PROCEEDINGS A

rspa.royalsocietypublishing.org

Research

Article submitted to journal

Subject Areas:

Wave motion, applied mathematics

Keywords:

Topological sensitivity, inverse scattering, diffraction catastrophe

Author for correspondence:

Bojan B. Guzina

e-mail: guzin001@umn.edu

Why the high-frequency inverse scattering by topological sensitivity may work

Bojan B. Guzina and Fatemeh Pourahmadian

Department of Civil, Environmental, and Geo-Engineering, University of Minnesota, Twin Cities, U.S.

This study deciphers the topological sensitivity as a tool for the reconstruction and characterization of impenetrable anomalies in the high-frequency regime. It is assumed that the anomaly is simply connected and convex, and that the measurements of the scattered field are of the far-field type. In this setting, the formula for topological sensitivity – which quantifies the perturbation of a cost functional due to a point-like impenetrable scatterer – is expressed as a pair of nested surface integrals: one taken over the boundary of a hidden obstacle, and the other over the measurement surface. Using multipole expansion, the latter integral is reduced to a set of antilinear forms featuring the Green's function and its gradient. The remaining expression is distilled by evaluating the scattered field on the surface of an obstacle via Kirchhoff approximation, and pursuing an asymptotic expansion of the resulting Fourier integral. In this way the topological sensitivity is found to survive upon three asymptotic lynchpins, namely i) the near-boundary approximation for sampling points close to the "exposed" surface of an obstacle; ii) uniform expansions synthesizing the diffraction catastrophes for sampling points near caustic surfaces, lines, and points; and iii) stationary phase approximation. Within the framework of catastrophe theory it is shown that, in the case of the full source aperture, the topological sensitivity is asymptotically dominated by the (explicit) near-boundary term – which explains the previously reported reconstruction capabilities of this class of indicator functionals. The analysis further shows that, when the (Dirichlet or Neumann) character of an anomaly is unknown beforehand, the latter can be effectively exposed by assuming point-like Dirichlet perturbation and considering the sign of the leading term inside the reconstruction.

THE ROYAL SOCIETY
PUBLISHING

1. Introduction

Waveform tomography and in particular inverse obstacle scattering are essential to a broad spectrum of science and technology disciplines including geophysics, oceanography, optics, aeronautics, and non-destructive material testing. In general the relationship between the wavefield scattered by an obstacle and its geometry (or physical characteristics) is nonlinear, which invites two overt solution strategies: i) linearization via e.g. Born approximation and ray theory [13], or ii) pursuit of the nonlinear minimization approach [44]. Over the past two decades, however, a number of *sampling methods* have emerged that both consider the nonlinear nature of the inverse problem and dispense with iterations. Commonly, these techniques deploy an indicator functional that varies with spatial coordinates of the trial i.e. sampling point, and projects observations of the scattered field onto a functional space reflecting the "baseline" wave motion in a background medium. This indicator functional, designed to reach extreme values when the sampling point strikes the anomaly, accordingly provides a tomogram via its (thresholded) spatial distribution. Examples of such imaging paradigm include the linear sampling method [21] and the factorization technique [34] in the context of extended (i.e. finite-sized) scatterers, as well as the MUSIC algorithm [24] and the direct approach [8] as techniques catering primarily for point-like targets.

Another sampling take on inverse scattering, that motivates this study, is the method of topological sensitivity (TS) [29, 32]. Stemming from the framework of shape optimization [39], this technique has emerged as an effective tool for the waveform tomography of extended obstacles in acoustics [14, 18, 19, 29, 33], electromagnetism [35, 36], and elastodynamics [1, 9, 15, 20]. Formally, the TS quantifies the leading-order perturbation of a given misfit functional when an infinitesimal scatterer is introduced at a sampling point in the reference domain – being imaged for obstacles. From the application viewpoint, the appeal of TS resides in its forthright computability as a bilinear form in terms of two (free and adjoint) forward solutions for the reference domain. Following the heuristic argument, this quantity is then used as *obstacle indicator* by identifying the support of its pronounced negative values with an anomaly.

Despite the mounting numerical [9, 15, 20, 29, 36] and experimental [26, 43] evidence of the imaging capability of the method in a variety of sensing configurations, a theoretical justification of the TS as an obstacle indicator function is still lacking. So far, [27] established the analogy between the topological sensitivity and time reversal, while [10] elucidated the TS reconstruction of a) point-like anomalies, and b) extended weak anomalies in the sense of small material contrast (Born approximation) and/or low excitation frequency. Further, [5] explained how the TS discerns small acoustic obstacles, and [4] exposed the link between the TS and error backpropagation. To date, however, the reported ability of TS to reconstruct obstacles of arbitrary (finite) size and contrast has eluded both physical understanding and rigorous justification. The problem is highlighted by the repeated observations [19, 20, 29, 43] that at higher frequencies, the usual reconstruction heuristics does not apply for the negative TS values tend to localize in a narrow region "*about the boundary*" of an anomaly [19] – rather than canvassing its support.

To help bridge the gap, this study focuses on the imaging by topological sensitivity of impenetrable (Dirichlet or Neumann) obstacles in the short-wavelength regime. First, the expression for the germane indicator functional is reduced, via multipole expansion and Kirchhoff approximation, to a Fourier-type surface integral over the illuminated part of the anomaly's boundary. Making use of the high-wavenumber hypothesis, the latter is distilled to three distinct asymptotic representations, namely i) the near-boundary approximation for sampling points within few wavelengths from the "exposed" surface of an obstacle; ii) diffraction catastrophes (of codimension less then four) for sampling points near caustic surfaces, lines, and points; and iii) non-uniform i.e. stationary phase approximation. Under the premise of a single illuminating (plane) wave, it is found that the distribution of topological sensitivity, while carrying hints about the shape of an anomaly via the near-boundary contribution, is controlled by the caustics. By way of the catastrophe theory and diffraction scaling laws, on the other hand, it is shown that in the case of the *full aperture* of illuminating wavefields, the topological sensitivity is asymptotically dominated by the (explicit) near-boundary term – which explains the evidenced imaging capabilities of this class of indicator functionals. This result further unveils the new reconstruction logic at short wavelengths where the *boundary* of an anomaly is obtained as a *zero level set* of the TS field separating its extreme negative and extreme positive values. From the practical point of view, such paradigm allows for obstacle reconstruction without the use of an ad-hoc threshold parameter, where the sign of TS inside the reconstruction can be used to identify the anomaly type (if unknown) as either Neumann or Dirichlet. The analysis is accompanied by numerical results and an application toward obstacle reconstruction to a recent set of experimental data [43].

2. Preliminaries

Consider the inverse scattering of time-harmonic scalar waves by a simply connected, convex, and impenetrable obstacle $D\subset\mathscr{B}_1\subset\mathbb{R}^3$ (of either Dirichlet or Neumann type) with smooth boundary $S=\partial D$, where $\mathscr{B}_1$ is an open ball of radius R_1 centered at the origin. On denoting by $\tilde{u}$ the scattered field generated by the action of an incident field u^i on D, the total field

$$u(\boldsymbol{\xi}) \,=\, u^i(\boldsymbol{\xi}) \,+\, \tilde{u}(\boldsymbol{\xi}), \qquad \boldsymbol{\xi}\in\mathbb{R}^3\backslash\overline{D}$$

is monitored over a closed measurement surface $\Gamma^{\text{obs}}=\partial\mathscr{B}_2$, where $\mathscr{B}_2$ is an open ball of radius $R_2=\alpha^{-1}R_1$ $(\alpha<1)$ centered at the origin, see Fig. 1. The reference background medium is assumed to be homogeneous with wave speed c and mass density ρ.

Objective. The goal is to reconstruct D, and to identify is character (as either sound-soft or sound-hard) in situations when such prior information is unavailable.

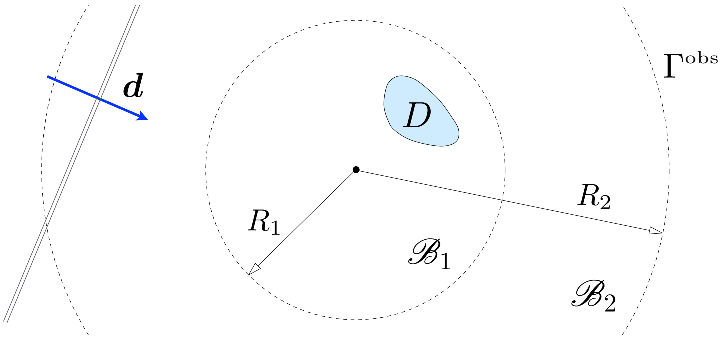

Figure 1. Impenetrable convex obstacle $D\in\mathbb{R}^3$ illuminated by plane waves.

Sensory data. Writing the implicit time dependence as $e^{\mathrm{i}\omega t}$, the incident field is assumed in the form of a *plane wave*, $u^i=e^{-\mathrm{i}k\boldsymbol{\xi}\cdot\boldsymbol{d}}$, endowed with wavenumber $k=\omega/c$ and direction $\boldsymbol{d}\in\Omega$ where Ω is a unit sphere. For each $\boldsymbol{d}$, values of the total field u are collected over Γ^{obs}.

Cost functional. To help solve the inverse problem, consider the misfit functional

$$J(\mathscr{D}) \;=\; \int_{\Gamma^{\text{obs}}} \varphi\left(v(\boldsymbol{\xi}),u(\boldsymbol{\xi}),\boldsymbol{\xi}\right)\,\mathrm{d}\Gamma_{\xi}, \tag{2.1}$$

computed for given $\boldsymbol{d}$, where $\mathscr{D}$ denotes the support of a *trial* (Dirichlet or Neumann) obstacle; v is the total field generated by the action of u^i on $\mathscr{D}$, and φ is a distance function that is differentiable with respect to the real and imaginary parts of its first argument. In what follows, φ is assumed to take the usual least-squares format

$$\varphi(v(\boldsymbol{\xi}),u(\boldsymbol{\xi}),\boldsymbol{\xi}) \;=\; \tfrac{1}{2}\,\overline{\left(v(\boldsymbol{\xi})-u(\boldsymbol{\xi})\right)}\,\left(v(\boldsymbol{\xi})-u(\boldsymbol{\xi})\right). \tag{2.2}$$

Green's function. For further reference, let

$$G(\boldsymbol{\xi},\boldsymbol{x}) \,=\, \frac{e^{-\mathrm{i}kr}}{4\pi r}, \qquad G_{,n}(\boldsymbol{\xi},\boldsymbol{x}) \,=\, \boldsymbol{n}\cdot\nabla G(\boldsymbol{\xi},\boldsymbol{x}) \,=\, -\,\frac{e^{-\mathrm{i}kr}}{4\pi r^2}(1+\mathrm{i}kr)\, r_{,n} \tag{2.3}$$

denote the fundamental solution for the free space $\mathbb{R}^3$ with wavenumber k, where $\boldsymbol{x}$ signifies the source location; $r=|\boldsymbol{\xi}-\boldsymbol{x}|$, and ∇G indicates differentiation with respect to *the first* argument.

Dimensional platform. In the sequel, all quantities are assumed to be dimensionless. This is accomplished by taking the radius of the inner sphere, the mass density of the background medium, and the sound speed in the background medium as the reference length, mass density, and velocity. In this setting, one in particular has $R_1=1$ and $R_2=\alpha^{-1}$.

(a) Topological Sensitivity

Let $\mathscr{D}\subset\mathbb{R}^3$ contain the origin, and consider the perturbation of $J(\emptyset)$ due to insertion of a vanishing impenetrable obstacle $\mathscr{D}_\epsilon=\boldsymbol{x}^\text{o}+\epsilon\mathscr{D}$ at a sampling point $\boldsymbol{x}^\text{o}\in\mathscr{B}_1$. In this case, it can be shown [7, 8] that

$$J(\mathscr{D}_\epsilon) \;=\; J(\emptyset) \;+\; T(\boldsymbol{x}^\text{o})\, f(\epsilon) \;+\; o(f(\epsilon)), \qquad \epsilon\to 0 \tag{2.4}$$

where $\lim_{\epsilon\to 0} f(\epsilon)=0$ and $T(\boldsymbol{x}^\text{o})$, the so-called topological sensitivity, is independent of ϵ. Taking $\mathscr{D}$ as the *unit ball*, analyses further show [7, 8, 33, 38] that

$$T(\boldsymbol{x}^\text{o}) \;=\; \text{Re}\Big[A\,\nabla u^i(\boldsymbol{x}^\text{o})\cdot\nabla u^a(\boldsymbol{x}^\text{o}) \;+\; B\,u^i(\boldsymbol{x}^\text{o})\,u^a(\boldsymbol{x}^\text{o})\Big] \tag{2.5}$$

where the coefficients A and B depend on the physical character of a vanishing perturbation, and u^a is the so-called adjoint field, generated in $\mathbb{R}^3$ by the single-layer potential $\partial\varphi(v,u,\boldsymbol{\xi})/\partial v|_{v=u^i}=\overline{(u^i-u)}(\boldsymbol{\xi})$ on Γ^obs. Note that the implicit assumption underpinning (2.5) is that the wavenumber k is fixed in the limiting process, whereby $k\epsilon\to 0$ in (2.4), see [2, 31]. As a prelude to the ensuing discussion, Table 1 specifies the coefficients A and B in situations when $\mathscr{D}_\epsilon$ is either sound-soft or sound-hard.

(b) Scaled TS indicator

As indicated earlier, the goal of this work is to provide an overarching high-frequency treatment of impenetrable (Dirichlet and Neumann) obstacles via the concept of topological sensitivity. Given the dependence of B on k in the Neumann case (see Table 1), however, one may conveniently introduce a *scaled counterpart* of (2.5), namely

$$\mathsf{T}(\boldsymbol{x}^\text{o}) \;:=\; k^\gamma\, T(\boldsymbol{x}^\text{o}) \;=\; \text{Re}\Big[\mathsf{A}\,\nabla\mathsf{u}^i(\boldsymbol{x}^\text{o})\cdot\nabla\mathsf{u}^a(\boldsymbol{x}^\text{o}) \;+\; \mathsf{k}^2\mathsf{B}\,\mathsf{u}^i(\boldsymbol{x}^\text{o})\,\mathsf{u}^a(\boldsymbol{x}^\text{o})\Big] \tag{2.6}$$

where the scaling parameter γ and normalized expansion coefficients A and B are given in Table 1. Relative to (2.5), the use of (2.6) is advantageous in that i) the new expansion coefficients are k-independent, and ii) the asymptotic order of T, in terms of powers of k, is invariant with respect to the (Dirichlet or Neumann) character of the vanishing perturbation. In the remainder of this work, (2.6) is *used as the basis* for the high-frequency reconstruction and identification of impenetrable obstacles. Note that the featured scaling of TS by k^γ (besides simplifying the analysis) does not affect the inverse solution, since the anomalies are usually identified from the relative variation of TS [e.g. 14, 18, 19, 29, 33].

Table 1. Expansion coefficients in the TS formula (2.5) assuming ball-shaped impenetrable perturbation [7, 8, 33, 38], and triplet of parameters (γ, A, B) featured by the scaled TS expression (2.6).

Vanishing obstacle	A	B	γ	A	B
Dirichlet (sound-soft)	0	1	2	0	1
Neumann (sound-hard)	3/2	$-k^2$	0	3/2	-1

To help expose the high-frequency behavior of T, one may expand the adjoint field in (2.6) as

$$\mathsf{T}(\boldsymbol{x}^{\rm o}) \;=\; \int_{\mathit{\Gamma}^{\rm obs}} \mathrm{Re}\left[\overline{(u^i - u)}(\boldsymbol{\xi}) \left\{\mathsf{A}\,\nabla \mathsf{u}^i(\boldsymbol{x}^{\rm o}) \cdot \nabla \mathsf{G}(\boldsymbol{x}^{\rm o},\boldsymbol{\xi}) \;+\; \mathsf{k}^2 \mathsf{B}\,\mathsf{u}^i(\boldsymbol{x}^{\rm o})\; \mathsf{G}(\boldsymbol{x}^{\rm o},\boldsymbol{\xi})\right\}\right] \mathrm{d}\mathit{\Gamma}_{\xi}, \qquad \boldsymbol{x}^{\rm o} \in \mathscr{B}_1, \tag{2.7}$$

and recall the integral representation of the scattered field

$$-\tilde{u}(\boldsymbol{\xi}) \;=\; (u^i - u)(\boldsymbol{\xi}) \;=\; \int_S \Big(u_{,n}(\boldsymbol{\zeta})\, G(\boldsymbol{\zeta},\boldsymbol{\xi}) \;-\; u(\boldsymbol{\zeta})\, \boldsymbol{n}(\boldsymbol{\zeta})\cdot\nabla G(\boldsymbol{\zeta},\boldsymbol{\xi})\Big)\mathrm{d}S_{\zeta}, \qquad \mathbb{R}^3\backslash\overline{D}$$

where $\boldsymbol{n}$ is the unit *outward* normal on S; $u_{,n} = \boldsymbol{n}\cdot\nabla u$, and $\mathscr{B}_1$ contains the region that is sampled for anomalies. Accordingly, (2.7) can be rewritten as

$$\begin{aligned}
\mathsf{T}(\boldsymbol{x}^{\rm o}) \;=\; -\mathrm{Re}\Bigg[\mathsf{A}\,\nabla\mathsf{u}^i(\boldsymbol{x}^{\rm o})\cdot\Bigg\{&\int_{\mathsf{S}} \overline{\mathsf{u}}_{,\mathsf{n}}(\boldsymbol{\zeta}) \int_{\mathit{\Gamma}^{\rm obs}} \overline{\mathsf{G}}(\boldsymbol{\xi},\boldsymbol{\zeta})\, \nabla\mathsf{G}(\boldsymbol{\xi},\boldsymbol{x}^{\rm o})\, \mathrm{d}\mathit{\Gamma}_{\xi}\, \mathrm{d}\mathsf{S}_{\zeta} \\
&+ \int_S \overline{u}(\boldsymbol{\zeta})\, \boldsymbol{n}(\boldsymbol{\zeta})\cdot \int_{\mathit{\Gamma}^{\rm obs}} \nabla\overline{G}(\boldsymbol{\xi},\boldsymbol{\zeta}) \otimes \nabla G(\boldsymbol{\xi},\boldsymbol{x}^{\rm o})\, \mathrm{d}\mathit{\Gamma}_{\xi}\, \mathrm{d}S_{\zeta}\Bigg\} \\
- k^2 \mathsf{B}\,\mathsf{u}^i(\boldsymbol{x}^{\rm o})\Bigg\{&\int_{\mathsf{S}} \overline{\mathsf{u}}_{,\mathsf{n}}(\boldsymbol{\zeta}) \int_{\mathit{\Gamma}^{\rm obs}} \overline{\mathsf{G}}(\boldsymbol{\xi},\boldsymbol{\zeta})\, \mathsf{G}(\boldsymbol{\xi},\boldsymbol{x}^{\rm o})\, \mathrm{d}\mathit{\Gamma}_{\xi}\, \mathrm{d}\mathsf{S}_{\zeta} \\
&+ \int_S \overline{u}(\boldsymbol{\zeta})\, \boldsymbol{n}(\boldsymbol{\zeta})\cdot \int_{\mathit{\Gamma}^{\rm obs}} \nabla\overline{G}(\boldsymbol{\xi},\boldsymbol{\zeta})\, G(\boldsymbol{\xi},\boldsymbol{x}^{\rm o})\, \mathrm{d}\mathit{\Gamma}_{\xi}\, \mathrm{d}S_{\zeta}\Bigg\}\Bigg],
\end{aligned} \tag{2.8}$$

due to the fact that $G(\boldsymbol{x},\boldsymbol{y}) = G(\boldsymbol{y},\boldsymbol{x})$ and $\nabla G(\boldsymbol{x},\boldsymbol{y}) = -\nabla G(\boldsymbol{y},\boldsymbol{x})$.

(c) Approximation of the component integrals over $\mathit{\Gamma}^{\rm obs}$

The purpose of this section is to reduce the TS formula (2.8) to a single, Fourier-type surface integral that is amenable to short-wavelength approximation. Note that analogous derivations can be found in [3, 5]. From (2.3), it follows that

$$\begin{aligned}
&\nabla^2 G(\boldsymbol{\xi},\boldsymbol{x}^{\rm o}) \;+\; k^2\, G(\boldsymbol{\xi},\boldsymbol{x}^{\rm o}) \;+\; \delta(\boldsymbol{\xi}-\boldsymbol{x}^{\rm o}) &&= 0, \\
&\nabla^2 G(\boldsymbol{\xi},\boldsymbol{\zeta}) \;+\; k^2\, G(\boldsymbol{\xi},\boldsymbol{\zeta}) \;+\; \delta(\boldsymbol{\xi}-\boldsymbol{\zeta}) &&= 0,
\end{aligned} \qquad \boldsymbol{\xi}\in\mathbb{R}^3. \tag{2.9}$$

On multiplying (2.9a) and (2.9b) respectively by $\overline{G}(\boldsymbol{\xi},\boldsymbol{\zeta})$ and $\overline{G}(\boldsymbol{\xi},\boldsymbol{x}^{\rm o})$ and integrating by parts over $\mathscr{B}_2$, one finds by way of the divergence theorem that

$$\begin{aligned}
&\int_{\mathit{\Gamma}^{\rm obs}} G_{,n}(\boldsymbol{\xi},\boldsymbol{a})\, \overline{G}(\boldsymbol{\xi},\boldsymbol{b})\, \mathrm{d}\mathit{\Gamma}_{\xi} \;-\; \int_{\mathscr{B}_2} \nabla G(\boldsymbol{\xi},\boldsymbol{a})\cdot\nabla\overline{G}(\boldsymbol{\xi},\boldsymbol{b})\, \mathrm{d}\mathscr{B}_{\xi} \\
&\qquad + \; k^2 \int_{\mathscr{B}_2} G(\boldsymbol{\xi},\boldsymbol{a})\, \overline{G}(\boldsymbol{\xi},\boldsymbol{b})\, \mathrm{d}\mathscr{B}_{\xi} \;=\; -\overline{G}(\boldsymbol{a},\boldsymbol{b}), \qquad (\boldsymbol{a},\boldsymbol{b}) \in \big\{(\boldsymbol{x}^{\rm o},\boldsymbol{\zeta}), (\boldsymbol{\zeta},\boldsymbol{x}^{\rm o})\big\}
\end{aligned} \tag{2.10}$$

Thanks to (2.3), the subtraction of the complex conjugate of (2.10) with $(\boldsymbol{a},\boldsymbol{b}) = (\boldsymbol{\zeta},\boldsymbol{x}^{\rm o})$ from its companion yields

$$\int_{\mathit{\Gamma}^{\rm obs}} \overline{G}(\boldsymbol{\xi},\boldsymbol{\zeta})\, G(\boldsymbol{\xi},\boldsymbol{x}^{\rm o})\, \big[1 + E(\boldsymbol{\xi},\boldsymbol{x}^{\rm o},\boldsymbol{\zeta})\big]\, \mathrm{d}\mathit{\Gamma}_{\xi} \;=\; -\frac{1}{k}\,\mathrm{Im}\big(G(\boldsymbol{x}^{\rm o},\boldsymbol{\zeta})\big), \quad \boldsymbol{x}^{\rm o},\boldsymbol{\zeta}\in\mathscr{B}_1, \tag{2.11}$$

where

$$E(\boldsymbol{\xi},\boldsymbol{x}^{\rm o},\boldsymbol{\zeta}) \;=\; \left[\frac{1}{2\mathrm{i}k}\Big(\bar{\widehat{(\boldsymbol{\xi}-\boldsymbol{x}^{\rm o})}} - \bar{\widehat{(\boldsymbol{\xi}-\boldsymbol{\zeta})}}\Big) + \frac{1}{2}\Big(\widehat{(\boldsymbol{\xi}-\boldsymbol{x}^{\rm o})} + \widehat{(\boldsymbol{\xi}-\boldsymbol{\zeta})}\Big)\right]\cdot\boldsymbol{n}(\boldsymbol{\xi}) - 1,$$

noting that $\widehat{\boldsymbol{x}} = \boldsymbol{x}/|\boldsymbol{x}|$ and $\bar{\widehat{\boldsymbol{x}}} = \boldsymbol{x}/|\boldsymbol{x}|^2$. On recalling that $R_1 = 1$ and $R_2 = \alpha^{-1} > 1$, it can be shown via triangle inequality that $|E| < \alpha^2/(k(1-\alpha^2)) + \alpha^2/2 + O(\alpha^4)$. When $k \geqslant O(1)$, (2.11) accordingly yields the Helmholtz-Kirchhoff identity

$$\int_{\mathit{\Gamma}^{\rm obs}} \overline{G}(\boldsymbol{\xi},\boldsymbol{\zeta})\, G(\boldsymbol{\xi},\boldsymbol{x}^{\rm o})\, \mathrm{d}\mathit{\Gamma}_{\xi} \;\overset{\alpha^2}{=}\; -\frac{1}{k}\,\mathrm{Im}\big(G(\boldsymbol{x}^{\rm o},\boldsymbol{\zeta})\big), \qquad \boldsymbol{x}^{\rm o},\boldsymbol{\zeta}\in\mathscr{B}_1, \tag{2.12}$$

where “$\overset{\alpha^n}{=}$” signifies approximation with an $O(\alpha^n)$ residual.

On differentiating (2.11) with respect to $\boldsymbol{x}^\text{o}$ and $\boldsymbol{\zeta}$, it can be similarly shown that

$$\begin{aligned}\int_{\mathit{\Gamma}^\text{obs}} \overline{G}(\boldsymbol{\xi},\boldsymbol{\zeta})\,\nabla G(\boldsymbol{\xi},\boldsymbol{x}^\text{o})\,\text{d}\mathit{\Gamma}_{\xi} &\overset{\alpha^2}{=} -\Big[\text{Re}\big(G(\boldsymbol{x}^\text{o},\boldsymbol{\zeta})\big)+\frac{1}{kr}\,\text{Im}\big(G(\boldsymbol{x}^\text{o},\boldsymbol{\zeta})\big)\Big]\,(\widehat{\boldsymbol{x}^\text{o}-\boldsymbol{\zeta}}) \\ \int_{\mathit{\Gamma}^\text{obs}} \nabla\overline{G}(\boldsymbol{\xi},\boldsymbol{\zeta})\,G(\boldsymbol{\xi},\boldsymbol{x}^\text{o})\,\text{d}\mathit{\Gamma}_{\xi} &\overset{\alpha^2}{=} \Big[\text{Re}\big(G(\boldsymbol{x}^\text{o},\boldsymbol{\zeta})\big)+\frac{1}{kr}\,\text{Im}\big(G(\boldsymbol{x}^\text{o},\boldsymbol{\zeta})\big)\Big]\,(\widehat{\boldsymbol{x}^\text{o}-\boldsymbol{\zeta}}), \qquad \boldsymbol{x}^\text{o},\boldsymbol{\zeta}\in\mathscr{B}_1\end{aligned} \tag{2.13}$$

and

$$\begin{aligned}\int_{\mathit{\Gamma}^\text{obs}} \nabla\overline{G}(\boldsymbol{\xi},\boldsymbol{\zeta})\otimes\nabla G(\boldsymbol{\xi},\boldsymbol{x}^\text{o})\,\text{d}\mathit{\Gamma}_{\xi} &\overset{\alpha^2}{=} -\frac{1}{r}\Big[\text{Re}\big(G(\boldsymbol{x}^\text{o},\boldsymbol{\zeta})\big)+\frac{1}{kr}\text{Im}\big(G(\boldsymbol{x}^\text{o},\boldsymbol{\zeta})\big)\Big]\,\boldsymbol{I} \\ &\quad+\frac{1}{r}\Big[3\,\text{Re}\big(G(\boldsymbol{x}^\text{o},\boldsymbol{\zeta})\big)+\Big(\frac{3}{kr}-kr\Big)\text{Im}\big(G(\boldsymbol{x}^\text{o},\boldsymbol{\zeta})\big)\Big](\widehat{\boldsymbol{x}^\text{o}-\boldsymbol{\zeta}})\otimes(\widehat{\boldsymbol{x}^\text{o}-\boldsymbol{\zeta}}), \qquad \boldsymbol{x}^\text{o},\boldsymbol{\zeta}\in\mathscr{B}_1,\end{aligned} \tag{2.14}$$

where ∇G indicates differentiation with respect to the first argument, $r{=}|\boldsymbol{x}^\text{o}-\boldsymbol{\zeta}|$ and $\boldsymbol{I}$ is the second-order identity tensor.

Remark 1. *Hereon, it is assumed that the sensory data in Fig. 1 are of the far-field type ($R_2\to\infty$), which amounts to setting $\alpha=0$ in (2.12)–(2.14).*

3. High-frequency behavior of topological sensitivity

As examined earlier, the objective of this work is to understand the previously reported high-frequency patterns of the TS indicator functional [e.g. 19, 29], obtained when (2.7) is applied to the scattered field data at wavelengths ($2\pi/k$) that are smaller than the characteristic size of an obstacle, L_o. In this vein, the ensuing analysis assumes a *separation of scales* in that $\epsilon\ll 2\pi/k\ll L_\text{o}$, where $\epsilon\to 0$ is the size of a vanishing perturbation in (2.4) while $2\pi/k$, however small, is *fixed* in the limiting process. With such premise, consider the scattering of a plane wave, $u^i=e^{-\text{i}k\boldsymbol{x}\cdot\boldsymbol{d}}$, by convex impenetrable obstacle D as in Section 2. Next, let $\boldsymbol{n}$ signify the outward normal on $S{=}\partial D$; let $S^\text{f}(\boldsymbol{d})=\{\boldsymbol{x}{\in}S:\boldsymbol{n}(\boldsymbol{x})\cdot\boldsymbol{d}<0\}$ be the "front" (i.e. illuminated) part of S, and denote by $S^\text{b}(\boldsymbol{d})=\{\boldsymbol{x}{\in}S:\boldsymbol{n}(\boldsymbol{x})\cdot\boldsymbol{d}\geqslant 0\}$ its "back" side.

Here it is noted that the high-frequency analysis of integrals similar to those featured in Section 2(a) has been recently proposed in [6] toward developing an iterative scheme for the multistatic imaging of extended penetrable targets. There, it is shown that the high-frequency data can be used to construct a good initial guess for the illuminated part of the inclusion.

Dirichlet obstacle as a testbed. To provide specificity for the analysis, it is hereon assumed that the hidden i.e. extended obstacle D is *sound-soft*. The case of a Neumann (sound-hard) obstacle is addressed separately in Section 4(d) and Appendix E (supplementary material). As it turns out, however, the latter developments draw heavily from the Dirichlet analysis – and in fact require only a minimal amount of additional deliberation.

Remark 2. *When D is of Dirichlet type, it is natural to let the trial vanishing obstacle $\mathscr{D}_\epsilon$ (underpinning the definition of TS) be sound-soft, i.e. to set $(\mathsf{A},\mathsf{B})=(0,1)$ in (2.6) and (2.8) according to Table 1. In general, however, the character of D (as an impenetrable anomaly) constitutes prior information that may not be available. As a result, it is of interest to proceed with the inverse scattering of sound-soft D while allowing (A,B) to assume either pair of values given in Table 1. As will be shown in Section 4(e), such paradigm paves the way toward a simultaneous reconstruction and characterization of extended impenetrable obstacles in situations when their character is unknown beforehand.*

(a) Kirchhoff approximation

When the extended obstacle is sound-soft and $kL_{\rm o} \gg 1$, the physical optics (Kirchhoff) approximation [12] states that

$$u = 0 \quad \text{on} \quad S = \partial D, \qquad\qquad u_{,n} = \begin{cases} 2\, u^i_{,n} & \text{on} \quad S^{\rm f} \\ 0 & \text{on} \quad S^{\rm b} \end{cases}. \tag{3.1}$$

By virtue of (3.1), (2.8) reduces to

$$\begin{aligned} \mathsf{T}(\boldsymbol{x}^{\rm o}) \;=\; & -2\,{\rm Re}\Big[\mathsf{A}\,\nabla \mathsf{u}^i(\boldsymbol{x}^{\rm o}) \cdot \int_{\mathsf{S}^{\rm f}} \overline{\mathsf{u}^i}_{,\mathsf{n}}(\boldsymbol{\zeta}) \int_{\Gamma^{\rm obs}} \overline{\mathsf{G}}(\boldsymbol{\xi},\boldsymbol{\zeta})\,\nabla \mathsf{G}(\boldsymbol{\xi},\boldsymbol{x}^{\rm o})\,{\rm d}\Gamma_\xi\,{\rm d}\mathsf{S}_\zeta \\ & \qquad - k^2 \mathsf{B}\,\mathsf{u}^i(\boldsymbol{x}^{\rm o}) \int_{\mathsf{S}^{\rm f}} \overline{\mathsf{u}^i}_{,\mathsf{n}}(\boldsymbol{\zeta}) \int_{\Gamma^{\rm obs}} \overline{\mathsf{G}}(\boldsymbol{\xi},\boldsymbol{\zeta})\,\mathsf{G}(\boldsymbol{\xi},\boldsymbol{x}^{\rm o})\,{\rm d}\Gamma_\xi\,{\rm d}\mathsf{S}_\zeta\Big]. \end{aligned} \tag{3.2}$$

On recalling that $u^i = e^{-{\rm i}k\boldsymbol{x}\cdot\boldsymbol{d}}$ and substituting (2.12) and (2.13) into (3.2), one finds that

$$\mathsf{T}(\boldsymbol{x}^{\rm o}) \;=\; 2k^2\,{\rm Im}\Big[\mathsf{A}\,({\rm i\,e}^{-{\rm i}k\boldsymbol{x}^{\rm o}\cdot\boldsymbol{d}})\,\mathsf{J}_1 \;+\; \mathsf{B}\,({\rm e}^{-{\rm i}k\boldsymbol{x}^{\rm o}\cdot\boldsymbol{d}})\,\mathsf{J}_2\Big], \tag{3.3}$$

where

$$\begin{aligned} J_1 \;&=\; \int_{S^{\rm f}} e^{{\rm i}k\boldsymbol{\zeta}\cdot\boldsymbol{d}} \Big[{\rm Re}\big(G(\boldsymbol{x}^{\rm o},\boldsymbol{\zeta})\big) + \frac{1}{kr}\,{\rm Im}\big(G(\boldsymbol{x}^{\rm o},\boldsymbol{\zeta})\big)\Big]\; \boldsymbol{d}\cdot\boldsymbol{n}(\boldsymbol{\zeta})\;\boldsymbol{d}\cdot\widehat{(\boldsymbol{x}^{\rm o}-\boldsymbol{\zeta})}\,{\rm d}S_\zeta, \\ J_2 \;&=\; \int_{S^{\rm f}} e^{{\rm i}k\boldsymbol{\zeta}\cdot\boldsymbol{d}}\,{\rm Im}\big(G(\boldsymbol{x}^{\rm o},\boldsymbol{\zeta})\big)\;\boldsymbol{d}\cdot\boldsymbol{n}(\boldsymbol{\zeta})\,{\rm d}S_\zeta, \end{aligned} \tag{3.4}$$

and the $O(\alpha^2)$ approximation error stemming from (2.12) and (2.13) is tacit.

In what follows, the high-frequency behavior of (3.3) is characterized explicitly, assuming both i) illumination by a single incident wave and ii) full source aperture when $\boldsymbol{d} \in \Omega$. Specifically, the analysis shows that in the latter case, the TS distribution is approximated by a *closed-form expression* (the main contribution of this work) whose extreme values are localized in a neighborhood of ∂D, as suggested by numerical investigations [19, 29]. This result is stated in Theorem 4.6 for sound-soft obstacles, and in Theorem 4.7 for sound-hard obstacles. For completeness, Appendix E (supplementary material) examines the ramifications of assuming Kirchhoff approximation (3.1) on the claim of Theorem 4.6.

(b) Contribution of non-degenerate stationary points

Consider first the high-frequency behavior of (3.3) when the sampling point $\boldsymbol{x}^{\rm o}$ straddles the region of interest $\mathscr{B}_1$ *excluding* a "thin-shell" neighborhood of $S^{\rm f}$, namely $\boldsymbol{x}^{\rm o} \in \mathscr{B}_1 \backslash \mathscr{N}_\epsilon$, where

$$\mathscr{N}_\epsilon(\boldsymbol{d}) \;=\; \{\boldsymbol{x}\colon\, \boldsymbol{x} = \boldsymbol{\zeta} + \ell\,\boldsymbol{n}(\boldsymbol{\zeta}), \quad \boldsymbol{\zeta} \in S^{\rm f}(\boldsymbol{d}), \quad -\epsilon < \ell < \epsilon\}, \tag{3.5}$$

and $\epsilon = O(k^{-1})$ is a length scale to be specified later. In this setting, the analysis can be facilitated by recalling (2.3) and rewriting (3.3) as

$$\begin{aligned} J_1 &= \int_{S^{\rm f}} \frac{\boldsymbol{d}\cdot\boldsymbol{n}(\boldsymbol{\zeta})}{8\pi r}\Big(1+\frac{\rm i}{kr}\Big)\,\boldsymbol{d}\cdot\widehat{(\boldsymbol{x}^{\rm o}-\boldsymbol{\zeta})}\,e^{{\rm i}k(\boldsymbol{\zeta}\cdot\boldsymbol{d}+r)}\,{\rm d}S_\zeta + \int_{S^{\rm f}} \frac{\boldsymbol{d}\cdot\boldsymbol{n}(\boldsymbol{\zeta})}{8\pi r}\Big(1-\frac{\rm i}{kr}\Big)\,\boldsymbol{d}\cdot\widehat{(\boldsymbol{x}^{\rm o}-\boldsymbol{\zeta})}\,e^{{\rm i}k(\boldsymbol{\zeta}\cdot\boldsymbol{d}-r)}\,{\rm d}S_\zeta, \\ J_2 &= {\rm i}\int_{S^{\rm f}} \frac{\boldsymbol{d}\cdot\boldsymbol{n}(\boldsymbol{\zeta})}{8\pi r}\,e^{{\rm i}k(\boldsymbol{\zeta}\cdot\boldsymbol{d}+r)}\,{\rm d}S_\zeta - {\rm i}\int_{S^{\rm f}} \frac{\boldsymbol{d}\cdot\boldsymbol{n}(\boldsymbol{\zeta})}{8\pi r}\,e^{{\rm i}k(\boldsymbol{\zeta}\cdot\boldsymbol{d}-r)}\,{\rm d}S_\zeta, \qquad r = |\boldsymbol{x}^{\rm o}-\boldsymbol{\zeta}|. \end{aligned} \tag{3.6}$$

To evaluate (3.6), one may invoke the parametrization of $S^{\rm f}$ in terms of curvilinear surface coordinates (η^1,η^2) as

$$\boldsymbol{\zeta} = \boldsymbol{\zeta}(\eta^1,\eta^2) \in S^{\rm f}, \qquad {\rm d}S_\zeta = \sqrt{\det g_{pq}}\,{\rm d}S_\eta, \qquad {\rm d}S_\eta = {\rm d}\eta^1{\rm d}\eta^2, \qquad g_{pq} = \frac{\partial\boldsymbol{\zeta}}{\partial\eta^p}\cdot\frac{\partial\boldsymbol{\zeta}}{\partial\eta^q}, \qquad p,q = 1,2$$

where g_{pq} are the covariant components of the metric tensor.

As examined in [12], the leading-order asymptotic behavior of (3.6) for large k is governed by the nature of the integrand in the neighborhood of three types of *critical points*, namely: i) the stationary points on S^{f} where $\nabla_\eta(\boldsymbol{\zeta}\cdot\boldsymbol{d} \pm r)$ vanishes; ii) the points on S^{f} where the integrand fails to be differentiable, and iii) all points on the closed curve ∂S^{f} – the boundary of S^{f}. By way of (3.5), $r \geqslant \epsilon > 0$ whereby the integrands in (3.6) are differentiable everywhere. One may also note that the latter *vanish* on ∂S^{f} due to multiplier $\boldsymbol{d}\cdot\boldsymbol{n}$. Following the analysis in [12], the leading contribution of ∂S^{f} to J_1 and J_2 can accordingly be shown to behave as $O(k^{-2})$ when k is large. In contrast, the contribution of a non-degenerate stationary point $\boldsymbol{\zeta}^* \in S^{\mathrm{f}}$ to a two-dimensional Fourier integral

$$I \;=\; \int_{S^{\mathrm{f}}} f(\boldsymbol{\zeta})\, e^{\mathrm{i}k(\boldsymbol{\zeta}\cdot\boldsymbol{d}\pm r)}\, \mathrm{d}S_\eta, \qquad \boldsymbol{\zeta} = \boldsymbol{\zeta}(\eta^1,\eta^2), \qquad r = |\boldsymbol{\zeta} - \boldsymbol{x}^{\mathrm{o}}| \tag{3.7}$$

can be computed via *non-uniform* asymptotic approximation [e.g. 40] as $O\big(k^{-1}\big)$, namely

$$I^{\boldsymbol{\zeta}^*} \;\overset{k^{-2}}{=\!=}\; \frac{2\pi}{k}\,\frac{f(\boldsymbol{\zeta}^*)}{\sqrt{|\det A_{pq}|}}\, e^{\mathrm{i}k(\boldsymbol{\zeta}^*\cdot\boldsymbol{d}\pm r^*) + \mathrm{i}(\operatorname{sgn} A_{pq})\pi/4}, \qquad r^* = |\boldsymbol{\zeta}^* - \boldsymbol{x}^{\mathrm{o}}|, \tag{3.8}$$

where

$$A_{pq} \;=\; \frac{\partial^2(\boldsymbol{\zeta}\cdot\boldsymbol{d} \pm r)}{\partial\eta^p\partial\eta^q}\bigg|_{\boldsymbol{\zeta}=\boldsymbol{\zeta}^*}, \qquad p,q = 1,2 \tag{3.9}$$

are the components of the Hessian matrix; $\det A_{pq} \neq 0$ by definition for simple stationary points, and $\operatorname{sgn} A_{pq} \in \{-2,0,2\}$ is the difference between the numbers of positive and negative eigenvalues of A_{pq}. Accordingly the portion of (3.6) due to non-degenerate stationary points can be computed, to the leading order, by summing the contributions of type (3.8).

(i) Stationary points

To evaluate (3.6) via the method of stationary phase [12], it is noted that

$$\nabla_\eta(\boldsymbol{\zeta}\cdot\boldsymbol{d} \pm r) = \boldsymbol{0} \quad\Longrightarrow\quad \big[\boldsymbol{d} \pm (\widehat{\boldsymbol{\zeta} - \boldsymbol{x}^{\mathrm{o}}})\big]\cdot\frac{\partial\boldsymbol{\zeta}}{\partial\eta^p} \;=\; 0, \qquad \boldsymbol{\zeta}\in S^{\mathrm{f}}, \quad p = 1,2. \tag{3.10}$$

On denoting by $\boldsymbol{\zeta}^{\pm} \in S^{\mathrm{f}}$ the stationary point of $e^{\mathrm{i}k(\boldsymbol{\zeta}\cdot\boldsymbol{d}\pm r)}$, this implies that $\boldsymbol{d} \pm (\widehat{\boldsymbol{\zeta}^{\pm} - \boldsymbol{x}^{\mathrm{o}}})$ must either vanish or be perpendicular to S^{f}. Making use of the inequality $\boldsymbol{d}\cdot\boldsymbol{n} < 0$, one finds from (3.10) that J_1 and J_2 feature two types of stationary points, namely

$$\begin{aligned} \boldsymbol{\zeta}^{\pm}_{\mathrm{I}} \;&=\; \boldsymbol{x}^{\mathrm{o}} \mp r\,\boldsymbol{d} \\ \boldsymbol{\zeta}^{\pm}_{\mathrm{II}} \;&=\; \boldsymbol{x}^{\mathrm{o}} \mp r\,\big[\boldsymbol{d} + 2|\boldsymbol{d}\cdot\boldsymbol{n}|\,\boldsymbol{n}(\boldsymbol{\zeta}^{\pm}_{\mathrm{II}})\big] \end{aligned}, \qquad \boldsymbol{\zeta}^{\pm}_{\mathrm{I/II}} \in S^{\mathrm{f}}(\boldsymbol{d}), \qquad r > 0. \tag{3.11}$$

For a given sampling point, the stationary point of type I exists only if

$$\boldsymbol{x}^{\mathrm{o}} \in \mathscr{L}^{\pm}, \qquad \mathscr{L}^{\pm}(\boldsymbol{d}) \;=\; \{\boldsymbol{x}\colon\, \boldsymbol{x} = \boldsymbol{\zeta} \pm \tau\,\boldsymbol{d}, \quad \boldsymbol{\zeta}\in S^{\mathrm{f}}(\boldsymbol{d}), \quad \tau > 0\}, \tag{3.12}$$

and is *uniquely* determined by the projection of $\boldsymbol{x}^{\mathrm{o}}$ along $\boldsymbol{d}$ on S^{f}. In light of the implicit specification of $\boldsymbol{\zeta}^{\pm}_{\mathrm{II}}$, on the other hand, integrals J_1 and J_2 may have *multiple* stationary points of type II. To provide further insight into (3.11), let

$$\begin{aligned} \mathrm{I}^{\pm} \;&=\; \{\boldsymbol{x}^{\mathrm{o}}\colon\, \boldsymbol{x}^{\mathrm{o}} = \boldsymbol{\zeta}^{\pm}_{\mathrm{I}} \pm r\,\boldsymbol{d}, \quad r > 0\}, \\ \mathrm{II}^{\pm} \;&=\; \{\boldsymbol{x}^{\mathrm{o}}\colon\, \boldsymbol{x}^{\mathrm{o}} = \boldsymbol{\zeta}^{\pm}_{\mathrm{II}} \pm r\,\big[\boldsymbol{d} + 2|\boldsymbol{d}\cdot\boldsymbol{n}|\,\boldsymbol{n}(\boldsymbol{\zeta}^{\pm}_{\mathrm{II}})\big], \quad r > 0\}, \end{aligned} \tag{3.13}$$

denote the loci of the sampling points for which *given* boundary point $\boldsymbol{\zeta}\in S^{\mathrm{f}}$ is the stationary point of (3.6). This is illustrated in Fig. 2 which shows that the I^- and II^+ loci emanate from S^{f} toward the exterior of D, while their I^+ and II^- counterparts extend (initially) from S^{f} toward the interior of D. One also may note that at the "apex" of S^{f}, where $\boldsymbol{n} = -\boldsymbol{d}$, locus I^- (resp. I^+) coincides with locus II^+ (resp. II^-). Such coalescence, however, does not pose special problems since each of the component integrals in (3.6) will have a stationary point of *either* type I or type II that in this case coincides with the apex of S^{f}.

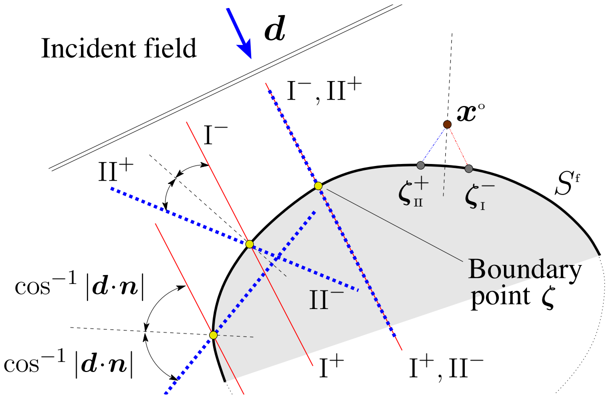

Figure 2. Loci of the sampling points, $\boldsymbol{x}^\circ$, for which given boundary point $\zeta \in S^{\rm f}$ is the *stationary point* of type I (solid lines) and type II (thick dashed lines). The normal on $S^{\rm f}$ is indicated by a thin dashed line. On the right side of the diagram, also depicted is the unique critical point of type I and the nearest critical point of type II for $\boldsymbol{x}^\circ$ close to $S^{\rm f}$.

Stationary point of type I. Recalling (3.12), the asymptotic behaviors of J_1 and J_2 entail the contribution of a unique stationary point $\zeta_{\rm I}^{\pm}$ when $\boldsymbol{x}^\circ \in \mathscr{L}^{\pm}$, and no entries of type $\mathrm{I}^{\pm}$ otherwise. The results in Appendix A(a) (supplementary material) show that in the former case

$$\det(A_{pq}) \,=\, \det g_{pq}\frac{(\boldsymbol{d}\cdot\boldsymbol{n})^2}{r^2} > 0, \qquad \operatorname{sgn}(A_{pq}) = \pm 2, \qquad \zeta = \zeta_{\rm I}^{\pm}, \quad \boldsymbol{x}^\circ \in \mathrm{I}^{\pm}. \tag{3.14}$$

Accordingly, the use of (3.3), (3.6) and (3.8) yields the contribution of $\zeta_{\rm I}^{\pm}$ to T as

$$\mathsf{T}^{\mathrm{I}^{\pm}}(\boldsymbol{x}^\circ) \overset{k^{-1}}{=\!=} \pm\frac{\mathsf{A}}{2r}, \qquad r = |\boldsymbol{x}^\circ - \zeta_{\rm I}^{\pm}|, \qquad \boldsymbol{x}^\circ \in \mathrm{I}^{\pm} \cap (\mathscr{B}_1 \backslash \mathscr{N}_\epsilon). \tag{3.15}$$

where r is separated from zero thanks to (3.5).

Stationary point of type II$^+$. From the analysis in Appendix A and Appendix C (supplementary material), one finds that J_1 and J_2 feature a *unique* stationary point $\zeta_{\rm II}^+$ when $\boldsymbol{x}^\circ \in \mathbb{R}^3 \backslash \bar{\mathscr{L}}^+$, and no contributions of type II^+ otherwise. In particular, it is shown that

$$\det(A_{pq}) \,=\, \det g_{pq}\frac{4(\boldsymbol{d}\cdot\boldsymbol{n})^2}{\rho_1\rho_2 r^2}\,(r+r_1)(r+r_2) > 0, \qquad \operatorname{sgn}(A_{pq}) = 2, \qquad \zeta = \zeta_{\rm II}^+, \quad \boldsymbol{x}^\circ \in \mathrm{II}^+, \tag{3.16}$$

where $\rho_{1/2}$ are the principal radii of curvature of $S^{\rm f}$ at $\zeta_{\rm II}^+$, while the roots $r_1 \geqslant r_2 > 0$ solve (A 5) (see Appendix A(a)). On the basis of (3.3), (3.6), (3.8) and (3.16), the contribution of $\zeta_{\rm II}^+$ to T reads

$$\mathsf{T}^{\mathrm{II}^+}(\boldsymbol{x}^\circ) \overset{1}{=} \frac{k\sqrt{\rho_1\rho_2}}{4\sqrt{(r+r_1)(r+r_2)}}\,\operatorname{Im}\Big[e^{2ik(\boldsymbol{d}\cdot\boldsymbol{n})^2 r}\Big]\Big\{\mathsf{A}\,(1-2(\boldsymbol{d}\cdot\boldsymbol{n})^2) + \mathsf{B}\Big\}, \\ r = |\boldsymbol{x}^\circ - \zeta_{\rm II}^+|, \quad \boldsymbol{x}^\circ \in \mathrm{II}^+ \cap (\mathscr{B}_1 \backslash \mathscr{N}_\epsilon), \tag{3.17}$$

where $\boldsymbol{n} = \boldsymbol{n}(\zeta_{\rm II}^+)$. A comparison between (3.15) and (3.17) immediately reveals that the stationary points of type $\mathrm{I}^{\pm}$ do not contribute to the leading asymptotic behavior of topological sensitivity; as a result, their $O(1)$ contribution is hereon ignored.

Stationary point of type II$^-$. With reference to Fig. 2 it is clear that, depending on $\boldsymbol{x}^\circ$, integrals J_1 and J_2 may feature *multiple* stationary points of type II^- according to the second of (3.11). For this class of critical points, it is shown in Appendix A(a) that

$$\det(A_{pq}) = \det g_{pq}\frac{4(\boldsymbol{d}\cdot\boldsymbol{n})^2}{\rho_1\rho_2 r^2}(r-r_1)(r-r_2), \quad \operatorname{sgn}(A_{pq}) = \sum_{j=1}^{2}\operatorname{sign}(r-r_j), \quad \zeta = \zeta_{\rm II}^-, \ \boldsymbol{x}^\circ \in \mathrm{II}^-, \tag{3.18}$$

where the nature of the roots $r_{1/2}$ and their bounds are detailed in Appendix A(b) (see for instance Fig. 15). From (3.18) it is seen that the non-uniform asymptotic expansion (3.8) breaks down as $r \to r_{1/2}$, which in physical terms corresponds to $\boldsymbol{x}^{\rm o}$ straddling a *caustic region* [40]. Appendix A(c) demonstrates that in this case the corank of A_{pq} approaches either 1 or 2, depending on $\boldsymbol{d}$ relative to the orthonormal basis $(\boldsymbol{a}_1, \boldsymbol{a}_2, \boldsymbol{n})$ – given by the principal directions and the outward normal to $S^{\rm f}$ at $\boldsymbol{\zeta}_{\rm II}^-$. On denoting by $\mathscr{C}_{\rm II} \subset {\rm II}^-$ the neighborhood of $r = r_{1/2}$ where (3.8) fails, the "minus" counterpart of (3.17) can be shown to read

$$\mathsf{T}^{{\rm II}^-}(\boldsymbol{x}^{\rm o}) \overset{1}{=} \frac{-k\sqrt{\rho_1\,\rho_2}}{4\sqrt{|(r-r_1)(r-r_2)|}}\, {\rm Im}\left[e^{-2{\rm i}k(\boldsymbol{d}\cdot\boldsymbol{n})^2 r + {\rm i}({\rm sgn}\, A_{pq}-2)\pi/4}\right]\Big\{\mathsf{A}\left(1-2(\boldsymbol{d}\cdot\boldsymbol{n})^2\right) + \mathsf{B}\Big\}, \tag{3.19}$$

$$r = |\boldsymbol{x}^{\rm o} - \boldsymbol{\zeta}_{\rm II}^-|, \qquad \boldsymbol{x}^{\rm o} \in ({\rm II}^- \backslash \mathscr{C}_{\rm II}) \cap (\mathscr{B}_1 \backslash \mathscr{N}_\epsilon),$$

where $\boldsymbol{n} = \boldsymbol{n}(\boldsymbol{\zeta}_{\rm II}^-)$. In principle when $\boldsymbol{x}^{\rm o} \in {\rm II}^- \backslash \mathscr{C}_{\rm II}$, the "mother" stationary point $\boldsymbol{\zeta}_{\rm II}^-$ does not interact with its neighbors in the sense that nominally $\det A_{pq}(\boldsymbol{\zeta}_{\rm II}^-) = O(1)$. In contrast when $\boldsymbol{x}^{\rm o} \in \mathscr{C}_{\rm II}$, $\det A_{pq}(\boldsymbol{p}) = O(k^{-\lambda})$ for some nominal $\lambda > 0$ – in which case the neighboring stationary points are sufficiently close to $\boldsymbol{\zeta}_{\rm II}^-$, and the germane interaction must be accounted for via uniform asymptotic expansion of (3.7) that is examined next.

(c) Uniform TS approximation in the caustic region

To frame the above discussion in a formal setting, recall that for a given i.e. fixed obstacle shape, the *bifurcation set* [41] of the phase function

$$\phi(\eta^1, \eta^2) = \boldsymbol{\zeta}\cdot\boldsymbol{d} - r, \qquad \boldsymbol{\zeta} = \boldsymbol{\zeta}(\eta^1, \eta^2), \qquad r = |\boldsymbol{\zeta} - \boldsymbol{x}^{\rm o}|, \tag{3.20}$$

is given by

$$B_\phi \;=\; \Big\{(\boldsymbol{d}, \boldsymbol{x}^{\rm o}) \in \Omega \times \mathbb{R}^3 :\; \nabla_\eta \phi = \boldsymbol{0}, \quad \det\left(\frac{\partial^2 \phi}{\partial \eta^p \partial \eta^q}\right) = 0, \quad \boldsymbol{\zeta} \in S^{\rm f}(\boldsymbol{d})\Big\}, \tag{3.21}$$

such that there exist at least two stationary points of ϕ whose distance vanishes as $(\boldsymbol{d}, \boldsymbol{x}^{\rm o}) \to B_\phi$.

Lemma 3.1. *For the problem under consideration,*

$$B_\phi \;=\; \Big\{(\boldsymbol{d}, \boldsymbol{x}^{\rm o}) \in \Omega \times \mathbb{R}^3 :\; \boldsymbol{x}^{\rm o} \in {\rm II}^-, \quad |\boldsymbol{x}^{\rm o} - \boldsymbol{\zeta}_{\rm II}^-| = r_{1/2}, \quad \boldsymbol{\zeta}_{\rm II}^- \in S^{\rm f}(\boldsymbol{d})\Big\}, \tag{3.22}$$

where the loci II^- *and affiliated caustic distances* $r_{1/2}$ *are specified respectively in (3.13) and Appendix A(a).*

Proof. The claim is a direct consequence of i) definition (3.21); ii) the completeness of the set of stationary points given by (3.11), and iii) the fact that the only loci in (3.13) which permit singular Hessian of the phase function are those of of type ${\rm II}^-$. ☐

Following [11], the interaction between stationary points should be considered as soon as their diminishing distance reaches $O(k^{-1/2})$ (a more precise condition will be established later). Hence when, given $\boldsymbol{d}$, the sampling point approaches the bifurcation set i.e. straddles the caustic region, the phase function is characterized by at least two *interacting* stationary points whose analysis warrants a uniform asymptotic treatment. In the context of (3.19) this neighborhood of interaction, as measured along ray ${\rm II}^-$, is denoted by $\mathscr{C}_{\rm II}$.

Elements of the catastrophe theory

The fundamental framework for the analysis of interacting (or coalescing) stationary points is provided by the catastrophe theory [42, 45], which is rooted in the notion of structurally-stable bifurcations [41]. To facilitate the discussion, assume without loss of generality that the phase function has a critical point at $\eta^1 = \eta^2 = 0$ so that $\nabla\phi|_{\boldsymbol{0}} = \boldsymbol{0}$. In this setting the theory originates from the Morse Lemma and Splitting Lemma [e.g. 37], which guarantee the existence of a local diffeomorphism $(\eta^1,\eta^2)\rightarrow(\vartheta^1,\vartheta^2)$ in a neighborhood of the critical point such that

$$\operatorname{corank}\Big(\frac{\partial^2\phi}{\partial\eta^p\partial\eta^q}\Big)\Big|_{\mathbf{0}} \;=\; \begin{cases} 0 & \Rightarrow \quad \phi \,=\, \pm(\vartheta^1)^2 \pm(\vartheta^2)^2 + \phi_\circ, \\ 1 & \Rightarrow \quad \phi \,=\, \pm(\vartheta^1)^2 + \psi(\vartheta^2) + \phi_\circ, \\ 2 & \Rightarrow \quad \phi \,=\, \psi(\vartheta^1,\vartheta^2) + \phi_\circ, \end{cases} \tag{3.23}$$

where $\phi_\circ$ is a constant, ψ is a smooth function whose value and derivatives up to order two all vanish at the origin. The basic question regarding (3.23), whose first phase representation signifies the non-degenerate case examined in Section 3(b), deals with the order of degeneracy carried by function ψ. This issue is resolved via the concept of *codimension*, $\mathrm{cod}(\phi)=\mathrm{cod}(\psi)$, of the phase function that can be introduced as follows. Consider first the so-called Jacobian ideal of ϕ, given by $\varDelta(\phi)=g_1\partial\phi/\partial\vartheta_1+g_2\partial\phi/\partial\vartheta_2$ for arbitrary smooth functions $g_{1/2}$, and its formal Taylor series, $\jmath\varDelta(\phi)$. With such definitions, the codimension of ϕ (assuming it is finite) can be written as

$$\mathrm{cod}(\phi)=\dim(H_2/\jmath\varDelta(\phi)), \tag{3.24}$$

where H_2 is the space of all power series $\mathbb{R}^2\rightarrow\mathbb{R}$ with zero constant term. In situations when $\jmath\varDelta(\phi)$ is expressible in terms of monomials, $\mathrm{cod}(\phi)$ is simply the number of missing monomials relative to those in H_2. As examined in [41], the geometric implication of (3.24) is that a small perturbation of ϕ with codimension n can produce at most $n{+}1$ critical points in a neighborhood of $\eta^1=\eta^2=0$.

Perhaps the most powerful result of the catastrophe theory is that of *universal unfolding*, which encapsulates feasible perturbations of ϕ (assuming structural stability) and provides for a uniform asymptotic treatment of diffraction catastrophes in a neighborhood of the bifurcation set. For a phase function $\phi=\hat{\phi}(\vartheta^1,\vartheta^2)$ of finite codimension, a universal unfolding can be written as

$$\jmath\hat{\phi}(\vartheta^1,\vartheta^2)\big|_{(\boldsymbol{d},\boldsymbol{x}^{\rm o})\in B_\phi} \;+\; \sum_{m=1}^{M} c_m(\boldsymbol{d},\boldsymbol{x}^{\rm o})\,h_m(\vartheta^1,\vartheta^2), \qquad M=\mathrm{cod}(\phi) \tag{3.25}$$

where c_m are the control parameters that vanish on B_ϕ, and h_m form a basis for H_2 modulo $\jmath\varDelta(\hat{\phi})$. In the context of (3.23) it is noted that (3.24) and (3.25) apply equally to ψ, since ϕ and ψ by definition share the codimension and universal unfolding.

Diffraction scaling. On denoting by $\varPsi(c_1,\ldots,c_M)$ the canonic Fourier integral with $k=1$ and prototypical unfolding (3.25) of the phase function, the leading-order contribution of cognate critical point to (3.7) in the neighborhood of B_ϕ when $k\gg 1$ can be computed (up to an $O(1)$ multiplier) by way of *diffraction scaling* [11] as $k^\mu\,\varPsi(k^{\sigma_1}c_1,\ldots,k^{\sigma_M}c_M)$, where μ is the so-called singularity index signifying the intensity of a caustic, c_m are k-independent, and $\sigma_m>0$ are the measures of fringe spacings in the control directions c_m (see Appendix B – supplementary material – for details).

Asymptotic order of the uniform approximation

With reference to (3.23)–(3.25), Table 2 provides the complete list of elementary diffraction catastrophes with $\mathrm{cod}(\phi)<4$ according to Thom's classification theorem [11, 41], including the respective universal unfoldings (where $(\vartheta^1,\vartheta^2)$ are replaced by (s,t)) and diffraction scaling parameters. Note that the diffraction catastrophes with $\mathrm{cod}(\phi)>3$ have not been fully analyzed due to their complexity [11]. To aid the high-frequency evaluation of topological sensitivity, Appendix B (supplementary material) outlines the uniform asymptotic expansion of two-dimensional Fourier integral (3.7) for each featured type of diffraction catastrophe. The main result of this summary, listed in the last column of Table 2, is the (fractional) asymptotic order of the uniform expansion when applied to the TS formula (3.3). As a point of reference, one may recall that the non-uniform approximations of type II are $O(k)$, while those of type I are $O(1)$.

Table 2. Elementary diffraction catastrophes with codimension less than four and the asymptotic order of their contribution, T^c, to the topological sensitivity. Following Appendix B, the error of each approximation is at most $O(k^{1/2})$.

Catastrophe	corank	cod	universal unfolding	μ	$\sigma_m^{\min}$	$\mathsf{T}^c(\boldsymbol{x}^\circ,\cdot,\cdot)$
Fold	1	1	$\pm s^2+t^3/3+ct$	1/6	2/3	$O(k^{7/6})$
Cusp	1	2	$\pm s^2+t^4+c_2t^2+c_1t$	1/4	1/2	$O(k^{5/4})$
Swallowtail	1	3	$\pm s^2+t^5+c_3t^3+c_2t^2+c_1t$	3/10	2/5	$O(k^{13/10})$
Hyp. umbilic	2	3	$s^3+t^3+c_3st+c_2t+c_1s$	1/3	1/3	$O(k^{4/3})$
Ell. umbilic	2	3	$s^3-st^2+c_3(s^2+t^2)+c_2t+c_1s$	1/3	1/3	$O(k^{4/3})$

Global shape of a scatterer. Assuming structural stability, the type of catastrophe affiliated with given stationary point $\boldsymbol{\zeta}_{\mathrm{II}}^-\in S^{\mathrm{f}}$ as $|\boldsymbol{x}^\circ-\boldsymbol{\zeta}_{\mathrm{II}}^-|\to r_{1/2}$ i.e. $(\boldsymbol{d},\boldsymbol{x}^\circ)\to B_\phi$ depends on the local behavior of the phase function, and thus on the geometry of S^{f}, in a neighborhood of $\boldsymbol{\zeta}_{\mathrm{II}}^-$. In Appendix A and Appendix B, the degeneracy of the Hessian matrix is examined in terms of the *second-order* properties of S^{f} (synthesized via the second fundamental form) at $\boldsymbol{\zeta}=\boldsymbol{\zeta}_{\mathrm{II}}^-$. In general, this type of analysis can be enriched by considering the *third- and higher-order* surface properties of $S=\partial D$ [11]. The principal result of this paper in terms of Theorem 4.6 and Theorem 4.7, however, applies *regardless* of this caveat – as long as the diffraction catastrophes affiliated with S do not exceed three in terms of their codimension.

(d) TS approximation in the neighborhood of S^{f}

To complete the analysis, consider the case $\boldsymbol{x}^\circ\in\mathscr{N}_\epsilon$ where $\mathscr{N}_\epsilon$ is a thin-shell neighborhood of S^{f} given by (3.5). It is apparent from Fig. 2 that as $\boldsymbol{x}^\circ\to S^{\mathrm{f}}$ from the outside (resp. inside) there exist at least two stationary points, $\boldsymbol{\zeta}_{\mathrm{II}}^+$ and $\boldsymbol{\zeta}_{\mathrm{I}}^-$ (resp. $\boldsymbol{\zeta}_{\mathrm{II}}^-$ and $\boldsymbol{\zeta}_{\mathrm{I}}^+$), that merge at the normal projection of $\boldsymbol{x}^\circ$ onto S^{f}, denoted by $\boldsymbol{x}^\star$. Further when $\boldsymbol{x}^\circ\in S^{\mathrm{f}}$, the phase function in (3.6) assumes locally-conical shape and becomes non-differentiable at $r=0$ i.e. $\boldsymbol{\zeta}=\boldsymbol{x}^\circ=\boldsymbol{x}^\star$, which is also the point where the non-exponential factors of integrands in J_1 and J_2 become singular. Under such circumstances, the asymptotic approximations developed in Sections 3(b)–(c) break down i.e. cease to represent the contribution of stationary points located in the vicinity of $\boldsymbol{x}^\star$. The purpose of this section is accordingly two-fold, namely to i) identify the length scale ϵ in (3.5) which preserves the validity of previously developed approximations, and ii) expose the asymptotic contribution of $\boldsymbol{x}^\star\in S^{\mathrm{f}}$ to the topological sensitivity (3.3) when $\boldsymbol{x}^\circ\in\mathscr{N}_\epsilon$.

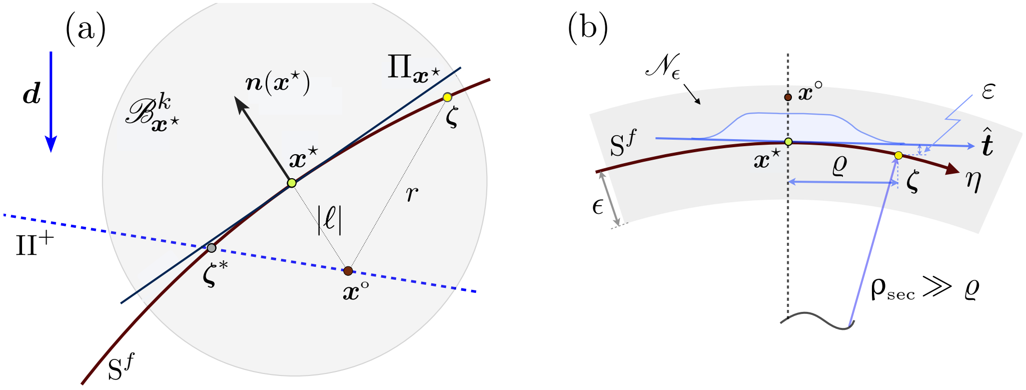

Figure 3. Sampling point $\boldsymbol{x}^\circ$ in a vicinity of the illuminated part, S^{f}, of the obstacle's boundary: (a) geometrical configuration, and (b) parameters in a generic normal section at $\boldsymbol{x}^\star$ used for computing the near-boundary approximation (ρ_{sec} is the sectional radius of curvature of S^{f}).

(i) Extent of $\mathscr{N}_\epsilon$

With reference to Fig. 3(a), consider without loss of generality the situation where

$$\boldsymbol{x}^{\mathrm{o}} \,=\, \boldsymbol{x}^\star - |\ell|\,\boldsymbol{n}(\boldsymbol{x}^\star), \qquad \ell \,=\, (\boldsymbol{x}^{\mathrm{o}} - \boldsymbol{x}^\star)\cdot\boldsymbol{n}(\boldsymbol{x}^\star),$$

for some $\boldsymbol{x}^\star\!\in S^{\mathrm{f}}$ and small $|\ell|$, and let $\boldsymbol{\zeta}^*\!=\!\boldsymbol{\zeta}_{\mathrm{II}}^{-}$ denote the germane stationary point of type II. Next, recall the two-term extension [40] of the non-uniform approximation (3.8) which reads

$$\frac{2\pi}{k}\,\frac{e^{\mathrm{i}(\operatorname{sgn} A_{pq})\pi/4}}{\sqrt{|\det A_{pq}|}}\,e^{\mathrm{i}k\varphi(\boldsymbol{\zeta}^*)}\big(\mathrm{f}_0 + k^{-1}\,\mathrm{f}_1\big), \tag{3.26}$$

in terms of generic phase function $\varphi(\boldsymbol{\zeta})$, where $A_{pq} = \partial^2\varphi/(\partial\eta^p\partial\eta^q)$;

$$\mathrm{f}_0 \,=\, f(\boldsymbol{\zeta}^*), \qquad \mathrm{f}_1 \,=\, 2\mathrm{i}\alpha^{-3}\big(2\mathrm{f}_0(\mathrm{p}_0 + \alpha\,\mathrm{p}_1) - 2\alpha\,\mathrm{p}_2 + \alpha^2\mathrm{p}_3\big), \qquad \alpha \,=\, \det A_{pq}, \tag{3.27}$$

and

$$\begin{aligned}
\mathrm{p}_0 \;&=\; 15\,(\varphi_{20}^3\,\varphi_{03}^2 \,+\, \varphi_{02}^3\,\varphi_{30}^2),\\
\mathrm{p}_1 \;&=\; \tfrac{3}{4}\varphi_{02}\,(2\varphi_{12}\,\varphi_{30} + \varphi_{21}^2) \,+\, \tfrac{3}{4}\,\varphi_{20}\,(2\varphi_{21}\,\varphi_{03} + \varphi_{12}^2) \,-\, 3(\varphi_{04}\,\varphi_{20}^2 + \varphi_{40}\,\varphi_{02}^2) \,-\, \varphi_{20}\,\varphi_{02}\,\varphi_{22},\\
\mathrm{p}_2 \;&=\; f_{10}\,(\varphi_{20}\,\varphi_{02}\,\varphi_{12} \,+\, 3\varphi_{30}\,\varphi_{02}^2) \,+\, f_{01}\,(\varphi_{02}\,\varphi_{20}\,\varphi_{21} \,+\, 3\varphi_{03}\,\varphi_{20}^2), \quad \mathrm{p}_3 \;=\; f_{02}\,\varphi_{20} \,+\, f_{20}\,\varphi_{02}.
\end{aligned}$$

Here $g_{ij} = (i!\,j!)^{-1}\partial^{i+j} g(\boldsymbol{\zeta})/(\partial x^i\partial y^j)|_{\boldsymbol{\zeta}=\boldsymbol{\zeta}^*}$ for $g = \varphi, f$, and (x,y) are obtained by a local diffeomorphism from (η^1,η^2) so that $\partial^2\varphi/\partial x\partial y = 0$ at $\boldsymbol{\zeta} = \boldsymbol{\zeta}^*$.

In the context of (3.26), the idea behind exposing the characteristic length ϵ in (3.5) is to find a threshold value of $|\ell|$ beyond which $|k^{-1}\mathrm{f}_1/\mathrm{f}_0| = o(1)$. For brevity of exposition, the attention is hereon focused on applying (3.26) to the component of J_1 in (3.6) with phase function $\boldsymbol{\zeta}\cdot\boldsymbol{d} - r$, noting that the analysis of the remaining integrals in (3.6) yields the same result when $\boldsymbol{x}^{\mathrm{o}} = \boldsymbol{x}^\star + \ell\,\boldsymbol{n}(\boldsymbol{x}^\star)$. To commence the analysis, let $|\ell| = |\boldsymbol{x}^{\mathrm{o}} - \boldsymbol{x}^\star| = O(k^{-1})$, and let $\boldsymbol{x}^\star$ be located away from ∂S^{f} so that $\boldsymbol{\zeta}^*$ in Fig. 3(a) is contained within a ball $\mathscr{B}^k_{\boldsymbol{x}^\star}$ of radius $O(k^{-1})$ centered at $\boldsymbol{x}^\star$. In the high-frequency regime, one has $\rho_1 \geqslant \rho_2 \gg k^{-1}$, where ρ_1 and ρ_2 are the principal radii of curvature of S^{f} at $\boldsymbol{x}^\star$. As a result, S^{f} can be locally approximated (within $\mathscr{B}^k_{\boldsymbol{x}^\star}$) by its tangent plane, $\mathit{\Pi}_{\boldsymbol{x}^\star}$, drawn at $\boldsymbol{x}^\star$. As shown in Section 3(d)ii, this treatment induces $O(k^{-2})$ error in the integration procedure.

To aid the application of (3.26), let the normal projection of $\boldsymbol{\zeta} \in S^{\mathrm{f}}$ on $\mathit{\Pi}_{\boldsymbol{x}^\star}$ be specified in terms of Cartesian coordinates (x,y) such that: i) $\boldsymbol{x}^\star$ is identified with the origin $(0,0)$, and ii) x is parallel to the tangential component of $\boldsymbol{d}$, namely $\boldsymbol{d}_t \,=\, \boldsymbol{d} \,+\, |\boldsymbol{d}\cdot\boldsymbol{n}|\,\boldsymbol{n}(\boldsymbol{x}^\star)$. In this setting, the phase function can be approximated locally as

$$\boldsymbol{\zeta}\cdot\boldsymbol{d} - r \,\simeq\, \varphi(\boldsymbol{\zeta}), \qquad \varphi \,=\, \boldsymbol{x}^\star\!\cdot\boldsymbol{d} \,+\, |\boldsymbol{d}_t|\,x \,-\, (\ell^2\!+\!x^2\!+\!y^2)^{1/2}, \qquad \boldsymbol{\zeta} \in S^{\mathrm{f}} \cap \mathscr{B}^k_{\boldsymbol{x}^\star} \tag{3.28}$$

for sufficiently large k. On computing the projection of the stationary point $\boldsymbol{\zeta}^*$ onto $\mathit{\Pi}_{\boldsymbol{x}^\star}$ as $(x^*,y^*) = (-\ell|\boldsymbol{d}_t|/d_n, 0)$ where $d_n = |\boldsymbol{d}\cdot\boldsymbol{n}(\boldsymbol{x}^\star)|$, the reduced phase function (3.28) can be expanded about (x^*,y^*) in Taylor series up to the fourth order to evaluate the necessary derivatives in (3.27). After treating in a similar way the multiplier of $\exp[\mathrm{i}k(\boldsymbol{\zeta}\cdot\boldsymbol{d} - r)]$ in the first of (3.6), one finds that

$$\frac{\mathrm{f}_1}{k\,\mathrm{f}_0} = \frac{1}{8}\left|\frac{d_n}{k\ell}\right|(|k\ell| - \mathrm{i}d_n)^{-1}\Big[d_n\,(15\,d_n^6 - 62\,d_n^4 + 87\,d_n^2 - 24) + \mathrm{i}\,|k\ell|\,(15\,d_n^6 - 46\,d_n^4 + 47\,d_n^2 - 8)\Big],$$

from which it follows that $|k^{-1}\mathrm{f}_1/\mathrm{f}_0| \lesssim (2\pi)^{-1}$ for $|\ell| > 2\pi/k$. As a result, the second-order term in (3.26) can be neglected, i.e. (3.8) holds, for normal distances to S^{f} of at least *one wavelength*. One should bear in mind that, as the shadow region is approached when $\boldsymbol{x}^\star\!\to \partial S^{\mathrm{f}}$ i.e. $d_n \to 0$, the foregoing analysis ceases to apply for the distance between $\boldsymbol{\zeta}^*$ and $\boldsymbol{x}^\star$ exceeds $O(k^{-1})$, see Fig. 3(a). In this case, however, the situation is mitigated by the fact that the kernels in (3.6) are all proportional to d_n, which makes precise knowledge of the portal distance in this border region less relevant. Accordingly, the above threshold on $|\ell|$ is applied uniformly $\forall \boldsymbol{x}^\star\!\in S^{\mathrm{f}}$ by stipulating $\epsilon = O(k^{-1}) \geqslant 2\pi/k$ in (3.5).

(ii) Asymptotic expansion for $\boldsymbol{x}^{\text{o}} \in \mathscr{N}_\epsilon$

In situations where the sampling point $\boldsymbol{x}^{\text{o}}$ straddles the "near-boundary" region (3.5) with $\epsilon = O(k^{-1}) \geqslant 2\pi/k$, the method of stationary phase ceases to apply for critical points close to the normal projection, $\boldsymbol{x}^\star$, of $\boldsymbol{x}^{\text{o}}$ on S^{f}. Further as $\boldsymbol{x}^{\text{o}} \to \boldsymbol{x}^\star$, the normal projection itself becomes a critical point owing to the loss of differentiability of the integrands in (3.6) there. This section is devoted to computing asymptotically the contribution of $\boldsymbol{x}^\star \in S^{\text{f}}$ (and its neighborhood) to $\mathsf{T}(\boldsymbol{x}^{\text{o}}, \cdot, \cdot)$ when $\boldsymbol{x}^{\text{o}} \in \mathscr{N}_\epsilon$.

It is well known that the topological sensitivity can be expressed as a bilinear form entailing two forward solutions for the reference domain, namely the incident field and the so-called adjoint field [e.g. 33]. In the context of Fig. 1, this guarantees that $\mathsf{T}(\boldsymbol{x}^{\text{o}}, \cdot, \cdot)$ is in fact analytic for $\boldsymbol{x}^{\text{o}} \in \mathscr{B}_1$. Indeed, the apparent singularities observed in (3.6) as $r \to 0$ (i.e. $\boldsymbol{x}^{\text{o}} \to S^{\text{f}}$) are the *artifact* of rearranging (3.4) to cater for the method of stationary phase, and can be dispensed with. Focusing on the component integral J_1 in (3.3), one finds from (2.3) and (3.4) that

$$J_1 \;=\; k\, e^{\mathrm{i}k\boldsymbol{x}^{\text{o}}\cdot\boldsymbol{d}} \int_{S^{\text{f}}} \frac{\boldsymbol{d}\cdot\boldsymbol{n}(\boldsymbol{\zeta})}{4\pi\, kr} \Big[\cos(kr) - \frac{\sin(kr)}{kr}\Big]\, \boldsymbol{d}\cdot\widehat{(\boldsymbol{x}^{\text{o}} - \boldsymbol{\zeta})}\, e^{-\mathrm{i}k\,(\boldsymbol{x}^{\text{o}}-\boldsymbol{\zeta})\cdot\boldsymbol{d}}\, \mathrm{d}S_{\boldsymbol{\zeta}}, \tag{3.29}$$

which is regular at $r{=}0$. To analyze (3.29) when $\boldsymbol{x}^{\text{o}} \in \mathscr{N}_\epsilon$, one may note that the local behavior of the integrand is dominated by the term $(kr)^{-1}[\cos(kr) - \sin(kr)/kr]$, that vanishes at $kr{=}0$ and reaches maximum (absolute) value at $kr \simeq 0.66$ i.e. $r = O(k^{-1})$. Thus, for sufficiently high k the contribution of $\boldsymbol{x}^\star$ to J_1 can be evaluated by approximating S^{f} via its tangent plane ($\mathit{\Pi}_{\boldsymbol{x}^\star}$) as shown in Fig. 3(a).

To expose the error in computing the contribution of $\boldsymbol{x}^\star$ to J_1 via tangent-plane approximation, consider a generic normal section of S^{f} at $\boldsymbol{x}^\star$, and let $\hat{\boldsymbol{t}}$ denote the germane tangent vector as in Fig. 3(b) so that

$$\begin{aligned} r \;&=\; \sqrt{(\ell+\varepsilon)^2 + \varrho^2}, \qquad \ell = O(k^{-1}), \qquad \varrho = (\boldsymbol{x}^{\text{o}} - \boldsymbol{\zeta})\cdot\hat{\boldsymbol{t}}, \\ \boldsymbol{x}^{\text{o}} - \boldsymbol{\zeta} \;&=\; (\ell+\varepsilon)\,\boldsymbol{n}(\boldsymbol{x}^\star) + \varrho\,\hat{\boldsymbol{t}}, \qquad \boldsymbol{n}(\boldsymbol{\zeta}) \;=\; \boldsymbol{n}(\boldsymbol{x}^\star) + \frac{2\varepsilon}{\varrho^2 + \varepsilon^2}\big(\varrho\hat{\boldsymbol{t}} - \varepsilon\boldsymbol{n}(\boldsymbol{x}^\star)\big). \end{aligned} \tag{3.30}$$

Note that for $r = O(k^{-1})$, one has $\varrho = O(k^{-1})$ and $\varepsilon = O(k^{-2})$ under the premise of locally-constant radius of curvature. Accordingly, it follows from (3.29) and (3.30) that

$$J_1 \;=\; J_1^\star \;+\; O(k^{-2}), \qquad J_1^\star \;=\; J_1|_{\varepsilon=0} \;=\; O(k^{-1}),$$

in terms of the asymptotic contribution of $\boldsymbol{x}^\star$ to J_1, where $J_1^\star$ denotes the tangent-plane approximation obtained by setting $\varepsilon{=}0$ in (3.30). On adopting the polar coordinate system (ϱ, θ) centered at $\boldsymbol{x}^\star$ so that direction $\boldsymbol{d}_t = \boldsymbol{d} - |\boldsymbol{d}\cdot\boldsymbol{n}|\boldsymbol{n}$ corresponds to $\theta = 0$, one finds that

$$J_1^\star = \frac{|\boldsymbol{d}\cdot\boldsymbol{n}|}{4\pi}\, e^{\mathrm{i}k\boldsymbol{x}^\star\cdot\boldsymbol{d}} \int_0^\infty \frac{k\varrho}{(kr_0)^2}\Big[\cos(kr_0) - \frac{\sin(kr_0)}{kr_0}\Big] \int_0^{2\pi} \Big(|\boldsymbol{d}\cdot\boldsymbol{n}|k\ell + d_t\cos(\theta)\,k\varrho\Big) e^{\mathrm{i}d_t k\varrho\cos(\theta)}\,\mathrm{d}\theta\,\mathrm{d}\varrho, \tag{3.31}$$

where $\boldsymbol{n} = \boldsymbol{n}(\boldsymbol{x}^\star)$, $r_0 {=} \sqrt{\ell^2 + \varrho^2}$, $d_t {=} \sqrt{1 - |\boldsymbol{d}\cdot\boldsymbol{n}|^2}$, and the outer integral is extended to infinity via an implicit neutralizer function [e.g. 40]. The inner integral over θ can be computed in terms of Bessel functions of the first kind, reducing the outer integral to a pair of Hankel transforms

$$J_1^\star \;=\; -\,\frac{|\boldsymbol{d}\cdot\boldsymbol{n}|}{2k}\, e^{\mathrm{i}k\boldsymbol{x}^\star\cdot\boldsymbol{d}} \Big\{|\boldsymbol{d}\cdot\boldsymbol{n}|\sin(k\ell) \;+\; d_t\Big[\mathrm{i}H_0(f_0; d_t) \;-\; |\boldsymbol{d}\cdot\boldsymbol{n}|\,k\ell\, H_1(f_1; d_t)\Big]\Big\}, \tag{3.32}$$

where

$$H_\nu(f(\varrho); \tau) = \int_0^\infty f(\varrho)\, J_\nu(\tau\varrho)\sqrt{\tau\varrho}\,\mathrm{d}\varrho, \qquad f_0 \;=\; \frac{\sin(kr_0)}{kr_0}\sqrt{k\,d_t\varrho}, \qquad f_1 \;=\; \frac{f_0}{k\,d_t\varrho}. \tag{3.33}$$

By way of the integral identities in [28], the leading-order contribution of $\boldsymbol{x}^\star$ to J_1 when $\boldsymbol{x}^{\text{o}} \in \mathscr{N}_\epsilon$ can accordingly be computed as

$$J_1^\star \;=\; -\,\frac{1}{2k}\, e^{\mathrm{i}k\boldsymbol{x}^\star\cdot\boldsymbol{d}} \Big\{\mathrm{i}d_t^2\cos(|\boldsymbol{d}\cdot\boldsymbol{n}|k\ell) \;+\; |\boldsymbol{d}\cdot\boldsymbol{n}|^2\sin(|\boldsymbol{d}\cdot\boldsymbol{n}|k\ell)\Big\}. \tag{3.34}$$

Recalling (3.4), the remaining integral in (3.3) can be evaluated in a similar fashion, yielding

$$J_2^\star \;=\; \frac{1}{2k}\, e^{\mathrm{i}k\boldsymbol{x}^\star\cdot\boldsymbol{d}} \cos(|\boldsymbol{d}\cdot\boldsymbol{n}|k\ell) \tag{3.35}$$

as the leading-order contribution of $\boldsymbol{x}^\star$ to J_2. On the basis of (3.3), (3.34) and (3.35), one finds

$$\mathsf{T}^\star(\boldsymbol{x}^\mathrm{o}) \;\overset{1}{=}\; \frac{k}{2}\sin(2k\ell|\boldsymbol{d}\cdot\boldsymbol{n}|)\,\Big\{\mathsf{A}\,(1-2|\boldsymbol{d}\cdot\boldsymbol{n}|^2)+\mathsf{B}\Big\}, \qquad \boldsymbol{x}^\mathrm{o}\!\in\!\mathscr{N}_\epsilon \tag{3.36}$$

to be the leading asymptotic contribution of $\boldsymbol{x}^\star$ to the topological sensitivity. It is perhaps not surprising that (3.36) shares the *common multiplier* with stationary phase approximations (3.17) and (3.19), dependent on $|\boldsymbol{d}\cdot\boldsymbol{n}|$ as well as the coefficients A and B – specified by the type of (impenetrable) vanishing perturbation according to Table 1.

4. Imaging ability of the TS indicator function

From (2.7), it is seen that for $\boldsymbol{x}^\mathrm{o}\!\in\mathscr{B}_1$ the topological sensitivity stems from a *bi-linear* form entailing two regular wave fields in the reference domain, namely the incident wave and the fundamental solution whose source is outside $\mathscr{B}_1$. As a result, the spatial distribution of TS is necessarily regular and generally characterized by wave-like fluctuations whose characteristic wavelength is π/k, i.e. half that of the illuminating wave. In this setting, the key question is that of the conditions under which the most pronounced negative values of TS are localized in a narrow region "about the boundary" [19] of an obstacle.

(a) Single plane-wave incidence

To provide an explicit platform for the analysis, the foregoing asymptotic developments (assuming the hidden anomaly to be of Dirichlet type) can be synthesized by writing

$$\begin{aligned}\mathsf{T}(\boldsymbol{x}^\mathrm{o}) \;&\overset{k^\nu}{=}\; 1_{\mathscr{N}_\epsilon(\boldsymbol{d})}(\boldsymbol{x}^\mathrm{o})\,\mathsf{T}^\star(\boldsymbol{x}^\mathrm{o}) \;+\; 1_{\tilde{B}_\phi}(\boldsymbol{d},\boldsymbol{x}^\mathrm{o})\,\mathsf{T}^c(\boldsymbol{x}^\mathrm{o}) \\ &+\; 1_{\mathscr{G}(\boldsymbol{d})}(\boldsymbol{x}^\mathrm{o})\,\mathsf{T}^{\mathrm{II}^+}(\boldsymbol{x}^\mathrm{o}) \;+\; \sum \mathsf{T}^{\mathrm{II}^-}(\boldsymbol{x}^\mathrm{o}), \qquad \boldsymbol{x}^\mathrm{o}\!\in\mathscr{B}_1, \quad \boldsymbol{d}\in\varOmega\end{aligned} \tag{4.1}$$

where $\nu\leqslant 1/2$; $1_M(m)$ is the characteristic function equalling 1 for $m\!\in\!M$ and 0 otherwise; recalling Fig. 4, $\mathscr{N}_\epsilon$ is a thin-shell neighborhood of S^f given by (3.5); $\tilde{B}_\phi\!\supset\! B_\phi$ is a neighborhood of the bifurcation set (3.21) where the non-uniform approximation fails; and, as shown in Appendix C (supplementary material), $\mathscr{G}(\boldsymbol{d})=\mathbb{R}^3\backslash\bar{\mathscr{L}}^+(\boldsymbol{d})$ where $\mathscr{L}^+$ is a semi-infinite cylindrical domain given by (3.12). From (3.17), (3.19), (3.36) and Table 2, one finds that

$$\mathsf{T}^\star = O(k), \qquad \mathsf{T}^c = O(k^\alpha), \quad \tfrac{7}{6}\leqslant\alpha\leqslant\tfrac{4}{3}, \qquad \mathsf{T}^{\mathrm{II}^\pm} = O(k). \tag{4.2}$$

Note that for given $\boldsymbol{d}$, the contributions of type $\mathsf{T}^\star$, T^c and $\mathsf{T}^{\mathrm{II}^+}$ are *unique* due respectively to: i) the uniqueness of the normal projection of $\boldsymbol{x}^\mathrm{o}\!\in\mathscr{N}_\epsilon$ on S^f, ii) premise that the hidden obstacle is convex with smooth boundary, and iii) geometrical grounds elaborated in Appendix C. In contrast $\mathsf{T}(\boldsymbol{x}^\mathrm{o})$ may include the contribution of *multiple* isolated stationary points of type II^-, as indicated by the summation symbol before $\mathsf{T}^{\mathrm{II}^-}$. In the context of (4.1) one should also mention that for $\boldsymbol{x}^\mathrm{o}\!\in\mathscr{N}_\epsilon$, the contribution of critical points within distance $O(k^{-1})$ from $\boldsymbol{x}^\star$ – accounted for via $\mathsf{T}^\star$ – is implicitly excluded when computing T^c and $\mathsf{T}^{\mathrm{II}^\pm}$.

From (4.2) it is readily seen that the near-boundary contribution is $O(k)$ i.e. commensurate with the non-uniform approximation, yet *subpar in order* relative to the asymptotic contribution of diffraction catastrophes summarized in Table 2. Accordingly the high-frequency distribution of topological sensitivity is, under the premise of single plane-wave incidence, asymptotically dominated by the caustics.

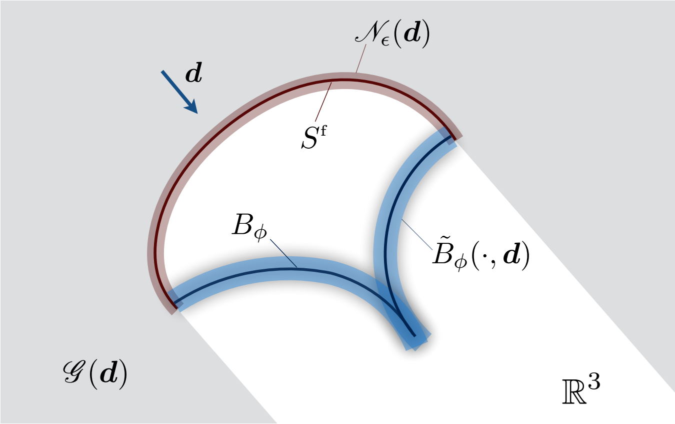

Figure 4. Schematics of the sets $\mathscr{N}_\epsilon$, $\tilde{B}_\phi$ and $\mathscr{G}$ featured in (4.1).

(b) Full source aperture

To expose the imaging ability of the TS indicator function, consider the full source aperture companion of (2.7), namely

$$\breve{\mathsf{T}}(\boldsymbol{x}^{\mathrm{o}}) \;=\; \int_{\Omega} \mathsf{T}(\boldsymbol{x}^{\mathrm{o}})\,\mathrm{d}\Omega_{\boldsymbol{d}}\,, \tag{4.3}$$

where the integration is performed over the direction $\boldsymbol{d}$ of incident plane wave, Ω is the unit sphere, and the dependence of T on $\boldsymbol{d}$ is implicit.

Proposition 4.1. *For given $\boldsymbol{x}^o \in \mathscr{B}_1$, every boundary point $\boldsymbol{\zeta} \in S$ becomes stationary point of type II for some unique incident direction $\boldsymbol{d} = \boldsymbol{d}^*(\boldsymbol{x}^o, \boldsymbol{\zeta})$ provided that $(\widehat{\boldsymbol{\zeta} - \boldsymbol{x}^o})\cdot\boldsymbol{n}(\boldsymbol{\zeta}) \neq 0$.*

Proof. From (3.11) one finds that for stationary points of type II, $\boldsymbol{d}^*$ must satisfy

$$\hat{\boldsymbol{r}}^{\pm} \;=\; \mp[\boldsymbol{d}^* + 2|\boldsymbol{d}^*\!\cdot\boldsymbol{n}|\,\boldsymbol{n}(\boldsymbol{\zeta}^{\pm}_{\mathrm{II}})]\,, \qquad \hat{\boldsymbol{r}}^{\pm} \;=\; \widehat{\boldsymbol{\zeta}^{\pm}_{\mathrm{II}} - \boldsymbol{x}^{\mathrm{o}}}, \tag{4.4}$$

subject to the condition $\boldsymbol{d}^*\!\cdot\boldsymbol{n}(\boldsymbol{\zeta}^{\pm}_{\mathrm{II}}) < 0$ to ensure $\boldsymbol{\zeta}^{\pm}_{\mathrm{II}} \in S^{\mathrm{f}}(\boldsymbol{d}^*)$. A contraction of (4.4) with $\boldsymbol{n}(\boldsymbol{\zeta}^{\pm}_{\mathrm{II}})$ yields $\boldsymbol{d}^*\!\cdot\boldsymbol{n}(\boldsymbol{\zeta}^{\pm}_{\mathrm{II}}) = \pm\,\hat{\boldsymbol{r}}^{\pm}\!\cdot\boldsymbol{n}(\boldsymbol{\zeta}^{\pm}_{\mathrm{II}})$, whereby

$$\boldsymbol{d}^*(\boldsymbol{x}^{\mathrm{o}},\boldsymbol{\zeta}) \;=\; \sigma\,[\boldsymbol{I} - 2\boldsymbol{n}\!\otimes\!\boldsymbol{n}(\boldsymbol{\zeta})]\,\hat{\boldsymbol{r}}\,, \quad \hat{\boldsymbol{r}} \;=\; \widehat{\boldsymbol{\zeta} - \boldsymbol{x}^{\mathrm{o}}}\,, \quad \sigma \;=\; \mathrm{sign}(\boldsymbol{n}\!\cdot\!\hat{\boldsymbol{r}}), \quad \sigma \neq 0. \tag{4.5}$$

Here $\boldsymbol{\zeta} \in S$ is a stationary point of type II for pair $(\boldsymbol{x}^{\mathrm{o}}, \boldsymbol{d}^*)$, and $[\boldsymbol{I} - 2\boldsymbol{n}\!\otimes\!\boldsymbol{n}]$ is an (orthogonal) reflection matrix. The uniqueness of $\boldsymbol{d}^*$ is then verified by contradiction noting that $\boldsymbol{n}(\boldsymbol{\zeta})$ is single-valued. □

Remark 3. *The uniqueness of $\boldsymbol{d}^*$ ceases at boundary points $\boldsymbol{\zeta}_o \in S$ where $\hat{\boldsymbol{r}}\cdot\boldsymbol{n}(\boldsymbol{\zeta}_o) = 0$. In particular, (4.4) demonstrates each $\boldsymbol{\zeta}_o$ is a stationary point of type II$^{\pm}$ when $\boldsymbol{d}^* = \mp\,\hat{\boldsymbol{r}}$. Their leading-order contribution to $\breve{\mathsf{T}}$, however, can be neglected since the slowly-varying components of the Fourier integrals in (3.4) vanish there due to the fact that $\boldsymbol{d}^*\!\cdot\boldsymbol{n}(\boldsymbol{\zeta}_o) = \hat{\boldsymbol{r}}\cdot\boldsymbol{n}(\boldsymbol{\zeta}_o) = 0$.*

Remark 4. *For $\boldsymbol{x}^o \in D$, one has $\hat{\boldsymbol{r}}\cdot\boldsymbol{n} \geqslant 0 \;\; \forall\boldsymbol{\zeta} \in S$. As a result, the stationarity type of every boundary point $\boldsymbol{\zeta}$ when $\boldsymbol{d} = \boldsymbol{d}^*(\boldsymbol{x}^o, \boldsymbol{\zeta})$ is II$^-$. When $\boldsymbol{x}^o \in \mathscr{B}_1 \backslash \overline{D}$, on the other hand, the boundary S of a Dirichlet obstacle can be split into subsets $S^{\pm}_{\mathrm{II}}(\boldsymbol{x}^o) = \{\boldsymbol{\zeta} \in S\colon \boldsymbol{d} = \boldsymbol{d}^*(\boldsymbol{x}^o, \boldsymbol{\zeta}) \to \boldsymbol{\zeta} = \boldsymbol{\zeta}^{\pm}_{\mathrm{II}}\}$, separated by a closed curve that is the locus of points $\boldsymbol{\zeta}_o$ where $\boldsymbol{d}^*\!\cdot\boldsymbol{n}(\boldsymbol{\zeta}_o) = 0$ (see Fig. 5(a)). When $\boldsymbol{x}^o \in \overline{D}$, these two subsets degenerate to $S^{+}_{\mathrm{II}} = \emptyset$ and $S^{-}_{\mathrm{II}} = S$.*

Remark 5. *For given $\boldsymbol{x}^o \in \mathscr{B}_1$, the bifurcation set $B_\phi(\boldsymbol{d}, \boldsymbol{x}^o)$ on the unit sphere spanned by $\boldsymbol{d}$ is a union of smooth curves and points where such curves join, intersect, or terminate as indicated in Fig. 5(b). Since $\mathrm{dim}(\Omega) = 2$, the only diffraction catastrophe affiliated with the* curves *in B_ϕ is of type fold (cod$(\phi) = 1$),*

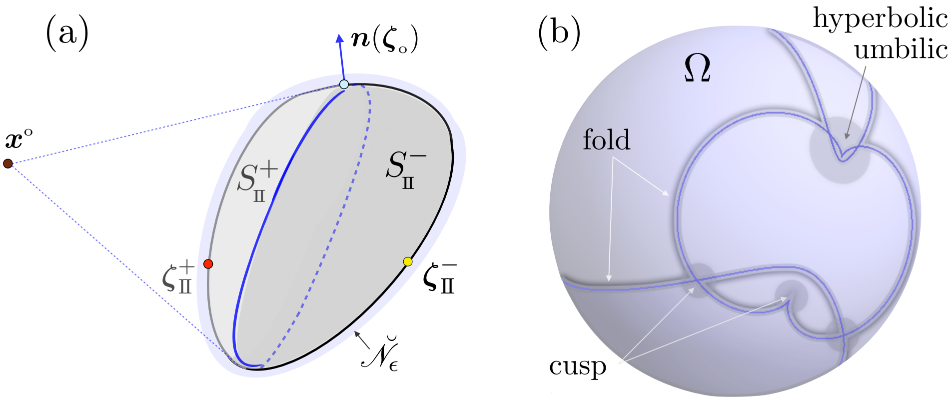

Figure 5. Schematics of the sets $S_{\rm II}^{\pm} \subset S$ and $B_\phi \subset \Omega$ for given $\boldsymbol{x}^\circ \in \mathscr{B}_1$: (a) Loci of the stationary points of type $\rm II^{\pm}$ when $\boldsymbol{d}$ spans Ω, and (b) bifurcation set $B_\phi(\boldsymbol{d}, \boldsymbol{x}^\circ)$ on the unit sphere, solid lines, surrounded by a narrow region $\tilde{B}_\phi$ (shaded area) where the non-uniform approximation fails.

while the higher-order catastrophes (cod$(\phi) > 1$) appear as points *[11] on Ω. In general, B_ϕ is contained within an open neighborhood $\tilde{B}_\phi$ where the non-uniform approximation fails, see also Fig. 4 for the schematics of $\tilde{B}_\phi$ in the physical space. On denoting by*

$$\boldsymbol{c} \,=\, \{c_m(\boldsymbol{d}, \boldsymbol{x}^o), \quad m = 1, ..., cod(\phi)\}$$

the minimal control space describing given diffraction catastrophe (see Section 3(c)), B_ϕ and $\tilde{B}_\phi$ can be formally specified as the level set $|\boldsymbol{c}| = 0$ *and* neighborhood $|\boldsymbol{c}| < k^{-\upsilon}$*, where $\upsilon > 0$ is a catastrophe-specific scaling parameter to be specified later. For completeness, it is noted that B_ϕ is* closed *for the assumption to the contrary would require cod$(\phi) = 0$ [23]. In the context of (4.5) relating (for given $\boldsymbol{x}^o$) $\boldsymbol{d} = \boldsymbol{d}^*$ to the stationary point(s) $\boldsymbol{\zeta} \in S$, the subset of S corresponding to $\tilde{B}_\phi$ is hereon denoted by $\tilde{S}_\phi$.*

In light of the above remarks, one may observe that a *discrete* set of critical points contributing to $\mathsf{T}(\boldsymbol{x}^\circ)$ in the case of a single incident wave, see (4.1), transitions in the course of full-aperture illumination into a *continuous* set S of all boundary points contributing to $\breve{\mathsf{T}}(\boldsymbol{x}^\circ)$. This suggests the possibility of a change of variable which remarkably facilitates the analysis. To introduce the idea, suppose that $\boldsymbol{x}^\circ \in \mathscr{B}_1 \backslash \{\breve{\mathscr{N}}_\epsilon \cup D\}$ and consider the integral of $\mathsf{T}^{\rm II^+}$ with respect to $\boldsymbol{d}$ as it contributes to (4.3). Next, recall that (4.5) provides the map relating $\boldsymbol{d} = \boldsymbol{d}^*$ to the solid angle of a boundary point with respect to $\boldsymbol{x}^\circ$, namely $\hat{\boldsymbol{r}}$. This map is *one-to-one* on account of the uniqueness of $\boldsymbol{\zeta}_{\rm II}^{+}$, see Appendix C. It is then straightforward to transform $\hat{\boldsymbol{r}}$ to $\boldsymbol{\zeta} \in S_{\rm II}^{+}$ (see Fig. 5) using the solid angle property $\mathrm{d}\Omega_{\hat{\boldsymbol{r}}} = \sigma\,(\hat{\boldsymbol{r}}\cdot\boldsymbol{n}/r^2)\,\mathrm{d}S_{\boldsymbol{\zeta}}$, whereby

$$\int_\Omega 1_{\mathscr{G}(\boldsymbol{d})}(\boldsymbol{x}^\circ)\, \mathsf{T}^{\rm II^+}(\boldsymbol{x}^\circ)\; \mathrm{d}\Omega_{\boldsymbol{d}} \;\;=\;\; -\int_{S_{\rm II}^{+}} \mathsf{T}^{\rm II^+}(\boldsymbol{x}^\circ)\; \frac{\hat{\boldsymbol{r}}\cdot\boldsymbol{n}}{r^2}\; \mathrm{d}S_{\boldsymbol{\zeta}}, \qquad r = |\boldsymbol{x}^\circ - \boldsymbol{\zeta}|. \tag{4.6}$$

When $\boldsymbol{x}^\circ \in \breve{\mathscr{N}}_\epsilon \backslash \overline{D}$, on the other hand, $\boldsymbol{\zeta}_{\rm II}^{+} \in \mathscr{B}^{k}_{\boldsymbol{x}^\star}$ and its contribution is computed via $\mathsf{T}^\star$, see Section 3(d). Hence $\mathscr{B}^{k}_{\boldsymbol{x}^\star} \cap S$ must be excluded from $S_{\rm II}^{+}$ in computing (4.6) via the concept of Van der Corput neutralizers [12, 16] (see also Appendix B, supplementary material). This tool is implicitly used in all cases where the partitioning of a domain of integration is in order.

The same change of variable can be applied to the integral over $\sum \mathsf{T}^{\rm II^-}$ in (4.1) with respect to $\boldsymbol{d}$. In this case, however, (4.5) is not one-to-one – which signifies the multiplicity of $\boldsymbol{\zeta}_{\rm II}^{-}$ and thus inherently accounts for the summation over $\mathsf{T}^{\rm II^-}$.

Lemma 4.2. *By way of (4.1), (4.3) and relationship $|\hat{\boldsymbol{r}}\cdot\boldsymbol{n}| = |\boldsymbol{d}^*\!\cdot\boldsymbol{n}|$, the full-aperture distribution $\breve{\mathsf{T}}$ can be recast as*

$$\breve{\mathsf{T}}(\boldsymbol{x}^o) \;\overset{k^\nu}{=}\; 1_{\breve{\mathscr{N}}_\epsilon}(\boldsymbol{x}^o) \int_\Omega \mathsf{T}^\star\; \mathrm{d}\Omega_{\boldsymbol{d}} \;+\; \int_{\tilde{B}_\phi} \mathsf{T}^c\; \mathrm{d}\Omega_{\boldsymbol{d}} \;+\; \int_{S^\pm} \frac{|\boldsymbol{d}^*\!\cdot\boldsymbol{n}|}{r^2}\, \mathsf{T}^{\rm II^\pm} \mathrm{d}S_{\boldsymbol{\zeta}}, \tag{4.7}$$

where $\nu \leqslant 1/2$; $\boldsymbol{d}^*$ *solves* (4.5); $\breve{\mathscr{N}}_\epsilon = \cup_{\boldsymbol{d}\in\Omega}\, \mathscr{N}_\epsilon(\boldsymbol{d})$ *is the "full-aperture" neighborhood of* S *constructed from* (3.5); $\mathsf{T}^\star = 0$ *for* $\boldsymbol{d}\cdot\boldsymbol{n}(\boldsymbol{x}^\star) > 0$;

$$S^{\pm} \;=\; S^{\pm}_{\mathrm{II}} \setminus \{1_{\breve{\mathscr{N}}_\epsilon}(\boldsymbol{x}^o)\, \mathscr{B}^k_{\boldsymbol{x}^\star} \cup \tilde{S}_\phi\}, \tag{4.8}$$

and $\mathscr{B}^k_{\boldsymbol{x}^\star}$ *is a ball of radius* $O(k^{-1})$ *centered at the normal projection* $\boldsymbol{x}^\star$ *of* $\boldsymbol{x}^o$ *on* S, *see Fig.* 3*(a). Geometrically, the respective support of* $\mathsf{T}^\star, \mathsf{T}^c$ *and* $\mathsf{T}^{\pm}$ *in* (4.7) *can be described as unit hemisphere, a small neighborhood of the bifurcation set* B_ϕ *on the unit sphere, and the boundary of the scatterer excluding its subsets contributing to* $\mathsf{T}^\star$ *and* T^c.

(i) Contribution of non-degenerate stationary points

Proposition 4.3. *The contribution of isolated stationary points to* $\check{\mathsf{T}}$ *in* (4.7) *scales as*

$$\int_{S^\pm} \frac{|\boldsymbol{d}^*\!\cdot\boldsymbol{n}|}{r^2}\, \mathsf{T}^{\mathrm{II}^{\pm}}\, \mathrm{d}S_{\boldsymbol{\zeta}} \;=\; O(k^\alpha), \qquad 0 \leqslant \alpha \leqslant \tfrac{1}{3} \tag{4.9}$$

for sufficiently large k, *assuming the codimension of phase singularities in the featured integral not to exceed three.*

Proof. By way of (3.17) and (3.19), the left-hand side of (4.9) can be rewritten as a Fourier integral

$$k\ \mathrm{Im}\bigg[\int_{S^\pm} F^{\pm}(\boldsymbol{\zeta})\, e^{\pm 2\mathrm{i}kr|\boldsymbol{d}^*\cdot\boldsymbol{n}|^2}\, \mathrm{d}S_{\boldsymbol{\zeta}}\bigg], \qquad |\boldsymbol{d}^*\!\cdot\boldsymbol{n}| \;=\; |(\widehat{\boldsymbol{\zeta}-\boldsymbol{x}^{\mathrm{o}}})\cdot\boldsymbol{n}(\boldsymbol{\zeta})|, \tag{4.10}$$

where $S^\pm$ is such that $r > 2\pi k^{-1}$ thanks to (4.8), and

$$k \int_{S^\pm} \big|F^{\pm}(\boldsymbol{\zeta})\big|\, \mathrm{d}S_{\boldsymbol{\zeta}} \;=\; O(k).$$

In this setting, the leading asymptotic behavior of (4.10) is governed by critical points of the phase function $r|\boldsymbol{d}^*\!\cdot\boldsymbol{n}|^2$ which satisfy

$$2|\boldsymbol{d}^*\!\cdot\boldsymbol{n}| \left[\sigma\boldsymbol{n} - \frac{|\boldsymbol{d}^*\!\cdot\boldsymbol{n}|}{2}(\widehat{\boldsymbol{\zeta}-\boldsymbol{x}^{\mathrm{o}}}) + \frac{\boldsymbol{d}^*\!\cdot\boldsymbol{a}_1}{\rho_1}\, r\boldsymbol{a}_1 + \frac{\boldsymbol{d}^*\!\cdot\boldsymbol{a}_2}{\rho_2}\, r\boldsymbol{a}_2\right]\cdot\frac{\partial\boldsymbol{\zeta}}{\partial\eta^p} \;=\; \boldsymbol{0}, \tag{4.11}$$

where $\sigma = \mathrm{sign}(\boldsymbol{n}\cdot\hat{\boldsymbol{r}})$ and $\rho_{1/2}$ are the principal radii of curvature of $S^\pm$ at $\boldsymbol{\zeta}$. From the definition of $S^\pm$ in (4.8), the relevant roots of (4.11) represent the normal projection of $\boldsymbol{x}^{\mathrm{o}}$ on S, i.e.

$$\big|(\widehat{\boldsymbol{\zeta}-\boldsymbol{x}^{\mathrm{o}}})\cdot\boldsymbol{n}(\boldsymbol{\zeta})\big| \;=\; 1. \tag{4.12}$$

Over S^+, the solution of (4.12) is unique due to the convexity and smoothness of S, whereby the phase function in this case possesses a single isolated stationary point. From (3.8), one accordingly finds that the integral over S^+ in (4.9) scales as $O(1)$.

On the other hand, the normal projection of $\boldsymbol{x}^{\mathrm{o}}$ on S^- is generally not unique. In this case, it can be shown via (4.8) and (4.11) that the Hessian of $r|\boldsymbol{d}\cdot\boldsymbol{n}|^2$ becomes singular at a critical point $\boldsymbol{\zeta} \in S^-$ solving (4.12) only if

$$|\boldsymbol{\zeta} - \boldsymbol{x}^{\mathrm{o}}| \;=\; \rho_{1/2}(\boldsymbol{\zeta}). \tag{4.13}$$

Making an appeal to the analysis in Section 3(c) and Appendix B, one subsequently finds that the integral over S^- in (4.9), on accounting for catastrophes where (4.12) and (4.13) both hold, may include contributions of orders shown in Table 2. □

Table 3. Leading-order contribution in (4.9) of the critical points over S^- to $\check{\mathsf{T}}(\boldsymbol{x}^{\mathrm{o}},\cdot,\cdot)$

Catastrophe of $r\lvert\boldsymbol{d}^*\!\cdot\boldsymbol{n}\rvert^2$	None	Fold	Cusp	Swallowtail	Hyperbolic umbilic	Elliptic umbilic
Contribution	$O(1)$	$O(k^{1/6})$	$O(k^{1/4})$	$O(k^{3/10})$	$O(k^{1/3})$	$O(k^{1/3})$

(ii) Contribution of diffraction catastrophes

Proposition 4.4. *For sufficiently large k, the contribution of caustics to $\check{\mathsf{T}}$ in (4.7) behaves as*

$$\int_{\tilde{B}_\phi} \mathsf{T}^c \;\mathrm{d}\Omega_{\boldsymbol{d}} \;=\; O(k^\alpha), \qquad \tfrac{1}{4} \leqslant \alpha \leqslant \tfrac{2}{3}. \tag{4.14}$$

Proof. The idea behind establishing (4.14) is to expose the measure of the vanishing support, $|\tilde{B}_\phi|$, of a region on the unit sphere where the non-uniform approximation fails – indicated by the shaded area in Fig. 5(b). In particular as $\boldsymbol{d}$ (for given $\boldsymbol{x}^{\text{o}}$) leaves the neighborhood $\tilde{B}_\phi \subset \Omega$ of the bifurcation set, special functions involved in describing the diffraction catastrophes, denoted by

$$\Psi(k^{\sigma_1} c_1, \ldots, k^{\sigma_M} c_M), \qquad M = \mathrm{cod}(\phi) < 4 \tag{4.15}$$

(see Section 3(c) and Appendix B), approach their large-argument asymptotics [25] due to growing magnitude, $|\boldsymbol{c}| = (c_1^2 + \cdots + c_M^2)^{1/2}$, of the featured minimal control space. This in turn reduces the germane *uniform* approximation to either its non-uniform counterpart, or zero – on the dark side of some caustics (e.g. fold) due to absence of real stationary points [40]. On denoting $b_m = k^{\sigma_m} c_m$, such transition in (4.15) occurs when $(b_1^2 + \cdots + b_M^2)^{1/2} = O(1)$, see Fig. 14 in Appendix B (supplementary material) as an example. Accordingly, one obtains

$$|\boldsymbol{c}| \;\leqslant\; O(k^{-\sigma_m^{\text{min}}}), \qquad \sigma_m^{\text{min}} \;=\; \min\{\sigma_1, \ldots, \sigma_M\} > 0 \tag{4.16}$$

as a *sufficient condition* for estimating the extent of $\tilde{B}_\phi$, where σ_m^{min} are given in Table 2.

The next step in the analysis is to establish (for given $\boldsymbol{x}^{\text{o}}$) a *linearized* relationship between $|\boldsymbol{c}|$ and $\mathrm{dist}(\boldsymbol{d}, B_\phi)$ on the unit sphere, in a small neighborhood of the bifurcation set. In the context of Fig. 5(b), it is recalled that the fold caustics ($\mathrm{cod}(\phi) = 1$) translate into smooth non-intersecting curves in $B_\phi \subset \Omega$, while the catastrophes of higher codimension are projected as points in B_ϕ. In this setting, $\mathrm{dist}(\boldsymbol{d}, B_\phi)$ is identified as the normal spherical distance to a curve (resp. spherical distance to a point) when $\mathrm{cod}(\phi) = 1$ (resp. $\mathrm{cod}(\phi) > 1$). On writing the sought relationship as $|\boldsymbol{c}| = V \cdot \mathrm{dist}(\boldsymbol{d}, B_\phi)$, one finds from (4.16) that

$$\tilde{B}_\phi \;=\; \big\{ \boldsymbol{d} \in \Omega : \, \mathrm{dist}(\boldsymbol{d}, B_\phi) \leqslant V^{-1} O(k^{-\sigma_m^{\text{min}}}) \big\} \tag{4.17}$$

for sufficiently large k, noting that $V > 0$ since the bifurcation set $B_\phi \subset \Omega$ is *closed* (see Remark 5).

To estimate V, consider first a *fold* bifurcation point $\boldsymbol{d}^{\text{o}} \in B_\phi$ for given $\boldsymbol{x}^{\text{o}}$, and let $\boldsymbol{\zeta}^* \in S$ denote the affiliated critical point on the boundary of the scatterer. In this case $\boldsymbol{c} = c$, and the Hessian of ϕ is of corank one. On account of the Splitting Lemma (3.23) and Taylor expansion of $\phi(\boldsymbol{\zeta})$ about $\boldsymbol{\zeta}^*$, there exist local surface coordinates (σ, τ) such that

$$\phi(\boldsymbol{\zeta})\big|_{\boldsymbol{d}^{\text{o}}} \simeq \phi_\circ + \tfrac{1}{2}\phi_\circ^{(2)}\sigma^2 + \tfrac{1}{6}\,\phi_\circ'''\,\tau^3, \quad \phi_\circ^{(2)} = \frac{\partial^2\phi}{\partial\sigma^2}\Big|_{\boldsymbol{\zeta}^*}, \quad \phi_\circ''' = \frac{\partial^3\phi}{\partial\tau^3}\Big|_{\boldsymbol{\zeta}^*}, \quad \boldsymbol{\zeta} \simeq \boldsymbol{\zeta}^* + \sigma\,\hat{\boldsymbol{s}} + \tau\,\hat{\boldsymbol{t}} \tag{4.18}$$

where $\phi_\circ = \phi(\boldsymbol{\zeta}^*)$; $\phi_\circ^{(2)}$ and $\phi_\circ'''$ are $O(1)$, and $(\hat{\boldsymbol{s}}, \hat{\boldsymbol{t}})$ are the unit vectors tangent to (σ, τ) at $\boldsymbol{\zeta}^*$, used to describe $\boldsymbol{\zeta}$ to the leading order. The objective is to find the variation in c due to infinitesimal perturbation $\mathrm{d}\boldsymbol{d} \perp \boldsymbol{d}^{\text{o}}$. Using (4.18) and definition $\phi = \boldsymbol{\zeta}\cdot\boldsymbol{d} - r$ where $r = |\boldsymbol{x}^{\text{o}} - \boldsymbol{\zeta}|$, one finds

$$\phi(\boldsymbol{\zeta})\big|_{\boldsymbol{d}^{\text{o}}+\mathrm{d}\boldsymbol{d}} \simeq \tilde{\phi}_\circ + \tfrac{1}{2}\phi_\circ^{(2)}\sigma^2 + (\mathrm{d}\boldsymbol{d}\cdot\hat{\boldsymbol{s}})\,\sigma + \tfrac{1}{6}\,\phi_\circ'''\,\tau^3 + (\mathrm{d}\boldsymbol{d}\cdot\hat{\boldsymbol{t}})\,\tau, \qquad \tilde{\phi}_\circ = \phi_\circ + \mathrm{d}\boldsymbol{d}\cdot\boldsymbol{\zeta}^*. \tag{4.19}$$

By considering the *fold* universal unfolding as in Table 2, one finds from (4.19) via mapping $t = (|\phi_\circ'''|/2)^{1/3}\tau$ that

$$|c| \;=\; \big|\tfrac{1}{2}\phi_\circ'''\big|^{-\frac{1}{3}}\;|\mathrm{d}\boldsymbol{d}\cdot\hat{\boldsymbol{t}}|.$$

When $\mathrm{d}\boldsymbol{d}$ is parallel to $\boldsymbol{d}^{\text{o}} \times \hat{\boldsymbol{t}}$, c remains zero to the leading order. This shows that $\boldsymbol{d}^{\text{o}} \times \hat{\boldsymbol{t}}$ is *tangent* to the fold curve at $\boldsymbol{d}^{\text{o}} \in B_\phi$. Subsequently, the width of a stripe-like region $\tilde{B}_\phi$ surrounding B_ϕ is exposed by considering $\mathrm{d}\boldsymbol{d}$ in the plane containing $\boldsymbol{d}^{\circ}$ and $\hat{\boldsymbol{t}}$, which yields

$$|\mathrm{d}\boldsymbol{d}\cdot\hat{\boldsymbol{t}}| \;=\; |\mathrm{d}\boldsymbol{d}|\sqrt{|\boldsymbol{d}^{\circ}\!\cdot\boldsymbol{n}|^2+\sin(\vartheta)^2(1-|\boldsymbol{d}^{\circ}\!\cdot\boldsymbol{n}|^2)} \geqslant |\mathrm{d}\boldsymbol{d}|\,|\boldsymbol{d}^{\circ}\!\cdot\boldsymbol{n}| \quad\Rightarrow\quad V \geqslant \left|\tfrac{1}{2}\phi_{\circ}'''\right|^{-\frac{1}{3}}\,|\boldsymbol{d}^{\circ}\!\cdot\boldsymbol{n}|, \tag{4.20}$$

where $|\mathrm{d}\boldsymbol{d}| = \mathrm{dist}(\boldsymbol{d}, B_\phi)$, $\boldsymbol{n} = \boldsymbol{n}(\boldsymbol{\zeta}^*)$, and ϑ is the angle between $\hat{\boldsymbol{t}}$ and the plane containing $\boldsymbol{d}^{\circ}$ and $\boldsymbol{n}$. From (4.17), (4.20) and Table 2, one finds an upper-bound estimate

$$|\tilde{B}_\phi|_{\mathrm{cod}(\phi)=1} \;=\; O\big(|\boldsymbol{d}^{\circ}\!\cdot\boldsymbol{n}|^{-1}\,k^{-\sigma_m^{\min}}\big) \;=\; O\big(|\boldsymbol{d}^{\circ}\!\cdot\boldsymbol{n}|^{-1}\,k^{-2/3}\big). \tag{4.21}$$

Note that the integrands (3.6) underpinning T^c scale with $|\boldsymbol{d}^{\circ}\!\cdot\boldsymbol{n}|$, so that the situations of widening $\tilde{B}_\phi$ when $|\boldsymbol{d}^{\circ}\!\cdot\boldsymbol{n}| \to 0$ pose no problem in terms of the contribution of the fold catastrophes to (4.14).

From (4.20), it is seen that the sole situation precluding $V = O(1)$ is $|\boldsymbol{d}^{\circ}\!\cdot\boldsymbol{n}(\boldsymbol{\zeta}^*)| \ll 1$. As shown in Appendix A(b), this requires that the distance between $\boldsymbol{x}^{\circ}$ and the critical point, $|\boldsymbol{x}^{\circ} - \boldsymbol{\zeta}^*|$, behaves as $O(|\boldsymbol{d}^{\circ}\!\cdot\boldsymbol{n}|^{\pm 1})$, see also Fig. 15. Due to the regularity of S, however, catastrophes with $\mathrm{cod}(\phi) > 1$ cannot occur arbitrarily close to S, while the sampling points where $|\boldsymbol{x}^{\circ} - \boldsymbol{\zeta}^*| \gg 1$ are outside of $\mathscr{B}_1$. As a result, $V = O(1)$ for higher-codimension catastrophes and consequently

$$|\tilde{B}_\phi|_{\mathrm{cod}(\phi)>1} \;=\; O\big(k^{-2\sigma_m^{\min}}\big), \tag{4.22}$$

where $\sigma_m^{\min}$ are given in Table 2, and factor 2 in the exponent arises from the fact that $\tilde{B}_\phi|_{\mathrm{cod}(\phi)>1}$ assembles the neighborhoods of *isolated points*, see Fig. 5(b). The claim (4.14) then follows from the scaling of T^c in Table 2, (3.6), (4.21), and (4.22). For completeness, the effect on (4.14) due to error of the Kirchhoff approximation (3.1) is examined in Appendix D (supplementary material). ☐

(iii) Contribution of nearby critical points for $\boldsymbol{x}^{\circ} \in \breve{\mathscr{N}}_\epsilon$

Proposition 4.5. *For $\boldsymbol{x}^{o} \in \breve{\mathscr{N}}_\epsilon$, the contribution of nearby critical points to $\breve{\mathsf{T}}$ in (4.7) is given by*

$$\int_{\Omega} \mathsf{T}^\star\,\mathrm{d}\Omega_{\boldsymbol{d}} \;\overset{1}{=}\; \frac{\pi k}{(k\ell)^3}\left\{\mathsf{A}\left(\mathsf{k}\ell\cos(\mathsf{k}\ell)-\sin(\mathsf{k}\ell)\right)^2+\mathsf{B}\,(\mathsf{k}\ell)^2\sin(\mathsf{k}\ell)^2\right\} \tag{4.23}$$

for sufficiently large k, where $\ell = (\boldsymbol{x}^{o} - \boldsymbol{x}^\star)\cdot\boldsymbol{n}(\boldsymbol{x}^\star)$ is the signed normal distance between $\boldsymbol{x}^{o}$ and the boundary of the scatterer.

Proof. The single-incident-wave expression for $\mathsf{T}^\star(\boldsymbol{x}^{\circ},\cdot,\cdot)$, given by (3.36), is explicit and permits direct integration with respect to $\boldsymbol{d}$. Recall that $\mathsf{T}^\star = 0$ for $\boldsymbol{d}\cdot\boldsymbol{n}(\boldsymbol{x}^\star) \geqslant 0$ thanks to (3.1), whereby the effective integration support in (4.23) is a hemisphere. By taking $-\boldsymbol{n}(\boldsymbol{x}^\star)$ as the zenith direction of the spherical coordinate system describing Ω, it is evident from (3.36) that $\mathsf{T}^\star$ is exclusively a function of the zenith angle $|\boldsymbol{d}\cdot\boldsymbol{n}(\boldsymbol{x}^\star)| = \cos\theta$ and $k\ell$ so that

$$\int_{\Omega} \mathsf{T}^\star\,\mathrm{d}\Omega_{\boldsymbol{d}} \;=\; \int_0^{2\pi}\!\!\int_0^{\pi/2} [\mathsf{T}^\star](\cos\theta, k\ell)\,\sin\theta\,\mathrm{d}\theta\,\mathrm{d}\varphi \;=\; 2\pi\int_0^1 [\mathsf{T}^\star](\tau, k\ell)\,\mathrm{d}\tau, \tag{4.24}$$

resulting immediately in (4.23). ☐

Remark 6. *As discussed in Remark 2, Proposition 4.5 is established under the premise that a hidden obstacle D is sound-soft. Accordingly, it is of interest to examine the near-boundary variation (4.23) when $(\mathsf{A},\mathsf{B}) = (0,1)$, i.e. when the vanishing perturbation in (2.6) is likewise of Dirichlet type (see Table 1). This behavior is shown in Fig. 6(a), which plots (4.23) with $(\mathsf{A},\mathsf{B}) = (0,1)$ versus $k\ell$ in a neighborhood of ∂D. As can be seen from the graph, the leading contribution of $\mathsf{T}^\star$ to $\breve{\mathsf{T}}$ in such case (i) crosses zero precisely at ∂D, and (ii) attains extreme negative (resp. positive) value at its first peak inside (resp. outside) the obstacle, at a normal distance of $|k\ell| < \pi/2$ from the boundary. For completeness, Fig. 6(b) plots the corresponding distribution of (4.23) assuming $(\mathsf{A},\mathsf{B}) = (3/2,-1)$, i.e. taking the vanishing obstacle to be of "wrong" i.e. Neumann type. From the display, one sees that the near-boundary variation of (4.23) assuming sound-hard vanishing obstacle is visibly less localized than that using sound-soft perturbation in Fig. 6(a). This observation will motivate the proposed TS algorithm for high-frequency obstacle reconstruction.*

The foregoing developments are now concluded with the main result of this work.

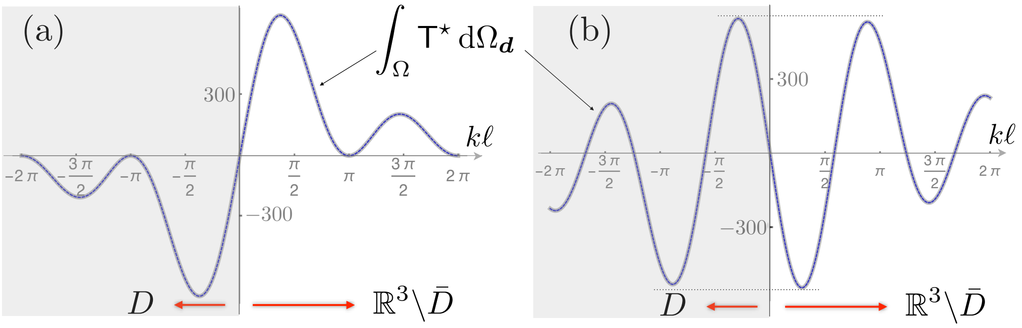

Figure 6. Contribution of $\mathsf{T}^\star$ to $\breve{\mathsf{T}}$ at $k = 300$ versus normal distance to the boundary of an extended Dirichlet obstacle: (a) local variation assuming $(\mathsf{A}, \mathsf{B}) = (0, 1)$, and (b) variation assuming $(\mathsf{A}, \mathsf{B}) = (3/2, -1)$.

Theorem 4.6. *Consider the inverse scattering problem for a convex Dirichlet obstacle D as in Fig. 1 with far-field sensory data. For sufficiently large k, the full-source-aperture distribution of the scaled TS indicator (2.6) behaves as*

$$\breve{\mathsf{T}}(\boldsymbol{x}^{\mathrm{o}}) \;\overset{k^\alpha}{=}\; 1_{\breve{\mathscr{N}}_\epsilon}(\boldsymbol{x}^{\mathrm{o}}) \, \frac{\pi k}{(k\ell)^3} \left\{ \mathsf{A} \left(k\ell \cos(k\ell) - \sin(k\ell) \right)^2 + \mathsf{B} \, (k\ell)^2 \sin(k\ell)^2 \right\}, \qquad \alpha \leqslant 2/3 \qquad (4.25)$$

under the premise of diffraction catastrophes with codimension less than four, where $\breve{\mathscr{N}}_\epsilon$ is a 2ϵ-thick shell (for some $\epsilon = O(k^{-1}) \geqslant 2\pi/k$) with mid-plane ∂D; $\ell = (\boldsymbol{x}^{\mathrm{o}} - \boldsymbol{x}^\star) \cdot \boldsymbol{n}(\boldsymbol{x}^\star)$ is the signed normal distance between $\boldsymbol{x}^{\mathrm{o}}$ and ∂D, and the coefficient pair (A, B) takes values as in Table 1 depending of the type of (impenetrable) vanishing perturbation used to probe the domain.

Proof. The claim is a direct consequence of Lemma 4.2 and Propositions 4.3–4.5. As shown in Appendix D, the result is resilient to the error due to Kirchhoff approximation (3.1). ☐

Remark 7. *Note that (4.25) ensures the high-frequency reconstruction of a Dirichlet obstacle assuming full source aperture ($\boldsymbol{d} \in \Omega$). At a glance, such requirement may appear excessive in light of the uniqueness-of-reconstruction result for sound-soft obstacles (Corollary 5.3 in [22]) with only a single incident plane wave. As examined in [30], however, the latter claim holds only for scatterers contained within a ball of radius $R_\circ \simeq 4.49/k$ – which inherently precludes the high-wavenumber case considered herein. Indeed the numerical results in Sec. 5 (see for instance Fig. 9) demonstrate that, at wavelengths that are small relative to the obstacle size, the TS reconstruction with a singe incident plane wave provides no information about the "dark side" of the obstacle. On the other hand, from Theorem 5.1 in [22] it follows that the above uniqueness result does hold for any wavenumber k provided that the obstacle is illuminated by an infinite number of incident plane waves – which is consistent with the claim of Theorem 4.6.*

(c) Neumann obstacle

For a sound-hard obstacle, the physical optics approximation [12] reads

$$u \;=\; \left\{ \begin{array}{ll} 2\,u^i & \text{on} \quad S^{\mathrm{f}} \\ 0 & \text{on} \quad S^{\mathrm{b}} \end{array} \right. , \qquad u_{,n} = 0 \quad \text{on} \quad S = \partial D. \qquad (4.26)$$

Applying this condition with $u^i = e^{-\mathrm{i}k\boldsymbol{x}\cdot\boldsymbol{d}}$ to (2.8), followed by the use of (2.13) and (2.14) to address the component integrals over Γ^{obs}, results in a TS formula for Neumann obstacle that is structurally similar to (3.3). In particular, the kernel in the "sound-hard" counterpart of (3.3) can be shown to (i) feature the identical phase function $\boldsymbol{\zeta}\cdot\boldsymbol{d} \pm r$, (ii) remain regular as $\boldsymbol{x}^{\mathrm{o}} \to S^{\mathrm{f}}$, and (iii) vanish on ∂S^{f}. The end result of the analysis is given by the following statement.

Theorem 4.7. *Consider the inverse scattering problem for a convex Neumann obstacle D as in Fig. 1 with far-field sensory data. For sufficiently large k, the full-source-aperture distribution of the scaled TS* *indicator* (2.6) *behaves as*

$$\breve{\mathsf{T}}(\boldsymbol{x}^o) \overset{k^\alpha}{=} 1_{\breve{\mathscr{N}}_\epsilon}(\boldsymbol{x}^o)\, \frac{-\pi k}{(k\ell)^3} \Big\{ \mathsf{A}\, \big(\mathrm{k}\ell \cos(\mathrm{k}\ell) - \sin(\mathrm{k}\ell)\big)^2 + \mathsf{B}\, (\mathrm{k}\ell)^2 \sin(\mathrm{k}\ell)^2 \Big\}, \qquad \alpha \leqslant 2/3 \tag{4.27}$$

under the premise of diffraction catastrophes with codimension less than four, where $\breve{\mathscr{N}}_\epsilon$ *is a* 2ϵ*-thick shell (for some* $\epsilon = O(k^{-1}) \geqslant 2\pi/k$*) with mid-plane* ∂D*;* $\ell = (\boldsymbol{x}^o - \boldsymbol{x}^\star)\cdot \boldsymbol{n}(\boldsymbol{x}^\star)$ *is the signed normal distance between* $\boldsymbol{x}^o$ *and* ∂D*, and the coefficient pair* (A, B) *takes values as in Table 1 depending of the type of (impenetrable) vanishing perturbation used to probe the domain.*

Proof. Claim (4.27) is established by the steps analogous to those entailed in the proof of (4.25), see Appendix E (supplementary material) for details. ☐

(d) Unscaled TS distribution

To establish a direct link with the results of earlier TS studies on impenetrable obstacles [e.g. 38], it is of interest to rewrite (4.25) and (4.27) in terms of the original (i.e. unscaled) TS formula (2.5), and to further assume *prior knowledge* of obstacle type by letting $(\mathsf{A}, \mathsf{B}) = (0, 1)$ (resp. $(3/2, -1)$) when reconstructing hidden Dirichlet (resp. Neumann) anomalies. On recalling the relationship $T(\boldsymbol{x}^\text{o}) = k^{-\gamma}\,\mathsf{T}(\boldsymbol{x}^\text{o})$ according to (2.6) and Table 1, one consequently finds from Theorem 4.6 and Theorem 4.7 that

$$\begin{aligned} \breve{T}(\boldsymbol{x}^\text{o}) \;&=\; k^{-2}\, \breve{\mathsf{T}}|_{(\mathsf{A},\mathsf{B})=(0,1)} \\ &\overset{k^\alpha}{=}\; 1_{\breve{\mathscr{N}}_\epsilon}(\boldsymbol{x}^\text{o})\, \frac{\pi\, k^{-1}}{(k\ell)} \Big\{ \sin(k\ell)^2 \Big\}, \qquad \alpha \leqslant -4/3 \end{aligned} \tag{4.28}$$

in the case of *Dirichlet* obstacles probed by sound-soft perturbations, and

$$\begin{aligned} \breve{T}(\boldsymbol{x}^\text{o}) \;&=\; \breve{\mathsf{T}}|_{(\mathsf{A},\mathsf{B})=(3/2,-1)} \\ &\overset{k^\alpha}{=}\; 1_{\breve{\mathscr{N}}_\epsilon}(\boldsymbol{x}^\text{o})\, \frac{-\pi\, k}{(k\ell)^3} \Big\{ \tfrac{3}{2} \big(k\ell \cos(k\ell) - \sin(k\ell)\big)^2 - (k\ell)^2 \sin(k\ell)^2 \Big\}, \qquad \alpha \leqslant 2/3 \end{aligned} \tag{4.29}$$

in terms of *Neumann* anomalies probed by sound-hard perturbations. As can be seen from (4.28) and (4.29), the two (unscaled) asymptotic behaviors are quite distinct, yet both localized near ∂D. This can be verified by noting that the Dirichlet variation (4.28) is, up to the factor k^{-2}, given by Fig. 6(a), while the Neumann variation (4.29) is – up to the sign factor – shown in Fig. 6(b).

(e) Reconstruction scheme

A comparison between (4.25) and (4.27) reveals that for (A, B) *fixed*, the leading-order behavior of $\breve{\mathsf{T}}$ simply *changes sign* when (2.6) is applied toward the reconstruction of a *hidden Dirichlet* vs. *hidden Neumann* obstacle. Accordingly, the counterpart of Fig. 6 for a hidden Neumann anomaly is obtained via reflection of the featured diagrams about the $k\ell$-axis. This opens two distinct avenues toward the high-frequency TS reconstruction of impenetrable obstacles:

Algorithm 1. When the nature of D is known beforehand, (i) compute $\breve{\mathsf{T}}(\boldsymbol{x}^\text{o})$ with commensurate trial parameters ($(\mathsf{A}, \mathsf{B}) = (0, 1)$ for Dirichlet anomaly, $(\mathsf{A}, \mathsf{B}) = (3/2, -1)$ for Neumann anomaly) and (ii) reconstruct ∂D as the *zero level set* of $\breve{\mathsf{T}}$ separating its extreme negative and extreme positive values. The extreme $\breve{\mathsf{T}}$-values inside the reconstruction are always *negative*.

Algorithm 2. When the nature of D is *unknown*, compute $\breve{\mathsf{T}}(\boldsymbol{x}^\text{o})$ with $(\mathsf{A}, \mathsf{B}) = (0, 1)$ and reconstruct ∂D as the *zero level set* of $\breve{\mathsf{T}}$ separating its extreme negative and extreme positive values. When the extreme $\breve{\mathsf{T}}$-values to the *inside* of the reconstruction are negative (resp. positive), the impenetrable obstacle is of Dirichlet (resp. Neumann) type.

In this setting, Algorithm 2 is generally preferred due the to the facts that: (a) the obstacle type is *revealed* rather than required as prior information, and (b) setting $(\mathsf{A}, \mathsf{B}) = (0, 1)$ (as opposed to $(\mathsf{A}, \mathsf{B}) = (3/2, -1)$) allows for *stronger localization* of the extreme $\breve{\mathsf{T}}$-values near ∂D, see Fig. 6.

5. Numerical results

A computational experiment is devised to illustrate the performance of the TS as an imaging tool in the high-frequency regime. The focus is on elucidating how does (3.3) relate to the boundary of a convex Dirichlet obstacle, and how is the numerical distribution thereof approximated by the closed-form expression (4.25) in the case of the full source aperture. The sensing arrangement is shown in Fig. 7(a), where D is an ellipsoidal anomaly with semi-axes $(0.2, 0.08, 0.8)$. In what follows, the TS distribution is computed in the obstacle's mid-section $\mathit{\Pi}$ perpendicular to its major axis, assuming incident plane waves with $k = 300$ (wavelength $\lambda = 0.021$) propagating in direction $\boldsymbol{d} \,\|\, \mathit{\Pi}$. In this case, the computation of TS is facilitated by two critical observations: i) for $\boldsymbol{x}^{\mathrm{o}}$ within the square "patch" shown in Fig. 7(a), the critical points on S^{f} are confined to $S^{\mathrm{f}} \cap \mathit{\Pi}$, and ii) the germane catastrophes are of either type fold or cusp, i.e. $\mathrm{cod}(\phi) \leqslant 2$. Note, however, that the caustics of higher codimension may occur in out-of-plane situations – when either $\boldsymbol{d} \nparallel \mathit{\Pi}$ or $\boldsymbol{x}^{\mathrm{o}} \notin \mathit{\Pi}$ – see Fig. 7(b) for an example projection of the bifurcation set $B_\phi(\boldsymbol{d}, \boldsymbol{x}^{\mathrm{o}})$ on $\mathit{\Omega}$.

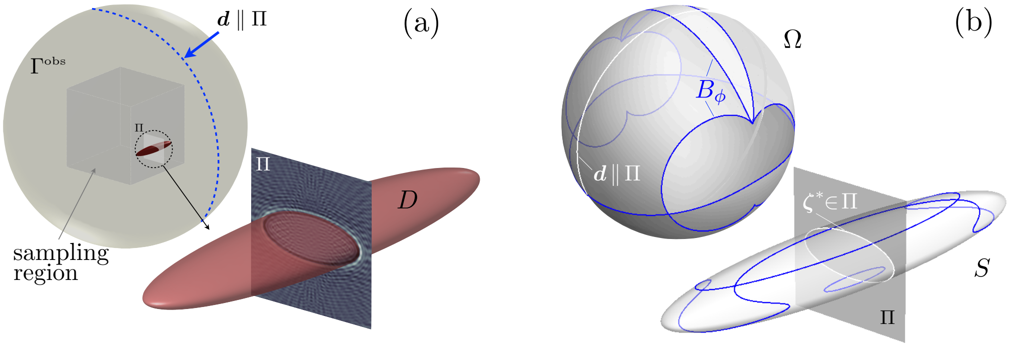

Figure 7. Example problem: (a) sensing configuration, and (b) bifurcation set $B_\phi(\boldsymbol{d}, \boldsymbol{x}^{\mathrm{o}}) \subset \mathit{\Omega}$ with affiliated critical points $\boldsymbol{\zeta}^* \in S$ (dark curves) for the sampling point $\boldsymbol{x}^{\mathrm{o}} = \boldsymbol{p}$ shown in Fig. 9(b). Loci $\boldsymbol{d} \,\|\, \mathit{\Pi}$ and matching $\boldsymbol{\zeta}^*$ are shown in white.

(a) Applicability of Kirchhoff approximation

One may recall that the implicit assumptions behind (3.3) – used hereon as the basis for numerical evaluation of TS – are that: i) the sensory data are of far-field type (see Remark 1), and ii) the Kirchhoff approximation (3.1) applies. In this setting, it is of interest to assess the accuracy of (3.1) for the testing configuration described above. Due to lack of suitable 3D solutions, the validation is performed in a two-dimensional setting, assuming scattering by a sound-soft *cylinder* whose cross-section equals $S \cap \mathit{\Pi}$ in Fig. 7. With such premise, Fig. 8 compares the analytical solution [17] for the far-field pattern, $\tilde{u}_\infty$, of the scattered field given by

$$\tilde{u}(\boldsymbol{x}) \;=\; \frac{e^{\mathrm{i}kR}}{\sqrt{kR}}\,\tilde{u}_\infty(\alpha), \qquad R = |\boldsymbol{x}| \to \infty,$$

with that stemming from the Kirchhoff approximation. As can be seen from the display, the agreement between the two solutions is rather satisfactory.

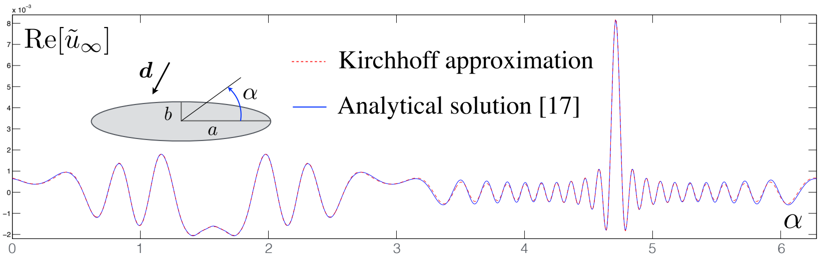

Figure 8. Far-field pattern at $k = 300$ of the scattered field generated by an infinite sound-soft cylinder with $a = 0.2$, $b = 0.08$ and $\boldsymbol{d} = (0, 1)$. The relative error (L^2-norm) committed by the Kirchhoff approximation is less than 6%.

(b) Single plane-wave incidence

With the aid of the high-frequency approximations described in Section 3 and Appendix B, the TS field (4.1) is computed via the following steps: i) the 0.5×0.5 square computational domain within Π (see Fig. 7(a)) is discretized by 10^6 pixels, nearly 42 per wavelength; ii) the boundary curve $S^{\mathrm{f}}(\boldsymbol{d}) \cap \Pi$ is split into 10^4 segments centered at $\boldsymbol{\zeta}^n$, $n = \overline{1, 10^4}$; and iii) starting from $\boldsymbol{\zeta}^1$, the contribution of $\boldsymbol{\zeta}^n$ to (4.1) is computed (via either near-boundary, uniform, or non-uniform approximation) along rays $\mathrm{II}^{\pm} \in \Pi$, and accordingly used to "paint" the pixels. In doing so, the use is made of the Van der Corput neutralizers [12] to prevent double-counting of individual contributions. Assuming the ellipsoidal anomaly to be of Dirichlet type, the resulting TS map is shown in Fig. 9(a), which clearly reflects the presence of fold- and cusp-type caustics. For completeness, Fig. 9(b) plots the corresponding diagram obtained via numerical integration of (3.3), while Fig. 9(c) compares the two estimates along an example ray II^{-}. As can be seen from the panel, the near-boundary, uniform, and non-uniform approximations smoothly transition into one another and overlap with the numerical solution.

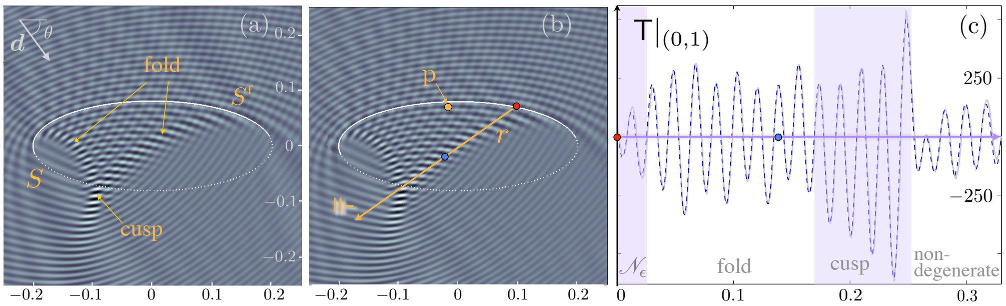

Figure 9. Distribution of $\mathsf{T}|_{(\mathsf{A},\mathsf{B})=(0,1)}$ in the Π-plane for a Dirichlet obstacle, $\boldsymbol{d} \,\|\, \Pi$, and $\theta = 0.35\pi$: (a) numerical integration, (b) high-frequency approximation, and (c) comparison along ray II^{-} (solid - numerics, dashed - asymptotics).

In the context of Remark 7, one may observe from Fig. 9 that obstacle illumination by a single incident wave yields no information about the "dark side" of the anomaly thanks to the fact that the scattered field vanishes (to the leading order) there, see (3.1). Recalling Corollary 5.3 in [22], on the other hand, it is further noted (using the length scale in Fig. 9) that D would have to be contained within a ball of radius $R_\circ \simeq 4.49/k \simeq 0.015$ [30] in order to guarantee the uniqueness of obstacle reconstruction with only a single incident plane wave.

(c) Partial and full source aperture

In what follows, the partial- and full-source-aperture simulations of TS are effected by first i) integrating (3.4) numerically to obtain (3.3) – as a function of $\boldsymbol{x}^\circ$ – for given $\boldsymbol{d}$, and then ii) integrating the latter result (also numerically) with respect to $\boldsymbol{d}$ over a prescribed subset of Ω. In the context of the single-incident-wave example in Fig. 9, it is first of interest to integrate $\mathsf{T}(\boldsymbol{x}^\circ)$ with respect to $\boldsymbol{d} \,\|\, \Pi$, i.e. with respect to the *in-plane* angle of incidence θ shown in Fig. 9(a). On denoting for brevity $\breve{\mathsf{T}}_\Pi = \int_\Pi \mathsf{T} \, \mathrm{d}\Omega_{\boldsymbol{d}}$, it can be shown by following the analysis in Section 4(b) that the contributions of $\mathsf{T}^\star$, T^c and $\mathsf{T}^{\mathrm{II}^{\pm}}$ to $\breve{\mathsf{T}}_\Pi$ behave respectively as $O(k)$, $O(k^\alpha)$ and $O(k^\mu)$, where $\alpha \leqslant 3/4$ and $\mu \leqslant 3/4$ due to the fact that the codimension of catastrophes in the example does not exceed two. Such reconstruction ability of $\breve{\mathsf{T}}_\Pi$ is illustrated in Fig. 10, which plots the evolution of TS with increasing *in-plane* aperture. Note that (i) the bright sector of the unit circle in each panel depicts the source aperture; (ii) the TS distributions are thresholded at 45%; (iii) the bottom right panel plots $\breve{\mathsf{T}}_\Pi$, and (iv) the full-source-aperture result assumes 80 equidistant plane-wave directions, which approximate the continuum of unit vectors $\boldsymbol{d}$ spanning the unit circle.

In practice, one may expect to obtain a satisfactory TS reconstruction – at least at lower frequencies – with only a limited number of incident plane waves, see e.g. [18, 31]. To examine this possibility, Fig. 11 plots four "coarse" approximations of $\breve{\mathsf{T}}_\Pi$, computed with $4 \leqslant N \leqslant 32$ incident

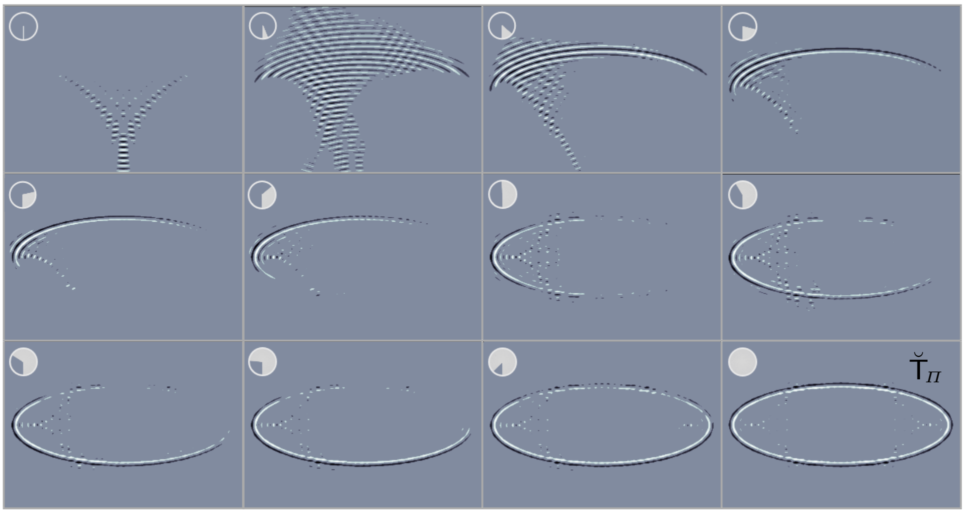

Figure 10. Imaging of a Dirichlet anomaly by $\mathsf{T}|_{(\mathsf{A},\mathsf{B})=(0,1)}$: evolution of TS with increasing (in-plane) source aperture.

wave directions (indicated on the unit circle) spanning $[0, 2\pi]$. As can be seen from the display, the high-frequency TS reconstruction is notably sensitive to the density of plane-wave illumination, primarily due to the apparent effect of *caustics*. This finding appears to be consistent with the high-frequency numerical study in [29] on the TS reconstruction of Neumann obstacles in $\mathbb{R}^2$, where 120 incident plane wave directions were deployed to obtain the reported full-aperture images.

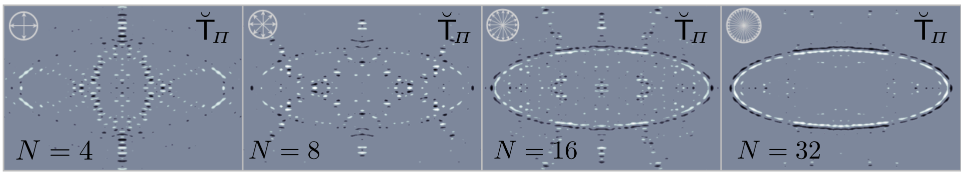

Figure 11. Effect of source density on the TS reconstruction of a Dirichlet anomaly with $(\mathsf{A},\mathsf{B}) = (0,1)$: "full" aperture images obtained with $4 \leqslant N \leqslant 32$ incident plane waves.

For completeness, the reconstruction of a Dirichlet obstacle by $\breve{\mathsf{T}}_{\Pi}|_{(\mathsf{A},\mathsf{B})=(0,1)}$ is compared in Fig. 12 to that of a Neumann anomaly by $\breve{\mathsf{T}}_{\Pi}|_{(\mathsf{A},\mathsf{B})=(3/2,-1)}$. Here the left, middle, and right panels plot respectively $\breve{\mathsf{T}}_{\Pi}$, thresholded $\breve{\mathsf{T}}_{\Pi}$, and example near-boundary variation of $\breve{\mathsf{T}}_{\Pi}$ (along the indicated normal) versus the contribution of $\mathsf{T}^{\star}$ only. Note that the featured images are obtained by adopting *Algorithm 1*, which samples each anomaly with physically-compatible vanishing obstacle. As can be seen from Fig. 12(e), this leads to an apparent "smearing" in the case of a Neumann obstacle. In contrast, its image obtained via *Algorithm 2*, i.e. using $\breve{\mathsf{T}}|_{(\mathsf{A},\mathsf{B})=(0,1)}$ as a sampling tool, is given by the negative of Fig. 12(b) – and thus better localized.

To provide the *full-source-aperture* counterpart of the result in Fig 12(c) – computed at boundary point $\boldsymbol{x}^{\star} = (0.178, 0.036, 0)$, Fig. 13 compares the analytical expression (4.25) with a numerical estimate of $\breve{\mathsf{T}} \equiv \breve{\mathsf{T}}_{\Omega}$, obtained by the superposition of $4\pi N^{-1} \times$(3.3) for N=512 incident plane-wave directions, uniformly distributed over Ω. For generality, the comparison is made at both in-plane boundary point $\boldsymbol{x}^{\star} = (0.178, 0.036, 0)$ (left panel), and its out-of-plane companion $\boldsymbol{x}^{\star} = (0.114, 0.046, 0.470)$ (right panel). Irrespective of the boundary point, the numerical result closely follows (4.25) at both $k = 300$ and $k = 600$, showing visibly better agreement in the latter case.

To conclude the study, *Algorithm 1* is applied to identify the boundary of a circular hole (Neumann obstacle) in an aluminum plate from the recent set of *elastodynamic* experiments [43]. In this case, elastic waves are propagated in a *bounded* domain shown in Fig. 14(a) and monitored along its top and side edges. The incident waves are generated by a piezoelectric transducer, placed sequentially at five locations indicated in the panel, such that the ratio between the wavelength and the obstacle size is 0.85. Thus, the testing configuration is incompatible with

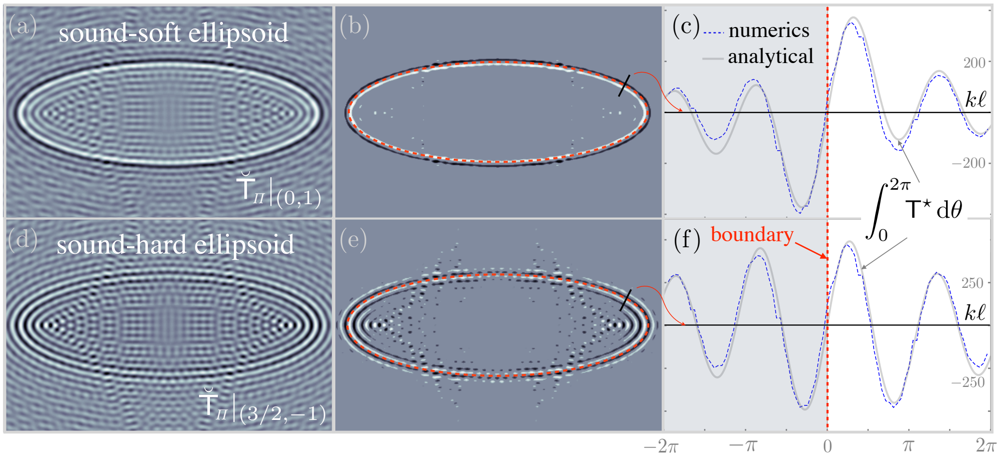

Figure 12. Distribution of $\breve{\mathsf{T}}_{\varPi}(\boldsymbol{x}^\circ)$ for a Dirichlet obstacle probed with $(\mathsf{A},\mathsf{B})=(0,1)$ (top row), and Neumann obstacle sampled with $(\mathsf{A},\mathsf{B})=(3/2,-1)$ (bottom row): full variation (left), thresholded distribution (middle), and example near-boundary variation (right). The thin dashed line in panels (b) and (e) traces $S \cap \varPi$.

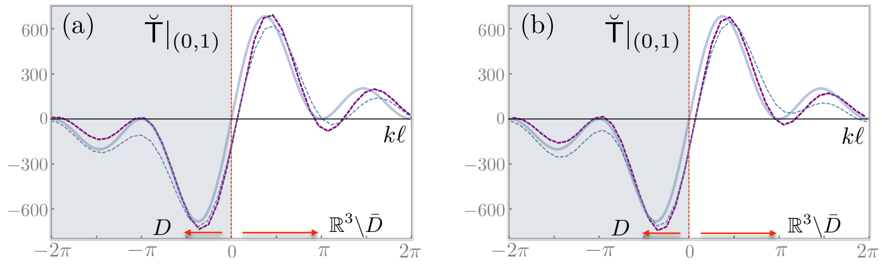

Figure 13. Near-boundary variation of $\breve{\mathsf{T}}|_{(0,1)}$ at $\boldsymbol{x}^\star=(0.178, 0.036, 0)$ (left) and $\boldsymbol{x}^\star=(0.114, 0.046, 0.470)$ (right): analytical solution (4.25) (solid line) versus the numerical result for $k=300$ (thin dashed line) and $k=600$ (thick dashed line). The hidden anomaly is sound-soft.

the present analysis in several aspects, including (i) dimensionality of the problem, (ii) type of the governing equation, (iii) geometry of the anomaly-free domain, (iv) probing wavelength, and (v) source aperture. Nonetheless the reconstruction of a circular hole in panel (c), obtained by applying *Algorithm 1* to the TS distribution [43] shown in panel (b), is rather satisfactory.

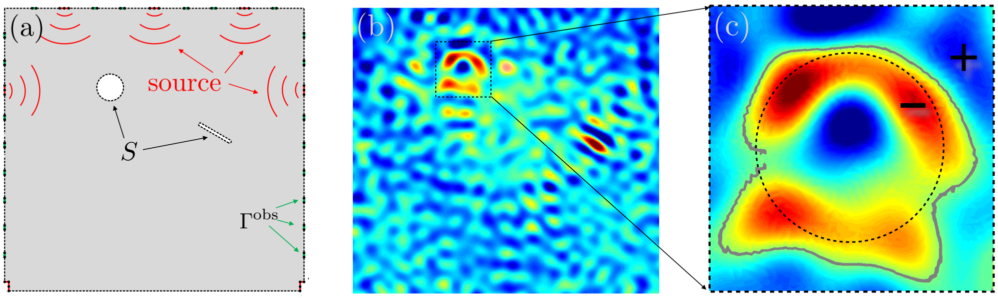

Figure 14. Elastodynamic experiment in [43]: (a) testing setup, (b) five-sources TS field, and (c) true boundary (dashed circle) versus its reconstruction (solid irregular line) obtained via Algorithm 1.

6. Summary

In this work, it is shown why the topological sensitivity (TS) may work as a non-iterative tool for the waveform tomography of finite-sized anomalies in the short wavelength regime. The analysis confirms previous numerical and experimental findings to this effect, that have so far eluded rigorous justification. To establish the claim, it is assumed that anomaly is convex and impenetrable, and that the sensory data are of the far-field type. Making use of the multipole expansion and Kirchhoff approximation, the TS indicator function is first expressed as a surface Fourier integral over the illuminated part of obstacle's boundary. Under the high-wavenumber hypothesis, the latter is pruned to three asymptotic essentials, namely i) the near-boundary approximation for sampling points within few wavelengths from the illuminated surface of an anomaly; ii) diffraction catastrophes (of codimension < 4) for sampling points near caustic surfaces, lines, and points; and iii) stationary phase approximation in the remainder of the sampled region. In the case of the full source aperture, it is shown via catastrophe theory that the TS is asymptotically dominated by the explicit near-boundary term. This unveils the new reconstruction logic at short wavelengths, where the anomaly's boundary is obtained as a zero level set of the TS field separating its extreme negative and extreme positive values while its character – if unknown beforehand – is exposed from the sign of the near-boundary variation. The analysis inherently lends itself to the treatment of diffraction catastrophes with higher codimension ($\geqslant 4$) for which uniform approximation may become available. However, extensions of the study to penetrable, non-convex, or multiple scatterers remain open question due to lack of explicit (Kirchhoff-type) approximations for the scattered field on the boundary of such obstacles.

Acknowledgment

The support provided by the U.S. Department of Energy via NEUP Grant #10-862 and the University of Minnesota Supercomputing institute is kindly acknowledged. Special thanks are due to Sir Michael Berry and David Farrelly for their input during the course of this investigation.

References

1 H. Ammari, E. Bretin, J. Garnier, W. Jing, H. Kang, and A. Wahab. Localization, stability, and resolution of topological derivative based imaging functionals in elasticity. *SIAM J. Imag. Sci.*, 6:2174–2212, 2013.

2 H. Ammari, P. Garapon, L. Guadarrama Bustos, and H. Kang. Transient anomaly imaging by the acoustic radiation force. *J. Diff. Eqs.*, 249:1579–1595, 2010.

3 H. Ammari, J. Garnier, W. Jing, H. Kang, M. Lim, K. Sølna, and H. Wang. *Mathematical and Statistical Methods for Multistatic Imaging*. Lect. Not. Math., 2098. Springer, 2013.

4 H. Ammari, J. Garnier, V. Jugnon, and H. Kang. Direct reconstruction methods in ultrasound imaging of small anomalies. In *Mathematical Modeling in Biomedical Imaging II*, Lect. Not. Math., 2035, 31–55. Springer, 2012.

5 H. Ammari, J. Garnier, V. Jugnon, and H. Kang. Stability and resolution analysis for a topological derivative based imaging functional. *SIAM J. Contr. Opt.*, 50:48–76, 2012.

6 H. Ammari, J. Garnier, H. Kang, M. Lim, and K. Sølna. Multistatic imaging of extended targets. *SIAM J. Imag. Sci.*, 5:564–600, 2012.

7 H. Ammari, E. Iakovleva, and S. Moskow. Recovery of small inhomogeneities from the scattering amplitude at a fixed frequency. *SIAM J. Math. Anal.*, 34:882–900, 2003.

8 H. Ammari and H. Kang. *Reconstruction of the Small Inhomogeneities from Boundary Measurements*. Springer, New York, 2004.

9 C. Bellis and M. Bonnet. A FEM-based topological sensitivity approach for fast qualitattive identification of buried cavities from elastodynamic overdetermined boundary data. *Int. J. Solids Struct.*, 47:1221–1242, 2010.

10 C. Bellis, M. Bonnet, and F. Cakoni. Acoustic inverse scattering using topological derivative of far-field measurements-based L^2 cost functionals. *Inverse Problems*, 29:075012, 2013.

11 M. V. Berry and C. Upstill. Catastrophe optics: Morphologies of caustics and their diffraction patterns. *Progress in Optics*, 18:257–346, 1980.

12 N. Bleistein. *Mathematical Methods for Wave Phenomena*. Academic Press, London, 1984.

13 N. Bleistein, J.K. Cohen, and J.W. Stockwell, Jr. *Mathematics of Multidimensional Seismic Imaging, Migration, and Inversion*. Springer, New York, 2001.

14 M. Bonnet. Inverse acoustic scattering by small-obstacle expansion of a misfit function. *Inverse Problems*, 24:035022, 2008.

15 M. Bonnet and B. B. Guzina. Topological derivative for the inverse scattering of elastic waves. *Int. J. Num. Meth. Eng.*, 57:161–179, 2004.

16 V. A. Borovikov. *Uniform Stationary Phase Method*. Instit. Electrical Engineers, London, 1994.

17 J.J. Bowman, T.B. Senior, and P.L. Uslenghi. *Electromagnetic and Acoustic Scattering by Simple Shapes*. Hemisphere Publ. Corp., New York, 1987.

18 A. Carpio, B.T. Johansson, and M.-L. Rapún. Determining planar multiple sound-soft obstacles from scattered acoustic fields. *J. Math. Imaging Vis.*, 36:185–199, 2010.

19 A. Carpio and M. L. Rapun. Topological derivatives for shape reconstruction. *Lect. Not. Math.*, 1943:85–131, 2008.

20 I. Chikichev and B. B. Guzina. Generalized topological derivative for the Navier equation and inverse scattering in the time domain. *Comp. Meth. Appl. Mech. Eng.*, 197:4467–4484, 2008.

21 D. Colton, J. Coyle, and P. Monk. Recent developments in inverse acoustic scattering theory. *SIAM Review*, 42:369–414, 2000.

22 D. Colton and R. Kress. *Inverse Acoustic and Electromagnetic Scattering Theory*. Springer, New York, 2013.

23 Michel Demazure. *Bifurcations and Catastophes*. Springer, Berlin, 2000.

24 A.J. Devaney. *Mathematical Foundations of Imaging, Tomography and Wavefield Inversion*. Cambridge Univ. Press, Cambridge, UK, 2012.

25 NIST Digital Library of Mathematical Functions. http://dlmf.nist.gov, Release 1.0.6 (05-06-13).

26 N. Dominguez and V. Gibiat. Non-destructive imaging using the time domain topological energy method. *Ultrasonics*, 50:367–372, 2010.

27 N. Dominguez, V. Gibiat, and Y. Esquerre. Time domain topological gradient and time reversal analogy: an inverse method for ultrasonic target detection. *Wave Motion*, 42:31–52, 2005.

28 A. Erdelyi, editor. *Bateman Manuscript Project, Tables of Integral Transforms Volume II*. McGraw-Hill, New York, 1954.

29 G. R. Feijoo. A new method in inverse scattering based on the topological derivative. *Inverse Problems*, 20:1819–1840, 2004.

30 D. Gintides. Local uniqueness for the inverse scattering problem in acoustics via the Faber–Krahn inequality. *Inverse Problems*, 21:1195, 2005.

31 B. Guzina and M. Bonnet. Small-inclusion asymptotic of misfit functionals for inverse problems in acoustics. *Inverse Problems*, 22:1761–1785, 2006.

32 B. B. Guzina and M. Bonnet. Topological derivative for the inverse scattering of elastic waves. *Quart. J. Mech. Appl. Math.*, 57:161–179, 2004.

33 B. B. Guzina and M. Bonnet. Small-inclusion asymptotic of misfit functionals for inverse problems in acoustics. *Inverse Problems*, 22:1761–1785, 2006.

34 A. Kirsch and N. Grinberg. *The Factorization Method for Inverse Problems*. Oxford University Press, Oxford, UK, 2007.

35 M. Masmoudi, J. Pommier, and B. Samet. The topological asymptotic expansion for the Maxwell equations and some applications. *Inverse Problems*, 21:547–564, 2005.

36 W-K. Park. Topological derivative strategy for one-step iteration imaging of arbitrary shaped thin, curve-like electromagnetic inclusions. *J. Comp. Phys.*, 231:1426–1439, 2012.

37 T. Poston and I. Stewart. *Catastrophe Theory and its Applications*. Pitman, London, 1981.

38 B. Samet, S. Amstutz, and M. Masmoudi. The topological asymptotic for the Helmholtz equation. *SIAM J. Contr. Optim.*, 42:1523–1544, 2003.

39 J. Sokolowski and A. Zochowski. On the topological derivative in shape optimization. *SIAM J. Control Optim.*, 37:1251–1272, 1999.

40 J. J. Stamnes. *Waves in Focal Regions*. Taylor & Francis, New York, 1986.

41 I. Stewart. Catastrophe theory in physics. *Rep. Prog. Phys.*, 45:185–221, 1982.

42 R. Thom. *Stabilité Structurelle et Morphogénèse*. Benjamin, New York, 1972.

43 R.D. Tokmashev, A. Tixier, and B.B. Guzina. Experimental validation of the topological sensitivity approach to elastic-wave imaging. *Inverse Problems*, 29:125005, 2013.

44 J Virieux and S Operto. An overview of full-waveform inversion in exploration geophysics. *Geophysics*, 74:WCC1–WCC26, 2009.

45 E. C. Zeeman. The geomery of catastrophe. *Times Literary Supplement*, Dec. 10:1556–7, 1971.

A. Hessian of the phase function

(a) Determinant of the Hessian matrix

At the stationary points of $\boldsymbol{\zeta}\cdot\boldsymbol{d}\pm r$, one finds via (3.11) and (3.9) its Hessian to read

$$A_{pq}(\boldsymbol{\zeta}) \;=\; \pm\frac{1}{r}\left[\frac{\partial\boldsymbol{\zeta}}{\partial\eta^p}\cdot\frac{\partial\boldsymbol{\zeta}}{\partial\eta^q}-\Big(\boldsymbol{d}\cdot\frac{\partial\boldsymbol{\zeta}}{\partial\eta^p}\Big)\Big(\boldsymbol{d}\cdot\frac{\partial\boldsymbol{\zeta}}{\partial\eta^q}\Big)\right] + \begin{cases} 0, & \boldsymbol{\zeta}=\boldsymbol{\zeta}_{\mathrm{I}}^{\pm} \\ -2|\boldsymbol{d}\cdot\boldsymbol{n}|\,\boldsymbol{n}\cdot\frac{\partial^2\boldsymbol{\zeta}}{\partial\eta^p\partial\eta^q}, & \boldsymbol{\zeta}=\boldsymbol{\zeta}_{\mathrm{II}}^{\pm}\end{cases}, \qquad \text{(A 1)}$$

where $r=|\boldsymbol{\zeta}-\boldsymbol{x}^{\mathrm{o}}|>0$. On selecting the curvilinear coordinates (η^1,η^2) so that their tangents coincide with the *principal directions* $\boldsymbol{a}_p$ $(p{=}1,2)$ of S^{f} at the stationary point, (A 1) reduces to

$$A_{pq}(\boldsymbol{\zeta}) \;=\; \pm\frac{1}{r}\Big[g_{pq}-\sqrt{g_{pp}g_{qq}}\,(\boldsymbol{d}\cdot\boldsymbol{a}_p)\,(\boldsymbol{d}\cdot\boldsymbol{a}_q)\Big] + \begin{cases} 0, & \boldsymbol{\zeta}=\boldsymbol{\zeta}_{\mathrm{I}}^{\pm} \\ 2|\boldsymbol{d}\cdot\boldsymbol{n}|\,\frac{g_{pq}}{\rho_p}, & \boldsymbol{\zeta}=\boldsymbol{\zeta}_{\mathrm{II}}^{\pm}\end{cases} \quad \text{(no sum)}, \qquad \text{(A 2)}$$

where $\boldsymbol{n}$ is the unit outward normal on S^{f}; $\rho_1\geqslant\rho_2>0$ denote the principal radii of curvature of S^{f}; g_{pq} are the components of the (diagonal) first fundamental form, and b_{pq} stand for the second fundamental form. From (A 2) and the first of (3.13), one finds that

$$\det(A_{pq}) \;=\; \det g_{pq}\,\frac{(\boldsymbol{d}\cdot\boldsymbol{n})^2}{r^2}>0, \qquad \operatorname{sgn}(A_{pq})=\pm 2, \qquad \boldsymbol{\zeta}=\boldsymbol{\zeta}_{\mathrm{I}}^{\pm}, \quad \boldsymbol{x}^{\mathrm{o}}\in\mathrm{I}^{\pm}, \qquad \text{(A 3)}$$

where the signature of the Hessian matrix, $\operatorname{sgn}(A_{pq})$, equals the difference between the number of positive and negative eigenvalues of A_{pq}. The strict positivity of $\det(A_{pq})$ in (A 3) demonstrates that the stationary-phase approximation (3.8) is valid for all sampling points $\boldsymbol{x}^{\mathrm{o}}\notin\mathscr{N}_\epsilon$ along the $\mathrm{I}^{\pm}$ loci. The situation along the $\mathrm{II}^{\pm}$ loci is, however, more complicated since

$$\det(A_{pq}) \;=\; \frac{4(\boldsymbol{d}\cdot\boldsymbol{n})^2}{\rho_1\rho_2\,r^2}\,\det g_{pq}\prod_{j=1}^{2}(r\pm r_j)\gtreqless 0, \qquad \operatorname{sgn}(A_{pq})\in\{-2,0,2\}, \qquad \boldsymbol{\zeta}=\boldsymbol{\zeta}_{\mathrm{II}}^{\pm}, \quad \boldsymbol{x}^{\mathrm{o}}\in\mathrm{II}^{\pm}, \qquad \text{(A 4)}$$

where

$$r_{1/2} \;=\; \frac{1}{4|\boldsymbol{d}\cdot\boldsymbol{n}|}\Big[h\pm\sqrt{h^2-4(\boldsymbol{d}\cdot\boldsymbol{n})^2\rho_1\rho_2}\Big], \qquad h \;=\; \rho_1(1-(\boldsymbol{d}\cdot\boldsymbol{a}_1)^2)+\rho_2(1-(\boldsymbol{d}\cdot\boldsymbol{a}_2)^2). \qquad \text{(A 5)}$$

Assuming $\boldsymbol{x}^{\mathrm{o}}\notin\mathscr{N}_\epsilon$, (A 3) and (A 4) demonstrate that the stationary-phase approximation (3.8) holds for all sampling points along ray II^+, and those along ray II^- whose distance to the stationary point, $r{=}|\boldsymbol{x}^{\mathrm{o}}-\boldsymbol{\zeta}^-|$, is sufficiently separated from the caustic values (A 5).

(b) Nature of the roots r_1 and r_2

In light of the facts that $0{<}\rho_2\leqslant\rho_1$ and $(\boldsymbol{d}\cdot\boldsymbol{n})^2{=}1-(\boldsymbol{d}\cdot\boldsymbol{a}_1)^2-(\boldsymbol{d}\cdot\boldsymbol{a}_2)^2$, one finds that the discriminant in (A 5) is, for any given triplet $\{\rho_1,\rho_2,\boldsymbol{d}\cdot\boldsymbol{a}_1\}$, a monotonically decreasing function of $(\boldsymbol{d}\cdot\boldsymbol{n})^2$. Accordingly, the latter is (given $\boldsymbol{d}\cdot\boldsymbol{a}_1$) minimized by setting $\boldsymbol{d}\cdot\boldsymbol{a}_2{=}0$, in which case

$$h^2-4(\boldsymbol{d}\cdot\boldsymbol{n})^2\rho_1\rho_2 \;=\; \big(\rho_1(\boldsymbol{d}\cdot\boldsymbol{n})^2-\rho_2\big)^2\begin{cases} =0, & \boldsymbol{d}\cdot\boldsymbol{a}_2{=}0 \;\text{ and }\; |\boldsymbol{d}\cdot\boldsymbol{n}|^2{=}\,\rho_2/\rho_1 \\ >0, & \text{otherwise}\end{cases}. \qquad \text{(A 6)}$$

As a result, the roots r_1 and r_2 are real-valued, positive, and distinct unless $\boldsymbol{d}\cdot\boldsymbol{a}_2=0$ and $|\boldsymbol{d}\cdot\boldsymbol{n}|^2{=}\,\rho_2/\rho_1$ (in which case $r_1{=}r_2{=}\sqrt{\rho_1\rho_2}/2$). From (A 5), it is also seen that for fixed $\{\rho_1,\rho_2,\boldsymbol{d}\cdot\boldsymbol{n}\}$, h is a monotonically decreasing function of $(\boldsymbol{d}\cdot\boldsymbol{a}_1)^2$. Accordingly the lower (r_j^{ℓ}) and upper (r_j^{u}) bounds on $r_{1/2}$ can be obtained from (A 5) by setting $(\boldsymbol{d}\cdot\boldsymbol{a}_1)^2$ to either zero or $1-(\boldsymbol{d}\cdot\boldsymbol{n})^2$; in particular, one finds that

$$\begin{aligned} r_2^{\ell} &= \frac{\rho_2}{2}|\boldsymbol{d}\cdot\boldsymbol{n}| \\ r_1^{u} &= \frac{\rho_1}{2|\boldsymbol{d}\cdot\boldsymbol{n}|}\end{aligned}, \quad r_2^{u} \;=\; \begin{cases}\frac{\rho_1}{2}|\boldsymbol{d}\cdot\boldsymbol{n}|, & |\boldsymbol{d}\cdot\boldsymbol{n}|\leqslant\sqrt{\frac{\rho_2}{\rho_1}} \\ \frac{\rho_2}{2|\boldsymbol{d}\cdot\boldsymbol{n}|}, & \text{otherwise}\end{cases}, \quad r_1^{\ell} \;=\; \begin{cases}\frac{\rho_2}{2|\boldsymbol{d}\cdot\boldsymbol{n}|}, & |\boldsymbol{d}\cdot\boldsymbol{n}|\leqslant\sqrt{\frac{\rho_2}{\rho_1}} \\ \frac{\rho_1}{2}|\boldsymbol{d}\cdot\boldsymbol{n}| & \text{otherwise}\end{cases}, \qquad \text{(A 7)}$$

where r_1^ℓ is obtained by substituting the upper bound on r_2 into identity $r_1 r_2 = \rho_1 \rho_2/4$. The above result is illustrated in Fig. 15 via the polar plots of $r_2^\ell, r_2^u, r_1^\ell$ and r_1^u for the example ratio $\rho_2/\rho_1 = 0.7$. For completeness it can be also shown that, consistent with Fig. 15,

$$\lim_{|\boldsymbol{d}\cdot\boldsymbol{n}|\to 0} r_1 = \frac{\rho_1 - (\rho_1-\rho_2)(\boldsymbol{d}\cdot\boldsymbol{a}_1)^2}{2|\boldsymbol{d}\cdot\boldsymbol{n}|}, \qquad \lim_{|\boldsymbol{d}\cdot\boldsymbol{n}|\to 0} r_2 = \frac{\tfrac{1}{2}\rho_1\rho_2\,|\boldsymbol{d}\cdot\boldsymbol{n}|}{\rho_1 - (\rho_1-\rho_2)(\boldsymbol{d}\cdot\boldsymbol{a}_1)^2}, \qquad \lim_{|\boldsymbol{d}\cdot\boldsymbol{n}|\to 1} r_k = \frac{\rho_k}{2}.$$

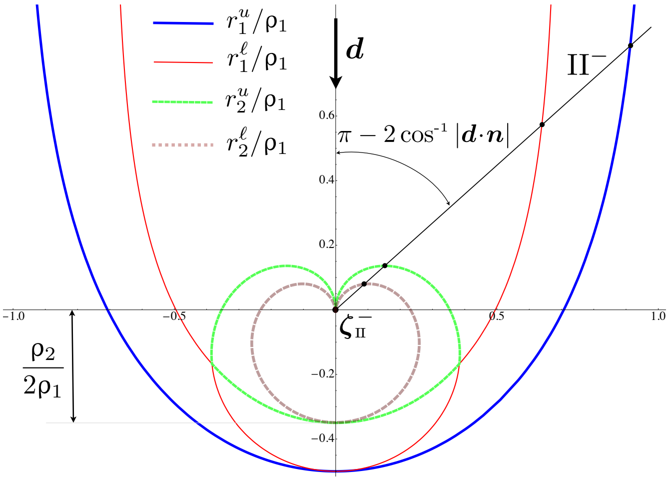

Figure 15. Upper and lower bounds on the caustic distances r_1 and r_2 along ray II$^-$, computed for $\rho_2/\rho_1 = 0.7$.

(c) Behavior of the Hessian for near-caustic sampling points

For the purposes of this study, it is instructive to examine the limiting behavior of (A 2) for sampling points $\boldsymbol{x}^\circ \in \mathrm{II}^-$ such that $r = |\boldsymbol{x}^\circ - \boldsymbol{\zeta}_{\mathrm{II}}^-| = r_k + \epsilon$, $\epsilon \to 0$.

Case $\boldsymbol{d}\cdot\boldsymbol{a}_1 = 0$ ($\boldsymbol{\zeta} = \boldsymbol{\zeta}_{\mathrm{II}}^-$). For this configuration, one finds from (A 2) and (A 5) that the mixed derivative vanishes at the stationary point (i.e. $A_{12} = A_{21} = 0$) for any $r > 0$, while

$$\begin{aligned} &A_{11} \overset{\epsilon^2}{=} g_{11}\frac{4|\boldsymbol{d}\cdot\boldsymbol{n}|^2}{\rho_1^2}\,\epsilon, && A_{22} \overset{\epsilon}{=} 2g_{22}\left(\frac{|\boldsymbol{d}\cdot\boldsymbol{n}|}{\rho_2} - \frac{|\boldsymbol{d}\cdot\boldsymbol{n}|^3}{\rho_1}\right), && r = r_1 + \epsilon, \\ &A_{22} \overset{\epsilon^2}{=} \frac{4g_{22}}{\rho_2^2}\,\epsilon, && A_{11} \overset{\epsilon}{=} \frac{2g_{11}}{|\boldsymbol{d}\cdot\boldsymbol{n}|}\left(\frac{|\boldsymbol{d}\cdot\boldsymbol{n}|^2}{\rho_1} - \frac{1}{\rho_2}\right), && r = r_2 + \epsilon, \end{aligned} \tag{A 8}$$

when $\epsilon \to 0$. From (A 8) it is clear that the corank of the Hessian matrix (A 2) equals *one* in the limit as $r \to r_{1/2}$, except when $|\boldsymbol{d}\cdot\boldsymbol{n}|^2 = \rho_2/\rho_1 = 1$.

Case $\boldsymbol{d}\cdot\boldsymbol{a}_2 = 0$ ($\boldsymbol{\zeta} = \boldsymbol{\zeta}_{\mathrm{II}}^-$). In this situation, one again finds that $A_{12} = A_{21} = 0$ for any $r > 0$. On the other hand, it follows from (A 2) and (A 5) that

$$\begin{aligned} &A_{11} \overset{\epsilon^2}{=} \frac{4g_{11}}{\rho_1^2}\epsilon, && A_{22} \overset{\epsilon}{=} \frac{2g_{22}}{|\boldsymbol{d}\cdot\boldsymbol{n}|}\left(\frac{|\boldsymbol{d}\cdot\boldsymbol{n}|^2}{\rho_2} - \frac{1}{\rho_1}\right), && \begin{cases} r = r_1 + \epsilon, & \frac{\rho_2}{\rho_1} < |\boldsymbol{d}\cdot\boldsymbol{n}|^2 \\ r = r_2 + \epsilon, & \frac{\rho_2}{\rho_1} \geqslant |\boldsymbol{d}\cdot\boldsymbol{n}|^2 \end{cases} \\ &A_{22} \overset{\epsilon^2}{=} \frac{4g_{22}|\boldsymbol{d}\cdot\boldsymbol{n}|^2}{\rho_2^2}\epsilon, && A_{11} \overset{\epsilon}{=} 2g_{11}\left(\frac{|\boldsymbol{d}\cdot\boldsymbol{n}|}{\rho_1} - \frac{|\boldsymbol{d}\cdot\boldsymbol{n}|^3}{\rho_2}\right), && \begin{cases} r = r_1 + \epsilon, & \frac{\rho_2}{\rho_1} \geqslant |\boldsymbol{d}\cdot\boldsymbol{n}|^2 \\ r = r_2 + \epsilon, & \frac{\rho_2}{\rho_1} < |\boldsymbol{d}\cdot\boldsymbol{n}|^2 \end{cases} \end{aligned} \tag{A 9}$$

when $\epsilon \to 0$. For sampling points $\boldsymbol{x}^\circ$ along ray II$^-$, (A 9) accordingly demonstrates that the corank of (A 2) equals one in the limit as $r \to r_{1/2}$, except when $|\boldsymbol{d}\cdot\boldsymbol{n}|^2 = \rho_2/\rho_1$.

Case $(\boldsymbol{d}\cdot\boldsymbol{a}_1)(\boldsymbol{d}\cdot\boldsymbol{a}_2)\neq 0$ ($\boldsymbol{\zeta}{=}\boldsymbol{\zeta}_{\text{II}}^-$). For this class of configurations, $r_1\neq r_2$ due to (A 5) and (A 6). As a result the corank of the Hessian matrix (A 2) at $\boldsymbol{\zeta}{=}\boldsymbol{\zeta}_{\text{II}}^-$ equals one, regardless of $\boldsymbol{d}\cdot\boldsymbol{n}$, as $r\to r_{1/2}$. Next, assume $r=r_j+\epsilon$ where $\epsilon\to 0$ and $j{=}1,2$. Thanks to the Splitting Lemma [P1], for each j there exists a local diffeomorphism $(\eta^1,\eta^2)\to(\vartheta^1,\vartheta^2)$ under which the phase function (3.20) is approximated by the second of (3.23). In this case one has $A_{\vartheta^1\vartheta^2}=A_{\vartheta^2\vartheta^1}=0$ and, owing to the invariance of (A 4) with respect to the choice of local coordinates,

$$A_{\vartheta^1\vartheta^1}=O(1),\qquad A_{\vartheta^2\vartheta^2}=O(\epsilon),\qquad r=r_j+\epsilon,\qquad \epsilon\to 0. \tag{A 10}$$

Note that (A 8)–(A 10) apply to catastrophes of *any codimension*. Along given ray II^- the codimension of the caustic as $r\to r_j$, if exceeding one, is inherently governed by the limiting behavior of higher-order derivatives of $\boldsymbol{\zeta}\cdot\boldsymbol{d}-r$, i.e. the derivatives of A_{pq}, in that neighborhood.

References

P1 T. Poston and I. Stewart. *Catastrophe Theory and its Applications*. Pitman, London, 1981.

B. Asymptotic expansion in the caustic region

For completeness, this section summarizes the asymptotic evaluation of a two-dimensional Fourier integral (3.7) in situations when the phase function $\phi = \boldsymbol{\zeta}\cdot\boldsymbol{d} - r$ is affiliated with any of the diffraction catastrophes listed in Table 2. The analysis implicitly makes use of the Van der Corput neutralizers [Q3, Q4] that are described at the end of the section.

(a) Hessian matrix of corank one

With the caveat of two degenerate configurations discussed in Appendix A(c), the corank of the Hessian of (3.20) within the bifurcation set (3.21) equals *one* which allows for the separation of ϕ into a non-degenerate Morse piece and a single-argument degenerate part according to the second of (3.23). In this setting (3.7) can be first integrated along the non-degenerate direction ϑ^1, thereby allowing the contribution of nearby (or coalescing) stationary points to be investigated in the context of a one-dimensional integral

$$k^{-\frac{1}{2}}\int_{-\infty}^{\infty}\mathscr{F}(\vartheta)\,e^{\mathrm{i}k\psi(\vartheta)}\,\mathrm{d}\vartheta, \qquad \vartheta=\vartheta^2, \qquad \psi(\vartheta)=(\boldsymbol{\zeta}\cdot\boldsymbol{d}-r)|_{\vartheta^1=0}, \qquad \text{(B 1)}$$

where

$$\mathscr{F}(\vartheta) \;=\; \frac{\sqrt{2\pi}\,e^{\mathrm{i}\delta\pi/4}\,f(\boldsymbol{\zeta})|_{\vartheta^1=0}}{\sqrt{|\partial^2\phi/\partial(\vartheta^1)^2|_{\vartheta^1=0}}} \times \frac{\mathrm{d}S_\eta}{\mathrm{d}S_\vartheta}\bigg|_{\vartheta^1=0}, \qquad \delta \;=\; \mathrm{sign}\left(\frac{\partial^2\phi}{\partial(\vartheta^1)^2}\right)\bigg|_{\vartheta^1=0}. \qquad \text{(B 2)}$$

Following Table 2, the codimension of the phase function is assumed not to exceed three, which in the context of (B 1) allows for structurally-stable caustics that are of either type *fold*, *cusp* or *swallowtail* [Q2] depending on the geometry of S^{f} in the neighborhood of $\boldsymbol{\zeta}_{\mathrm{II}}^{-}$.

One particular phenomenon that is common to all caustics, as elucidated by the catastrophe theory, is a dramatic shift in the character of the phase function due to smooth variation of its parameters. This may be interpreted as the suppression of propagating waves across the caustic: on the so-called *bright side* [Q13] of the bifurcation set B_ϕ, the diffraction pattern is formed by propagating waves stemming from the interaction of real-valued stationary points; however as $\boldsymbol{x}^{\mathrm{o}}$ moves across B_ϕ into the *dark side* of the caustic, at least one pair of the interacting stationary points become complex conjugate, leading to a diffraction pattern that is formed (at least in part) by evanescent waves. Due to the fact that the ensuing asymptotic models apply uniformly throughout the neighborhood of B_ϕ (and beyond), however, the remainder of this section makes little distinction between its bright and dark regions.

The procedure for developing *uniform* asymptotic approximation for a given type of diffraction catastrophe was first proposed in [Q7], and entails the following three steps. First, the degeneracy of the phase function is categorized, in terms of the topology of its stationary points, as a particular type of universal unfolding according to Thom's classification theorem. Second, a diffeomorphism is specified that maps the given phase function into a *normal form* representing the featured class of caustics. In particular, parameters of the so-called (minimal) *control space*, given by the coefficients of the normal form, are computed by solving a set of nonlinear equations. Third, depending upon the type of the caustic, a suitable expansion of the non-exponential part of the integrand is introduced – by which one arrives at the sought asymptotic approximation of an oscillatory integral. Here one should note that in the immediate vicinity of the bifurcation set B_ϕ (where stationary points coalesce), the uniform approximation breaks down. In this case the required mapping is computed stably, albeit locally, via Taylor series expansion of both the phase function and sought diffeomorphism, leading to the so-called *transitional* asymptotic approximation. A comprehensive asymptotic analysis of the fold and cusp diffraction catastrophes (both in terms of uniform and transitional approximations) can be found in [Q13], while the uniform asymptotic approximation of the swallowtail catastrophe is obtained in [Q10]. To facilitate the main presentation, the remainder of this section summarizes the uniform asymptotic treatment of the fold, cusp, and swallowtail catastrophes. Their transitional counterparts retain the same functional form, except that the germane control parameters and coefficients of approximation are computed locally.

Fold catastrophe. This type of caustics is affiliated with two coalescing stationary points that, on the dark side B_ϕ, become complex conjugate. The local behavior of the phase function around the "halfway" inflection point $\psi^{(2)}(0)=0$ follows, up to a diffeomorphism, the fold *normal form* $t^3/3+ct$. Following the aforementioned procedure, uniform asymptotic approximation of the one-dimensional integral (B 1) due to fold-type degeneracy of the phase function can be computed as

$$k^{-1/2}\int_{-\infty}^{\infty}\mathscr{F}(\vartheta)\,e^{\mathrm{i}k\psi(\vartheta)}\,\mathrm{d}\vartheta \;=\; e^{\mathrm{i}k\psi_\circ}\Big[k^{-5/6}f_1\,Ai(-ck^{\frac{2}{3}}) \,+\, k^{-7/6}f_2\,Ai'(-ck^{\frac{2}{3}})\Big] \,+\, O(k^{-3/2}), \tag{B 3}$$

in terms of the Airy function and its derivative

$$Ai(b) \;=\; \frac{1}{2\pi}\int_{-\infty}^{\infty} e^{\mathrm{i}(\tau^3/3\,+\,b\,\tau)}\,\mathrm{d}\tau, \qquad Ai' \;=\; \frac{\mathrm{d}Ai}{\mathrm{d}b}, \tag{B 4}$$

see e.g. [Q4]. Through a diffeomorphism $\vartheta\to t=k^{-1/3}\tau$ transforming $\psi(\vartheta)$ into $t^3/3+ct+\psi_\circ$, the control parameter c and phase offset can be computed explicitly as

$$c \;=\; \big[\tfrac{3}{4}\,(\psi(\vartheta_2)-\psi(\vartheta_1))\big]^{2/3}, \qquad \psi_\circ \;=\; \tfrac{1}{2}\big[\psi(\vartheta_1)+\psi(\vartheta_2)\big],$$

where ϑ_1 and ϑ_2 are the adjacent stationary points of $\psi(\vartheta)$, arranged so that $\psi(\vartheta_2)>\psi(\vartheta_1)$. The remaining quantities in (B 3) are the coefficients of the expansion given by

$$f_1 \;=\; \pi\,g^+ \quad f_2 \;=\; -\frac{\mathrm{i}\pi}{\sqrt{c}}\,g^-, \quad g^\pm \;=\; \mathscr{F}(\vartheta_1)\big[2\sqrt{c}/\psi^{(2)}(\vartheta_1)\big]^{1/2} \pm \mathscr{F}(\vartheta_2)\big[-2\sqrt{c}/\psi^{(2)}(\vartheta_2)\big]^{1/2}.$$

As ϑ_1 and ϑ_2 move apart, uniform approximation (B 3) reduces to the sum of the contributions of two isolated stationary points. It is also worth mentioning that the featured asymptotic model remains valid on the dark side of B_ϕ provided that c is replaced by $|c|e^{\mathrm{i}\pi}$, where $|c|=(\frac{3}{4}\,\mathrm{Im}[\psi(\vartheta_1)-\psi(\vartheta_2)])^{2/3}$. Further details on (B 3), along with a full account of the transitional approximation, can be found in [Q13].

Cusp catastrophe. In diffraction terms, this type of degeneracy occurs at the point contact of two fold caustics, and is characterized by three coalescing stationary points as the sampling point $\boldsymbol{x}^\circ$ approaches B_ϕ from the bright side. Specifically, the cusp catastrophe is the universal unfolding of *germ* t^4 with codimension two and normal form $t^4+c_2\,t^2+c_1\,t$. Assuming $\psi^{(3)}(0)=0$ and $\psi^{(4)}(0)>0$, uniform asymptotic approximation of (B 1) in the cusp region is given by

$$k^{-1/2}\int_{-\infty}^{\infty}\mathscr{F}(\vartheta)\,e^{\mathrm{i}k\psi(\vartheta)}\,\mathrm{d}\vartheta \;=\; e^{\mathrm{i}k\psi_\circ}\sum_{m=0}^{2} k^{-(3+m)/4}\,f_m\,P_{,m}(c_1k^{\frac{3}{4}},c_2k^{\frac{1}{2}}) \,+\, O(k^{-3/2}), \tag{B 5}$$

in terms of the Pearcey function and its derivatives

$$P(b_1,b_2) \;=\; \int_{-\infty}^{\infty} e^{\mathrm{i}(\tau^4\,+\,b_2\tau^2\,+\,b_1\tau)}\,\mathrm{d}\tau, \qquad P_{,0} \;=\; P, \qquad P_{,m} \;=\; \frac{1}{\mathrm{i}}\,\frac{\partial P}{\partial b_m} \;\; (m{=}1,2),$$

see for instance [Q13]. Through an implicit diffeomorphism $\vartheta\to t=k^{-1/4}\tau$, the phase function $\psi(\vartheta)$ is mapped onto $t^4+c_2\,t^2+c_1\,t+\psi_\circ$. Accordingly, the control parameters (c_1,c_2) and phase offset $\psi_\circ$ featured in (B 5) can be computed by solving the set of nonlinear equations enforcing one-to-one correspondence between the stationary points in the ϑ and t spaces, namely

$$\psi_\circ+c_1\,t_m+c_2\,t_m^2+t_m^4 \;=\; \psi(\vartheta_m), \qquad m=1,2,3$$

where the stationary points of $\psi(\vartheta)$ are denoted by ϑ_m, and their counterparts in the t-space are t_m which satisfy $4\,t_m^3+2\,c_2t_m+c_1=0$. The coefficients f_m of the uniform expansion (B 5) are obtained by solving

$$f_0 + f_1 t_m + f_2 t_m^2 = \mathscr{F}(\vartheta_m)\left.\frac{\mathrm{d}\vartheta}{\mathrm{d}t}\right|_{t=t_m}, \qquad \left.\frac{\mathrm{d}\vartheta}{\mathrm{d}t}\right|_{t=t_m} = \left[\frac{12\,t_m^2 + 2\,c_2}{\psi^{(2)}(\vartheta_m)}\right]^{1/2}, \qquad m=1,2,3.$$

The transitional Pearcey approximation, that applies in the immediate vicinity of the cusp caustic, can be found in [Q13]. Note that the above analysis applies equally to the bright and dark side of B_ϕ, the key difference being that the triplets ϑ_m and t_m are each comprised of one real and two (complex-conjugate) roots in the latter case. In situations where $\psi^{(4)}(0)<0$, the problem is resolved by applying (B 5) to the complex conjugate of (B 1).

Swallowtail catastrophe. In this case that is affiliated with four (real or complex) stationary points, two cusped edges, known as *ribs*, meet at a point. This type of catastrophe is classified as the universal unfolding of germ t^5 with codimension three and normal form $t^5 + c_3\,t^3 + c_2\,t^2 + c_1\,t$. The uniform asymptotic approximation of the diffraction integral (B 1) endowed with this type of caustics can be written as

$$k^{-1/2}\int_{-\infty}^{\infty} \mathscr{F}(\vartheta)\, e^{\mathrm{i}k\psi(\vartheta)}\,\mathrm{d}\vartheta = e^{\mathrm{i}k\psi_\circ}\sum_{m=0}^{3} k^{-(7+2m)/10} f_m\, S_{,m}(c_1 k^{\frac{4}{5}}, c_2 k^{\frac{3}{5}}, c_3 k^{\frac{2}{5}}) + O(k^{-3/2}), \tag{B 6}$$

in terms of the swallowtail function and its derivatives

$$S(b_1,b_2,b_3) = \int_{-\infty}^{\infty} e^{\mathrm{i}(\tau^5 + b_3\tau^3 + b_2\tau^2 + b_1\tau)}\,\mathrm{d}\tau, \qquad S_{,0} = S, \qquad S_{,m} = \frac{1}{\mathrm{i}}\frac{\partial S}{\partial b_m} \quad (m=1,2,3)$$

see [Q9]. By invoking the same strategy as in the cusp case, the control parameters (c_1, c_2, c_3) and phase offset $\psi_\circ$ are obtained by solving the system of nonlinear equations

$$\psi_\circ + c_1\,t_m + c_2\,t_m^2 + c_3\,t_m^3 + t_m^5 = \psi(\vartheta_m), \qquad m=1,2,3,4,$$

where ϑ_m are the stationary points of $\psi(\vartheta)$, and t_m are their counterparts in the t-space satisfying $5\,t_m^4 + 3\,c_3 t_m^2 + 2\,c_2\,t_m + c_1 = 0$. The remaining coefficients in (B 6) are determined from the linear set of equations

$$f_0 + f_1 t_m + f_2 t_m^2 + f_3 t_m^3 = \mathscr{F}(\vartheta_m)\left[\frac{20\,t_m^3 + 6\,c_3 t_m + 2\,c_2}{\psi^{(2)}(\vartheta_m)}\right]^{1/2}, \qquad m=1,2,3,4,$$

In the immediate vicinity of B_ϕ (where two or more stationary points coalesce), the above solution breaks down and is replaced by the transitional approximation, see [Q9, Q10].

(b) Hessian matrix of corank two

From the results in Appendix A(c), one finds that the rank of the Hessian matrix (A 1) vanishes only for two nested degenerate configurations, namely i) $\boldsymbol{d}\cdot\boldsymbol{a}_2 = 0$ and $|\boldsymbol{d}\cdot\boldsymbol{n}|^2 = \rho_2/\rho_1 < 1$, and ii) $|\boldsymbol{d}\cdot\boldsymbol{n}|^2 = \rho_2/\rho_1 = 1$. In both cases, the corank-two degeneracy occurs for sampling points where

$$r = |\boldsymbol{x}^\circ - \boldsymbol{\zeta}_{\mathrm{II}}^-| \to r_1, \qquad r_1 = r_2 = \tfrac{1}{2}\,\rho_1|\boldsymbol{d}\cdot\boldsymbol{n}|, \qquad \boldsymbol{x}^\circ \in \mathrm{II}^-.$$

To identify the class of catastrophes describing each case, it is necessary to expose the germ of the phase function $\phi = \boldsymbol{\zeta}\cdot\boldsymbol{d} - r$ in (3.7), characterizing its behavior when all nearby stationary points coalesce [Q2] as $r \to r_1$. To this end, consider first the third-order expansion of $\phi(\eta^1, \eta^2)$ for the case when $\rho_2/\rho_1 < 1$. Assuming the principal curvatures ρ_1 and ρ_2 to be locally constant, (3.20) can be expanded in Taylor series as

$$\phi(\eta^1,\eta^2) \simeq \phi_\circ + \frac{\boldsymbol{d}\cdot\boldsymbol{a}_1}{\rho_1}\left[\frac{g_{11}}{\rho_1}(\eta^1)^3 + \frac{g_{22}}{\rho_2}\,\eta^1(\eta^2)^2\right](g_{11})^{1/2}, \qquad \rho_2/\rho_1 < 1, \qquad \text{(B 7)}$$

where $\phi_\circ = \phi(\zeta_{\rm II}^-)$. On introducing the linear mapping $(\eta^1,\eta^2)\to(s,t)$ by way of

$$\eta^1 = \frac{1}{\sqrt{g_{11}}}\left(\frac{4\,\boldsymbol{d}\cdot\boldsymbol{a}_1}{{\rho_1}^2}\right)^{-\frac{1}{3}}(t+s), \qquad \eta^2 = \frac{|\boldsymbol{d}\cdot\boldsymbol{n}|\sqrt{3}}{\sqrt{g_{22}}}\left(\frac{4\,\boldsymbol{d}\cdot\boldsymbol{a}_1}{{\rho_1}^2}\right)^{-\frac{1}{3}}(t-s), \qquad \text{(B 8)}$$

one obtains (up to a constant) the normal cubic form s^3+t^3 of the phase function at $r=r_1$ which is of codimension three [Q6]. This particular germ corresponds to the *hyperbolic umbilic* catastrophe listed in Table 2, and is geometrically described by a cusp line touching a fold surface at the focus. In this case there are four interacting (real or complex) stationary points whose coalescence entails three control parameters (c_1,c_2,c_3), and their topology is such that the phase function can be transformed, in the neighborhood of $r=r_1$, into the normal form $s^3+t^3+c_3\,s\,t+c_2\,t+c_1 s$ via a diffeomorphism. The uniform asymptotic approximation of (3.7) due to this type of diffraction catastrophe [Q8] can be computed as

$$\int_{S^{\rm f}} f(\zeta)\,e^{{\rm i}k\phi(\eta^1,\eta^2)}\,{\rm d}S_\eta = e^{{\rm i}k\phi_\circ}\sum_{m=0}^{2} k^{-(2+m)/3} f_m\, H_{,m}(c_1k^{\frac{2}{3}}, c_2k^{\frac{2}{3}}, c_3k^{\frac{1}{3}}) + O(k^{-5/3}), \quad \text{(B 9)}$$

in terms of the hyperbolic-umbilic canonical integral and its derivatives

$$H(b_1,b_2,b_3) = \int_{-\infty}^{\infty}\int_{-\infty}^{\infty} e^{{\rm i}(\sigma^3+\tau^3+b_3\sigma\tau+b_2\tau+b_1\sigma)}\,{\rm d}\sigma\,{\rm d}\tau,$$

$$H_{,0} = H, \qquad H_{,1} = \frac{1}{\rm i}\sum_{j=1}^{2}\alpha_j\frac{\partial H}{\partial b_j}, \qquad H_{,2} = \frac{1}{\rm i}\frac{\partial H}{\partial b_3}.$$

The procedure for computing the control parameters (c_1,c_2,c_3) follows the same logic as that outlined in the previous section and entails transforming $\phi(\eta^1,\eta^2)$ to the hyperbolic-umbilic normal form, see [Q8, Q12] for details. Further, the coefficients $f_0, f_1\alpha_1, f_1\alpha_2$ and f_2 in (B 9) are obtained [Q14] by expanding the non-exponential part of the integrand as

$$f(\zeta)\,\frac{{\rm d}S_\eta}{{\rm d}s\,{\rm d}t} \simeq f_0 + f_1(\alpha_1 s+\alpha_2 t) + f_2\,s\,t, \qquad \zeta = \zeta(\eta^1,\eta^2). \qquad \text{(B 10)}$$

As examined earlier, the remaining configuration from Appendix A(c) resulting in a corank-two Hessian of the phase function is given by $|\boldsymbol{d}\cdot\boldsymbol{n}|^2 = \rho_2/\rho_1 = 1$ and $r=r_1=r_2$. In this case, the apex of $S^{\rm f}$ is also an umbilic point of the exposed boundary, and the third-order derivatives in (B 7) uniformly vanish. Accordingly, the class of caustics involved in this case is at least of codimension four, i.e. $\text{cod}(\phi)\geqslant 4$ which is beyond the scope of present investigation.

For completeness the reader is reminded that depending on the shape of $S^{\rm f}$, the corank-two Hessian of the phase function may further be affiliated with "global" caustics, which involve third- and higher-order surface properties – and thus (possibly) additional types of degeneracy. Within the framework of this study which is limited to $\text{cod}(\phi)\leqslant 3$, the only remaining class of catastrophes meeting this requirement is that of the *elliptic umbilic*, see Table 2. In this case, the leading asymptotic behavior of the diffraction integral is $O(k^{-2/3})$ [Q1], i.e. the same as that for the hyperbolic umbilic catastrophe.

As an illustration, example behavior of the canonical integrals featured in this section is plotted in Fig. 16, including their large-argument asymptotics as applicable.

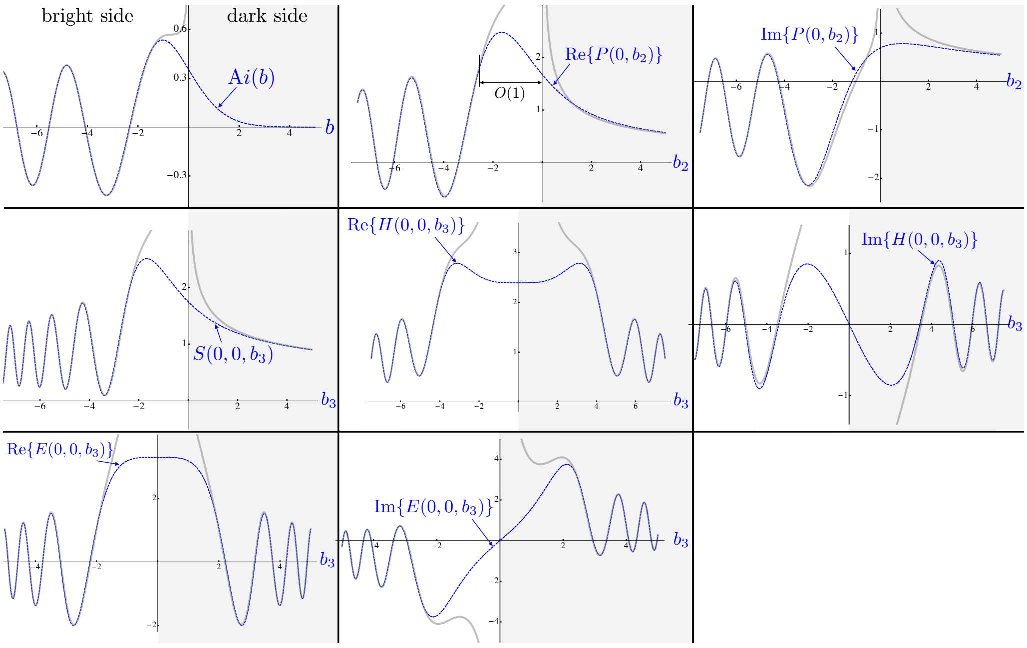

Figure 16. Elements of diffraction patterns (dashed lines) in the normalized control space $\boldsymbol{b}$ along with their large-argument asymptotic expansion (solid grey lines) for catastrophes of codimension less than four: fold, cusp, swallowtail, hyperbolic umbilic, end elliptic umbilic (left-to-right, top-to-bottom).

(c) Neutralizer functions

For generic $\mathscr{F}$ and ψ, the contribution of a given set of coalescing stationary points of ψ to the one-dimensional integral in (B 1) is evaluated via the partition of unity, namely

$$1=\sum_j g_j(\vartheta)+\tilde{g}(\vartheta) \qquad \Rightarrow \qquad \mathscr{F}(\vartheta)=\sum_j \mathscr{F}_j(\vartheta)+\tilde{\mathscr{F}}(\vartheta), \qquad \vartheta\in\mathbb{R},$$

where $\mathscr{F}_j=\mathscr{F}g_j$, and g_j (called the Van der Corput neutralizers) isolate the individual clusters of interacting stationary points. Assuming that the given cluster is enclosed by g_m, the sought contribution is accordingly computed as

$$k^{-\frac{1}{2}}\int_{-\infty}^{\infty}\mathscr{F}_m(\vartheta)\,\mathrm{e}^{\mathrm{i}k\psi(\vartheta)}\,\mathrm{d}\vartheta. \tag{B 11}$$

As examined for instance in [Q3], g_j are designed to: i) be infinitely differentiable, ii) equal unity over the support of germane (stationary point) interaction, and iii) vanish over the support of the remaining clusters. One example of a function meeting these requirements [Q4] is given by $g(\vartheta)=h(\vartheta)h(-\vartheta)/h_0^2$, where

$$h(x)=\int_x^{\infty}e(\delta-s)\,e(s-\epsilon)\,\mathrm{d}s, \qquad e(s)=\left\{\begin{array}{ll}0, & s\leqslant 0\\ e^{-1/s}, & s>0\end{array}\right., \qquad 0<\epsilon<\delta$$

and

$$h_0=\int_{\epsilon}^{\delta}e(\delta-s)\,e(s-\epsilon)\,\mathrm{d}s.$$

In particular, it is trivial to show that such infinitely differentiable function equals unity (resp. zero) for $|\vartheta|<\epsilon$ (resp. $|\vartheta|>\delta$).

Note that the concept of neutralizer functions extends naturally to surface (and in general higher-dimensional) integrals, see e.g. [Q5].

References

Q1 M. V. Berry, J. F. Nye, and F. J. Wright. The elliptic umbilic diffraction catastrophe. *Philos. Trans. R. Soc. London*, 291:453–484, 1979.

Q2 M. V. Berry and C. Upstill. Catastrophe optics: Morphologies of caustics and their diffraction patterns. *Progress in Optics*, 18:257–346, 1980.

Q3 N. Bleistein. *Mathematical Methods for Wave Phenomena*. Academic Press, London, 1984.

Q4 V. A. Borovikov. *Uniform Stationary Phase Method*. Instit. Electrical Engineers, London, 1994.

Q5 O. P. Bruno and C. A. Geuzaine. An O(1) integration scheme for three-dimensional surface scattering problems *Comp. Appl. Math.*, 204:463–476, 2007. Instit. Electrical Engineers, London, 1994.

Q6 P. L. Castrigiano and S. A. Hayes. *Catastrophe Theory*. Addison-Wesley, 1993.

Q7 C. Chester, B. Friedman, and F. Ursell. An extension of the method of steepest descents. *Proc. Camb. Phil. Soc.*, 53(599–611), 1957.

Q8 J. N. L. Connor. Asymptotic evaluation of multidimensional integrals for the S matrix in the semiclassical theory of inelastic and reactive molecular collisions. *Mol. Phys.*, 25:181–191, 1973.

Q9 J. N. L. Connor. Catastrophes and molecular collisions. *Mol. Phys.*, 31:33–55, 1976.

Q10 J. N. L. Connor, P. R. Curtis, and D. Farrelly. The uniform asymptotic swallowtail approximation: practical methods for oscillating integrals with four coalescing saddle points. *Phys. A: Math. Gen.*, 17:283–310, 1984.

Q11 E. Kreyszig. *Differential Geometry*. Dover, 1991.

Q12 P. A. Martin and G. R. Wickham. *Wave Asymptotics*. Cambridge University Press, 1992.

Q13 J. J. Stamnes. *Waves in Focal Regions*. Taylor & Francis, New York, 1986.

Q14 R. A. W. Young. *The Uniform Hyperbolic Umbilic Approximation*. ProQuest, UMI Dissertations Publishing, 1986.

C. Existence and uniqueness of the stationary point $\zeta_{\rm II}^{+}$

Consider a convex domain $D\subset\mathbb{R}^3$ bounded by a smooth closed surface $S=\partial D$. As examined e.g. in [R1], for each $\boldsymbol{x}\in\mathbb{R}^3\backslash\overline{D}$ there exists a unique normal projection on S, $\boldsymbol{x}^*$, such that

$$\widehat{\boldsymbol{x}^*-\boldsymbol{x}} \;=\; -\,\boldsymbol{n}(\boldsymbol{x}^*), \qquad \boldsymbol{x}^*\in S. \tag{C 1}$$

Next, consider the perturbation of $\boldsymbol{x}$ by $\mathrm{d}\boldsymbol{x}$ as shown in Fig. 17, where

$$\mathrm{d}_{\rm T}\boldsymbol{x} \;=\; \mathrm{d}\boldsymbol{x} - (\mathrm{d}\boldsymbol{x}\cdot\boldsymbol{n})\,\boldsymbol{n}(\boldsymbol{x}^*)$$

signifies the "tangential" component of $\mathrm{d}\boldsymbol{x}$ that is perpendicular to $\boldsymbol{n}$. Letting further $\mathrm{d}\boldsymbol{x}^*\perp\boldsymbol{n}$ denote the perturbation of the affiliated projection point, one finds that

$$\mathrm{d}\boldsymbol{n} \;=\; \boldsymbol{n}(\boldsymbol{x}^*+\mathrm{d}\boldsymbol{x}^*) - \boldsymbol{n}(\boldsymbol{x}^*) \;=\; \alpha\,(\mathrm{d}_{\rm T}\boldsymbol{x}-\mathrm{d}\boldsymbol{x}^*), \tag{C 2}$$

where $\alpha>0$ is the scaling coefficient dependent on distance $|\boldsymbol{x}^*-\boldsymbol{x}|$. With reference to the orthonormal basis $(\boldsymbol{a}_1,\boldsymbol{a}_2,\boldsymbol{n})$ where $\boldsymbol{a}_1$ and $\boldsymbol{a}_2$ are the principal directions of S at $\boldsymbol{x}^*$, the formulae of Rodrigues [R2] demonstrate that for a convex domain

$$\mathrm{d}\boldsymbol{n} \;=\; \rho_1^{-1}(\mathrm{d}\boldsymbol{x}^*\!\cdot\boldsymbol{a}_1)\,\boldsymbol{a}_1 \;+\; \rho_2^{-1}(\mathrm{d}\boldsymbol{x}^*\!\cdot\boldsymbol{a}_2)\,\boldsymbol{a}_2, \tag{C 3}$$

where ρ_1 and ρ_2 denote the principal radii of curvature. On contracting the difference between (C 2) and (C 3) by $\boldsymbol{a}_p$ ($p{=}1,2$) one finds that

$$\mathrm{d}\boldsymbol{x}^*\!\cdot\boldsymbol{a}_p \;=\; \frac{\alpha\,\rho_p}{1+\alpha\rho_p}\,(\mathrm{d}_{\rm T}\boldsymbol{x}\cdot\boldsymbol{a}_p), \quad\Longrightarrow\quad \mathrm{d}\boldsymbol{x}^*\!\cdot\mathrm{d}\boldsymbol{x} \;=\; \sum_{p=1}^{2}\frac{\alpha\,\rho_p}{1+\alpha\rho_p}\,(\mathrm{d}_{\rm T}\boldsymbol{x}\cdot\boldsymbol{a}_p)^2 \;>\; 0, \tag{C 4}$$

as long as $\mathrm{d}\boldsymbol{x}\nparallel\boldsymbol{n}$. Here it is also noted that

$$\mathrm{d}r \;=\; \tfrac{1}{2}\,r\,\mathrm{d}\boldsymbol{n}\cdot\mathrm{d}\boldsymbol{n} \;+\; \mathrm{d}\boldsymbol{x}\cdot\boldsymbol{n} \;>\; 0 \qquad \text{when} \qquad \mathrm{d}\boldsymbol{x}\cdot\boldsymbol{n}>0, \qquad r=|\boldsymbol{x}^*-\boldsymbol{x}|. \tag{C 5}$$

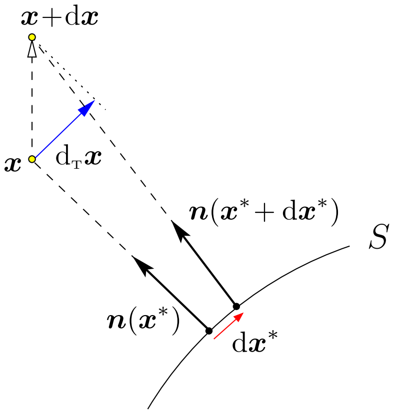

Figure 17. Perturbation of the normal projection, $\boldsymbol{x}^*$, of $\boldsymbol{x}\in\mathbb{R}^3\backslash\overline{D}$ on S.

Proposition C.1. For each sampling point $\boldsymbol{x}^{\rm o}\in\mathbb{R}^3\backslash\bar{\mathscr{L}}^{\pm}$ where $\mathscr{L}^{\pm}(\boldsymbol{d})$ are open "half" cylinders defined in (3.12), there exists a unique stationary point $\boldsymbol{\zeta}_{\rm II}^{+}\in S^{\rm f}$ given by the second of (3.11).

Proof. With reference to Fig. 18, consider the line L parallel to $\boldsymbol{d}$ passing through $\boldsymbol{x}^{\rm o}$, and let $\boldsymbol{z}$ be the reference point on this line such that $(\boldsymbol{z}-\boldsymbol{z}^*)\perp\boldsymbol{d}$, where $\boldsymbol{z}^*$ is the normal projection of $\boldsymbol{z}$ on S according to (C 1). In this setting, it is instructive to examine the set of trial points $\boldsymbol{x}\in L$ "above" $\boldsymbol{z}$ specified by

$$\boldsymbol{x}\in L^{\rm f}, \qquad L^{\rm f}=\{\boldsymbol{\xi}\colon\, \boldsymbol{\xi}=\boldsymbol{z}+\chi(-\boldsymbol{d}),\; \chi>0\}.$$

In light of the earlier discussion, for any $\boldsymbol{x}\in L^{\rm f}$ there exists a unique normal projection $\boldsymbol{x}^*\in S^{\rm f}$. In general, vectors $\boldsymbol{x}^*-\boldsymbol{x}$ are not coplanar when $\boldsymbol{x}\in L^{\rm f}$. On taking $\mathrm{d}\boldsymbol{x}=\mathrm{d}\chi(-\boldsymbol{d})$ and recalling that

$\boldsymbol{n}\cdot\boldsymbol{d} < 0$ on $S^{\rm f}$, one finds from (C 6) that $r = |\boldsymbol{x}^* - \boldsymbol{x}|$ increases monotonically with $\chi > 0$. From Fig. 18, it is also seen that $\forall \boldsymbol{x} \in L^{\rm f}$ there is a *unique* "trailing" point, $\boldsymbol{x}' \in L$, with coordinates

$$\boldsymbol{x}' = \boldsymbol{x} - \frac{r}{2|\boldsymbol{n}\cdot\boldsymbol{d}|}(-\boldsymbol{d}) = \boldsymbol{z} + \chi'(-\boldsymbol{d}), \qquad \chi' = (\boldsymbol{x}^* - \boldsymbol{z}^*)\cdot(-\boldsymbol{d}) + r\Big(|\boldsymbol{n}\cdot\boldsymbol{d}| - \frac{1}{2|\boldsymbol{n}\cdot\boldsymbol{d}|}\Big), \quad \text{(C 6)}$$

where $\boldsymbol{n}{=}\boldsymbol{n}(\boldsymbol{x}^*)$. The key feature of $\boldsymbol{x}'$ is that the normal projection of $\boldsymbol{x}$ on $S^{\rm f}$, $\boldsymbol{x}^*$, is the *stationary point* of type $\boldsymbol{\zeta}_{\rm II}^{+}$ for the integrals in (3.6) when the sampling point $\boldsymbol{x}^{\rm o}$ coincides with $\boldsymbol{x}'$. Taking $\mathrm{d}\boldsymbol{x} = \mathrm{d}\chi(-\boldsymbol{d})$ as before, it follows from (C 4) that the product $(\boldsymbol{x}^* - \boldsymbol{z}^*)\cdot(-\boldsymbol{d})$ increases monotonically with $\chi > 0$. By virtue of the latter equality, one also finds that $|\boldsymbol{n}\cdot\boldsymbol{d}|$ steadily traverses the interval $(0,1)$ with increasing $\chi{\in}(0,\infty)$. As a result, $\chi'(\chi)$ is a *monotonically increasing* function that maps $(0,\infty)$ onto $(-\infty,\infty)$. On denoting the χ' coordinate of the given sampling point $\boldsymbol{x}^{\rm o}{\in} L$ by $\chi'_{\rm o} \gtreqless 0$, it follows that there exists a unique value $\chi_{\rm o} > 0$, specified by the equality $\chi'(\chi_{\rm o}) = \chi'_{\rm o}$, such that $\boldsymbol{\zeta}_{\rm II}^{+} = \boldsymbol{x}^* {\in} S^{\rm f}$ for $\boldsymbol{x} = \boldsymbol{z} + \chi_{\rm o}(-\boldsymbol{d})$. ☐

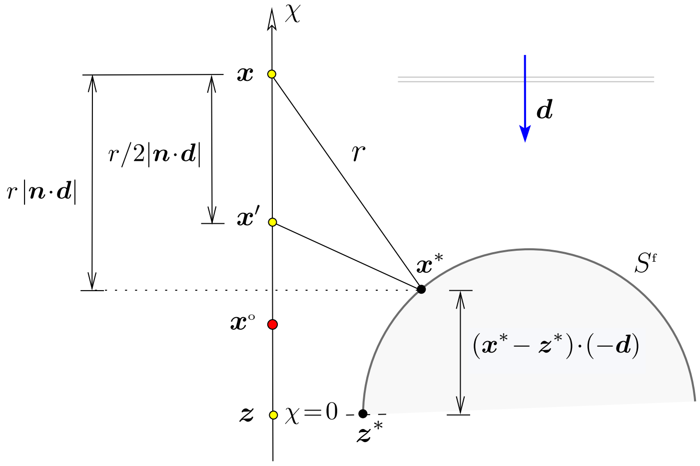

Figure 18. Geometrical platform for the identification of stationary point $\boldsymbol{\zeta}_{\rm II}^{+} \in S^{\rm f}$ affiliated with $\boldsymbol{x}^{\rm o}$.

Proposition C.2. For each sampling point $\boldsymbol{x}^{\rm o}{\in}\, \bar{\mathscr{L}}^{-}\backslash S^{\rm f}$ where $\mathscr{L}^{-}(\boldsymbol{d})$ is an open "half" cylinder defined in (3.12), there exists a unique stationary point $\boldsymbol{\zeta}_{\rm II}^{+} \in S^{\rm f}(\boldsymbol{d})$ given by the second of (3.11).

Proof. The proof of this claim follows that of Proposition C.1 and is omitted for brevity. The only notable differences are that: i) the reference point $\boldsymbol{z}$ is taken as the projection of $\boldsymbol{x}^{\rm o}$ along $\boldsymbol{d}$ on $S^{\rm f}$, and ii) the function $\chi'(\chi)$, which is again monotonically increasing, maps $(0,\infty)$ onto itself. For completeness, it is noted that for $\boldsymbol{x}^{\rm o}{\in}\, \partial\mathscr{L}^{-}\backslash S^{\rm f}$, $\boldsymbol{z}$ is the projection of $\boldsymbol{x}^{\rm o}$ along $\boldsymbol{d}$ on $\partial S^{\rm f}$. ☐

Proposition C.3. For any $\boldsymbol{x}^{\rm o}{\in}\, \bar{\mathscr{L}}^{+}\backslash S^{\rm f}$ where $\mathscr{L}^{+}$ is an open "half" cylinder defined in (3.12), there are no stationary points $\boldsymbol{\zeta}_{\rm II}^{+} \in S^{\rm f}$ given by the second of (3.11).

Proof. This claim is a direct consequence of the facts that D is convex and that every ray II^{+} emanating from $\boldsymbol{\zeta} \in S^{\rm f}$ is oriented toward the exterior of D, see Fig. 2. ☐

Remark. For reasons detailed in Section 3(d), the stationary phase approximation (3.17) is superseded by the near-boundary expansion (3.36) for sampling points close to $S^{\rm f}$. On the basis of this observation and Propositions C.1–C.3, one finds that the domain where (3.17) applies is contained within $\mathbb{R}^3\backslash\bar{\mathscr{L}}^{+}$.

References

R1 N. Bleistein. *Mathematical Methods for Wave Phenomena*. Academic Press, London, 1984.
R2 E. Kreyszig. *Differential Geometry*. Dover, 1991.

D. On the accuracy of Kirchhoff approximation

To examine the ramifications of the Kirchhoff approximation (3.1) and (4.26) on the high-frequency TS analysis, consider the scattering by a convex Dirichlet obstacle as an example. Next, adopt the decomposition of obstacle's boundary $S = \partial D$ as

$$S \,=\, S_b \,\cup\, S_t \,\cup\, S_{ds},$$

where S_b, S_t, and S_{ds} denote respectively the *bright*, *transitional*, and *deep shadow* region [S1] schematically shown in Fig. 19. In the context of the present study one has $S^{\rm f} \subset S_b \cup S_t$, where $S^{\rm f}(\boldsymbol{d}) = \{\boldsymbol{x} \in S : \boldsymbol{n}(\boldsymbol{x})\cdot\boldsymbol{d} < 0\}$ and S_t is a ring-like neighborhood of $\partial S^{\rm f}$ of width $O(k^{-1/3})$ [S4]. With such premise, (3.1) can be written more precisely as

$$u \,=\, 0, \qquad u_{,n} = \left\{ \begin{array}{cc} 2\,u^i_{,n} & \text{on} \;\; S^{\rm f} \\ 0 & \text{otherwise} \end{array} \right\} + E \qquad \text{on} \quad S, \tag{D 1}$$

were E is the error of the Kirchhoff approximation. While *the phase* of E is obstacle-geometry-dependent [S4] and remains an open research question [S1], it can be shown [e.g. S3, S2, S4] that

$$u^i_{,n} \,=\, -\mathrm{i}k\,\boldsymbol{d}\cdot\boldsymbol{n}\,e^{-\mathrm{i}k\boldsymbol{\xi}\cdot\boldsymbol{d}} \quad \text{on} \quad S^{\rm f} \qquad \Longrightarrow \qquad E \,=\, \left\{ \begin{array}{ll} O(1) & \text{on}\; S_b \\ O(k^{2/3}) & \text{on}\; S_t \\ O(k^{2/3}) \times \exp\left(-\beta(k)s\right) & \text{on}\; S_{ds} \end{array} \right. , \tag{D 2}$$

for scattering by a smooth Dirichlet obstacle, where s denotes a diffracted surface ray (the so-called creeping ray) path into the shadow region, and $\beta(k) \geqslant 0$ describes the amplitude decay of creeping rays due to tangential shedding of energy into the medium [S5]. By virtue of this result, E can be shown to have no effect on the claim of Theorem 4.6 as elucidated below.

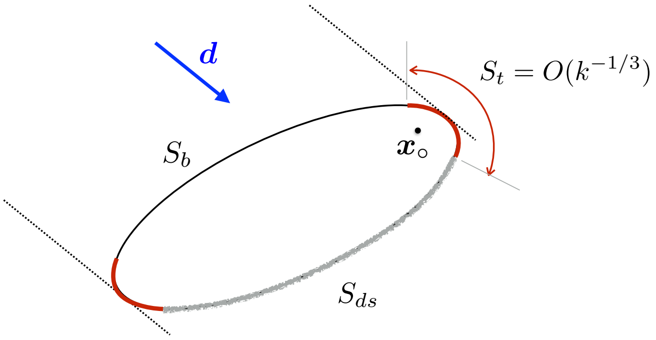

Figure 19. Schematics of the bright, transitional, and deep shadow regions comprising the surface of a scatterer.

- **Contribution of E to $\check{\mathsf{T}}$ via the boundary of the integration domain**. In the foregoing analysis, the contribution of critical points along the closed curve $\partial S^{\rm f}$ – the boundary of $S^{\rm f}$ – was neglected thanks to the fact that $u^i_{,n} = 0$ there. In the context of (D 1), there is likewise no "boundary" contribution due to E since the integration must be performed over the entire (closed) surface S.
- **Contribution of E to $\check{\mathsf{T}}$ via the near-boundary term $\mathsf{T}^\star$**. From the analysis in Section 3(d)ii and (D 2), it follows that the contribution of E over S to $\mathsf{T}^\star$ is $O(k^{2/3})$ in the case of illumination by a single plane wave. Accordingly the error in evaluating (4.23) and thus (4.25) due to E is at most $O(k^{2/3})$, which preserves the claim of Theorem 4.6.
- **Contribution of E to $\check{\mathsf{T}}$ via non-degenerate stationary points**. Thanks to (D 2), one finds that the contribution of E to T in (4.1) via the stationary points (i.e. the contribution of E to $\mathsf{T}^{\mathrm{II}^\pm}$) behaves at most as $O(k^{2/3})$ in the case of a single incident wave. As as a result, the claim of Theorem 4.6 remains unaltered by the stationary points of E – even if possible cancellation of their effect due to full-aperture illumination is altogether ignored.

- **Contribution of $E|_{S_b}$ to $\breve{\mathsf{T}}$ via diffraction catastrophes**. From (4.2) and (D 2), it can be seen that the single-indcident-wave contribution of E over S_b to T^c in (4.1) is at most $O(k^{1/3})$; accordingly it has no effect on the claim of Theorem 4.6.
- **Contribution of $E|_{S_t}$ to $\breve{\mathsf{T}}$ via diffraction catastrophes**. In contrast to the previous case, (4.2) and (D 2) demonstrate that the contribution of E over S_t to T^c may reach $O(k)$, which warrants further consideration. To this end, it can first be observed that the magnitude of E-catastrophes over the transitional region scales with wavenumber k as in Table 4.2 – diminished by a factor of $k^{-1/3}$. Next, one finds from the Melrose-Taylor corrected Kirchhoff approximation [S4] underpinning (D 2) that the neglected parts of integrands in (3.6) due to E contain rapidly-oscillating factors $e^{\mathrm{i}k\phi_E(\boldsymbol{\zeta})}$ whose phase permits leading-order approximation

$$\phi_{\scriptscriptstyle E}(\boldsymbol{\zeta}) \;=\; \boldsymbol{\zeta}\cdot\boldsymbol{d} \pm r - \tfrac{1}{3}Z^3(\boldsymbol{\zeta},\boldsymbol{d}). \tag{D 3}$$

Here Z is a smooth function that reflects the geometry of a scatterer and vanishes, to the first order, on ∂S^{f} where $\boldsymbol{d}\cdot\boldsymbol{n}=0$. Continuing upon the full-aperture analysis of diffraction catastrophes according to Kirchhoff approximation, the discussion is hereon focused on the phase function in (D 3) with the minus sign before r. In this setting, the developments in Sec. 4(b)ii can be extended to account for the leading-order correction $Z^3/3$, resulting in the analogue of (4.19) as

$$\phi_{\scriptscriptstyle E}(\boldsymbol{\zeta})\big|_{\boldsymbol{d}^{\circ}+\mathrm{d}\boldsymbol{d}} \simeq \tilde{\phi}_{\mathrm{E}_\circ} + \tfrac{1}{2}\phi^{(2)}_{\mathrm{E}_\circ}\sigma^2 + (\mathrm{d}\boldsymbol{d}\cdot\hat{\boldsymbol{s}})\,\sigma + \tfrac{1}{6}\,\phi'''_{\mathrm{E}_\circ}\tau^3 + (\mathrm{d}\boldsymbol{d}\cdot\hat{\boldsymbol{t}})\,\tau - Z^2\frac{\partial Z}{\partial \boldsymbol{d}}\cdot\mathrm{d}\boldsymbol{d}, \tag{D 4}$$

where $Z=Z(\boldsymbol{\zeta}^*\!+\!\sigma\,\hat{\boldsymbol{s}}\!+\!\tau\,\hat{\boldsymbol{t}},\boldsymbol{d}^{\circ})$ and $\tilde{\phi}_{\mathrm{E}_\circ}$, $\phi^{(2)}_{\mathrm{E}_\circ}$ and $\phi'''_{\mathrm{E}_\circ}$ are constants such that $\phi^{(2)}_{\mathrm{E}_\circ}=O(1)$ and $\phi'''_{\mathrm{E}_\circ}=O(1)$ under the premise of *fold catastrophe* at $\boldsymbol{\zeta}^*\!\in S_t$ when $\boldsymbol{d}=\boldsymbol{d}^{\circ}$. On recalling the framework of structural stability, the items of interest in (D 4) are the *linear* and *cubic* terms in τ – which permit computation of the sought initial slope $V_{\scriptscriptstyle E}=|c|/\mathrm{dist}(\boldsymbol{d},B^E_\phi)$ as $\boldsymbol{d}$ leaves the bifurcation set B^E_ϕ of $\phi_{\scriptscriptstyle E}$, where c is the featured *fold* control parameter. Here it is noted, however, that the last term in (D 4) behaves as

$$Z(\boldsymbol{\zeta}^*\!+\!\sigma\,\hat{\boldsymbol{s}}\!+\!\tau\,\hat{\boldsymbol{t}},\boldsymbol{d}^{\circ}) \;\leqslant\; O(k^{-1/3}), \qquad \boldsymbol{\zeta}^*\in S_t$$

due to the facts that: i) Z vanishes smoothly to the first order on ∂S^{f}, and ii) $St\supset\partial S^{\mathrm{f}}$ is a ring-shaped surface of width $O(k^{-1/3})$. As a result, the contributions of $Z^2(\partial Z/\partial\boldsymbol{d})\cdot\mathrm{d}\boldsymbol{d}$ to both linear and cubic terms in τ are $O(k^{-2/3})$, whereby the E-counterpart of (4.20) reduces to

$$V_{\scriptscriptstyle E} \;\geqslant\; \big|\tfrac{1}{2}\phi'''_{\mathrm{E}_\circ}\big|^{-\frac{1}{3}}\,\big(1+O(k^{-2/3})\big)\,|\boldsymbol{d}^{\circ}\!\cdot\boldsymbol{n}| \;\simeq\; \big|\tfrac{1}{2}\phi'''_{\mathrm{E}_\circ}\big|^{-\frac{1}{3}}\,|\boldsymbol{d}^{\circ}\!\cdot\boldsymbol{n}|, \tag{D 5}$$

noting that $\boldsymbol{n}=\boldsymbol{n}(\boldsymbol{\zeta}^*)$. When $\boldsymbol{\zeta}^*\in S_t$, it is clear from basic geometrical considerations that $|\boldsymbol{d}^{\circ}\!\cdot\boldsymbol{n}|\leqslant O(k^{-1/3})$, see Fig. 19. The question, however, is to determine the *lower bound* on $|\boldsymbol{d}^{\circ}\!\cdot\boldsymbol{n}|$ and thus that on $V_{\scriptscriptstyle E}$. To this end, one can show from (3.10), (3.11) and (D 3) that

$$\boldsymbol{\zeta}^*-\boldsymbol{x}^{\circ} \;=\; |\boldsymbol{\zeta}^*-\boldsymbol{x}^{\circ}|\,\big[\boldsymbol{d}^{\circ}+2|\boldsymbol{d}^{\circ}\!\cdot\boldsymbol{n}|\,\boldsymbol{n}(\boldsymbol{\zeta}^*)\big]+O(k^{-2/3}), \qquad \boldsymbol{\zeta}^*\in S_t\cap S^{\mathrm{f}}, \tag{D 6}$$

which again makes use of the fact that $Z(\boldsymbol{\zeta}^*,\boldsymbol{d}^{\circ})\leqslant O(k^{-1/3})$ in the transitional region. Assuming $|\boldsymbol{d}^{\circ}\!\cdot\boldsymbol{n}(\boldsymbol{\zeta}^*)|=O(k^{-\alpha})$ for some $0<\alpha<2/3$, (D 6) can be used to show – via tangent-plane approximation of S at $\boldsymbol{\zeta}^*$ – that the distance between $\boldsymbol{x}^{\circ}$ and its normal projection on S behaves as $|\ell|\simeq(\boldsymbol{\zeta}^*-\boldsymbol{x}^{\circ})\cdot\boldsymbol{n}(\boldsymbol{\zeta}^*)=O(k^{-\alpha}|\boldsymbol{\zeta}^*-\boldsymbol{x}^{\circ}|)$. Under the same hypothesis, one finds that $Z(\boldsymbol{\zeta}^*)=O(k^{-\alpha})$ and consequently, following the developments in Appendix A(a), that

$$|\boldsymbol{\zeta}^*-\boldsymbol{x}^{\circ}| \;=\; r_2 \,+\, O\big(Z(\boldsymbol{\zeta}^*)\big) \;=\; O(k^{-\alpha}) \qquad \text{when} \quad |\boldsymbol{d}^{\circ}\!\cdot\boldsymbol{n}(\boldsymbol{\zeta}^*)|=O(k^{-\alpha}), \quad 0<\alpha<2/3,$$

where r_2 is given by (A5) and behaves asymptotically as $r_2=O(|\boldsymbol{d}^{\circ}\!\cdot\boldsymbol{n}|)$ for $|\boldsymbol{d}^{\circ}\!\cdot\boldsymbol{n}|\ll 1$. In this setting one finds that for $|\boldsymbol{d}^{\circ}\!\cdot\boldsymbol{n}|=O(k^{-\alpha})$, the normal distance from $\boldsymbol{x}^{\circ}$ to the boundary is $|\ell|=O(k^{-2\alpha})$. As examined in Section 3(d), however, for sampling points with $|\ell|\leqslant O(k^{-1})$ the contribution of nearby critical points on S is universally computed via the near-boundary approximation (3.36). As a result, one obtains the lower bound $|\boldsymbol{d}^{\circ}\!\cdot\boldsymbol{n}|>O(k^{-1/2})$ for (D 5), whereby the E-analogue of (4.21) reads

$$|\tilde{B}^E_\phi|_{\mathrm{cod}(\phi)=1} \;\leqslant\; O\big(|\boldsymbol{d}^{\mathrm{o}}\!\cdot\!\boldsymbol{n}|^{-1}\, k^{-\sigma_m^{\min}}\big) \;=\; O\big(k^{1/2}\, k^{-2/3}\big) \;=\; O(k^{-1/6}). \tag{D 7}$$

On the basis of Table 4.2, (D 2), and (D 8), it immediately follows that the full-aperture contribution of the fold catastrophes ($\mathrm{cod}(\phi_E)=1$) of E over S_t scales, at most, as $O(k^{7/6}k^{-1/3}k^{-1/6})=O(k^{2/3})$ which leaves the claim of Theorem 4.6 unaffected. As argued earlier in Section 4(b)ii, the contribution of higher-order catastrophes in the transitional region is precluded by the regularity of the scattering surface S.

- **Contribution of $E|_{S_{ds}}$ to $\breve{\mathsf{T}}$ via diffraction catastrophes**. In this case one concludes, following the argument in Section 4(b)ii, that $V_{\scriptscriptstyle E}=O(1)$ owing to the absence of vanishing length scales (namely the vanishing distance $|\ell|$ from $\boldsymbol{x}^{\mathrm{o}}$ to S) there. As a result, the E-counterpart of (4.22) takes the form

$$|\tilde{B}^E_\phi|_{\mathrm{cod}(\phi_E)\geqslant 1} \;=\; \begin{cases} O\big(k^{-\sigma_m^{\min}}\big), & \mathrm{cod}(\phi_{\scriptscriptstyle E})=1 \\ O\big(k^{-2\sigma_m^{\min}}\big), & \mathrm{cod}(\phi_{\scriptscriptstyle E})>1 \end{cases} \tag{D 8}$$

where $\sigma_m^{\min}$ are given in Table 2. From this result and (D 2), it follows that the full-aperture contribution of catastrophes with $\mathrm{cod}(\phi_{\scriptscriptstyle E})\leqslant 3$ due to E over S_{ds} scales, at most, as $O(k^{1/3})$ – which again preserves the claim of Theorem 4.6.

References

S1 A. Asheim and D. Huybrechs. Extraction of uniformly accurate phase functions across smooth shadow boundaries in high frequency scattering problems. *SIAM J. Appl. Math.*, 74:454–476, 2014.

S2 J.B. Keller. Geometrical theory of diffraction. *J. Opt. Soc. Amer.*, 52:116–130, 1962.

S3 B.R. Levy and J.B. Keller. Diffraction by a smooth object. *Comm. Pure Appl. Math.*, 12:159–209, 1959.

S4 R.B. Melrose and M.E. Taylor. Near peak scattering and the corrected Kirchhoff approximation for a convex obstacle. *Advances in Mathematics*, 55:242–315, 1985.

S5 M. Motamed and O. Runborg. A fast phase space method for computing creeping rays. *J. Comp. Phys.*, 219:276–295, 2006.

E. Reconstruction of a Neumann obstacle

(a) Single plane-wave incidence

Taking advantage of the ideas presented in Section 3 for a sound-soft obstacle, the proof of Theorem 4.7 is outlined in more detail with the aim of deriving (4.27). To this end, the use in (2.8) of the physical optics approximation for a *sound-hard* obstacle (4.26) yields

$$\begin{aligned}\mathsf{T}(\boldsymbol{x}^{\mathrm{o}}) \;=\; & -2\,\mathrm{Re}\Big[\mathsf{A}\,\nabla \mathsf{u}^{i}(\boldsymbol{x}^{\mathrm{o}})\cdot\!\int_{\mathsf{S}^{\mathrm{f}}} \overline{\mathsf{u}^{i}}(\boldsymbol{\zeta})\,\boldsymbol{n}(\boldsymbol{\zeta})\cdot\!\int_{\mathit{\Gamma}^{\mathrm{obs}}} \nabla\overline{\mathsf{G}}(\boldsymbol{\xi},\boldsymbol{\zeta})\otimes\nabla\mathsf{G}(\boldsymbol{\xi},\boldsymbol{x}^{\mathrm{o}})\,\mathrm{d}\mathit{\Gamma}_{\xi}\,\mathrm{d}\mathsf{S}_{\zeta} \\ & \qquad - \mathsf{B}\,\mathsf{u}^{i}(\boldsymbol{x}^{\mathrm{o}})\int_{\mathsf{S}^{\mathrm{f}}} \overline{\mathsf{u}^{i}}(\boldsymbol{\zeta})\,\boldsymbol{n}(\boldsymbol{\zeta})\cdot\!\int_{\mathit{\Gamma}^{\mathrm{obs}}} \nabla\overline{\mathsf{G}}(\boldsymbol{\xi},\boldsymbol{\zeta})\,\mathsf{G}(\boldsymbol{\xi},\boldsymbol{x}^{\mathrm{o}})\,\mathrm{d}\mathit{\Gamma}_{\xi}\,\mathrm{d}\mathsf{S}_{\zeta}\Big]. \qquad \text{(E 1)}\end{aligned}$$

Thanks to (2.13) and (2.14), one accordingly finds that

$$\mathsf{T}(\boldsymbol{x}^{\mathrm{o}}) \;=\; 2k^2\,\mathrm{Re}\Big\{\mathsf{A}\,(\mathrm{i}\,\mathrm{e}^{-\mathrm{i}k\boldsymbol{x}^{\mathrm{o}}\cdot\boldsymbol{d}})\,(\mathsf{J}_3-\mathsf{J}_4) \;+\; \mathsf{B}\,(\mathrm{e}^{-\mathrm{i}k\boldsymbol{x}^{\mathrm{o}}\cdot\boldsymbol{d}})\,\mathsf{J}_5\Big\}, \qquad \text{(E 2)}$$

where

$$\begin{aligned} J_3 \;&=\; \int_{S^{\mathrm{f}}} e^{\mathrm{i}k\boldsymbol{\zeta}\cdot\boldsymbol{d}}\,\frac{\varkappa}{kr}\Big[3\,\mathrm{Re}\big(G(\boldsymbol{x}^{\mathrm{o}},\boldsymbol{\zeta})\big) + \Big(\frac{3}{kr}-kr\Big)\mathrm{Im}\big(G(\boldsymbol{x}^{\mathrm{o}},\boldsymbol{\zeta})\big)\Big]\,\mathrm{d}S_{\boldsymbol{\zeta}}, \\ J_4 \;&=\; \int_{S^{\mathrm{f}}} e^{\mathrm{i}k\boldsymbol{\zeta}\cdot\boldsymbol{d}}\,\frac{1}{kr}\Big[\mathrm{Re}\big(G(\boldsymbol{x}^{\mathrm{o}},\boldsymbol{\zeta})\big) + \frac{1}{kr}\mathrm{Im}\big(G(\boldsymbol{x}^{\mathrm{o}},\boldsymbol{\zeta})\big)\Big]\,\boldsymbol{d}\cdot\boldsymbol{n}(\boldsymbol{\zeta})\,\mathrm{d}S_{\boldsymbol{\zeta}}, \qquad \text{(E 3)} \\ J_5 \;&=\; \int_{S^{\mathrm{f}}} e^{\mathrm{i}k\boldsymbol{\zeta}\cdot\boldsymbol{d}}\,\Big[\mathrm{Re}\big(G(\boldsymbol{x}^{\mathrm{o}},\boldsymbol{\zeta})\big) + \frac{1}{kr}\,\mathrm{Im}\big(G(\boldsymbol{x}^{\mathrm{o}},\boldsymbol{\zeta})\big)\Big]\;\boldsymbol{n}(\boldsymbol{\zeta})\cdot(\widehat{\boldsymbol{x}^{\mathrm{o}}-\boldsymbol{\zeta}})\,\mathrm{d}S_{\boldsymbol{\zeta}}, \end{aligned}$$

and $\varkappa = (\widehat{\boldsymbol{x}^{\mathrm{o}}-\boldsymbol{\zeta}})\otimes(\widehat{\boldsymbol{x}^{\mathrm{o}}-\boldsymbol{\zeta}}):\boldsymbol{d}\otimes\boldsymbol{n}(\boldsymbol{\zeta})$.

Contribution of non-degenerate stationary points. On substituting (2.3) into (E 3), one finds that the Fourier-type surface integrals J_m $(m=3,4,5)$ feature the same phase function $\boldsymbol{\zeta}\cdot\boldsymbol{d}\pm r$ as J_1 and J_2 in (3.4). Thus the *non-uniform* asymptotic approximation (3.8), specifying the contribution of isolated stationary points $\boldsymbol{\zeta}^*$ to T, remains valid. Further, the loci of $\boldsymbol{\zeta}^*$ according to (3.11) and the nature of the affiliated Hessian matrix $A_{pq}(\boldsymbol{\zeta}^*)$, examined in Appendix A(a), stay the same. As a result, the contribution of non-degenerate critical points to (E 2) can be computed from (E 3), (3.14), (3.16) and (3.18) as

$$\mathsf{T}^{\mathrm{I}^{\pm}}(\boldsymbol{x}^{\mathrm{o}}) \;\overset{k^{-1}}{=\!=}\; \pm\,\frac{1}{2r}\Big\{2\,\mathsf{A}+\mathsf{B}\Big\}, \quad \mathsf{r} = |\boldsymbol{x}^{\mathrm{o}}-\boldsymbol{\zeta}_{\mathrm{I}}^{\pm}|, \quad \boldsymbol{x}^{\mathrm{o}}\in \mathrm{I}^{\pm}\cap(\mathscr{B}_1\backslash\mathscr{N}_{\epsilon}); \qquad \text{(E 4)}$$

$$\begin{aligned}\mathsf{T}^{\mathrm{II}^{+}}(\boldsymbol{x}^{\mathrm{o}}) \;\overset{1}{=}\; & -\frac{k\,\sqrt{\rho_1\,\rho_2}}{4\sqrt{(r+r_1)(r+r_2)}}\,\mathrm{Im}\Big[e^{2\mathrm{i}k(\boldsymbol{d}\cdot\boldsymbol{n})^2 r}\Big]\Big\{\mathsf{A}\,\big(1-2(\boldsymbol{d}\cdot\boldsymbol{n})^2\big)+\mathsf{B}\Big\}, \\ & r = |\boldsymbol{x}^{\mathrm{o}}-\boldsymbol{\zeta}_{\mathrm{II}}^{+}|, \quad \boldsymbol{x}^{\mathrm{o}}\in \mathrm{II}^{+}\cap(\mathscr{B}_1\backslash\mathscr{N}_{\epsilon}), \quad \boldsymbol{n} = \boldsymbol{n}(\boldsymbol{\zeta}_{\mathrm{II}}^{+}); \qquad \text{(E 5)}\end{aligned}$$

and

$$\begin{aligned}\mathsf{T}^{\mathrm{II}^{-}}(\boldsymbol{x}^{\mathrm{o}}) \;\overset{1}{=}\; & -\frac{k\,\sqrt{\rho_1\,\rho_2}}{4\sqrt{|(r-r_1)(r-r_2)|}}\,\mathrm{Re}\Big[e^{-2\mathrm{i}k(\boldsymbol{d}\cdot\boldsymbol{n})^2 r+\mathrm{i}(\mathrm{sgn}\,A_{pq})\pi/4}\Big]\Big\{\mathsf{A}\,\big(1-2(\boldsymbol{d}\cdot\boldsymbol{n})^2\big)+\mathsf{B}\Big\} \\ & r = |\boldsymbol{x}^{\mathrm{o}}-\boldsymbol{\zeta}_{\mathrm{II}}^{-}|, \quad \boldsymbol{x}^{\mathrm{o}}\in (\mathrm{II}^{-}\backslash\mathscr{C}_{\mathrm{II}})\cap(\mathscr{B}_1\backslash\mathscr{N}_{\epsilon}), \quad \boldsymbol{n} = \boldsymbol{n}(\boldsymbol{\zeta}_{\mathrm{II}}^{-}) \qquad \text{(E 6)}\end{aligned}$$

assuming the stationary points of type I, II^+ and II^-, respectively.

Here it is worth noting that the contribution of $\mathsf{T}^{\mathrm{I}^{\pm}} = O(1)$ can be neglected due to the fact that $\mathsf{T}^{\mathrm{II}^{\pm}} = O(k)$. Moreover, apart from the sign difference, (E 5) and (E 6) carry exactly the same structure as their "sound-soft" counterparts (3.17) and (3.19).

Contribution of diffraction catastrophes. Owing to the fact that the TS formulas (3.4) and (E 2) share the phase function $\phi = \boldsymbol{\zeta}\cdot\boldsymbol{d} - r$, the analysis in Section 3(c) concerning the contribution of degenerate stationary points to the TS, namely T^c, remains unchanged.

Asymptotic expansion for $\boldsymbol{x}^{\rm o} \in \mathscr{N}_\epsilon$. At the stationary points $\boldsymbol{\zeta}^*$ of type $\rm{II}^{\pm}$, one has $|\boldsymbol{d}\cdot\boldsymbol{n}(\boldsymbol{\zeta}^*)| = |\boldsymbol{n}(\boldsymbol{\zeta}^*)\cdot(\widehat{\boldsymbol{x}^{\rm o} - \boldsymbol{\zeta}^*})|$ so that the kernels in J_m $(m = 3,4,5)$, when *evaluated at* $\boldsymbol{\zeta}^*$, are proportional to $|\boldsymbol{d}\cdot\boldsymbol{n}|$. With such remark, one may appeal to the argument as in Section 3(d)i to find the appropriate threshold, $\epsilon \geqslant 2\pi/k$, for the extent of $\mathscr{N}_\epsilon$ according to (3.5).

When $\boldsymbol{x}^{\rm o} \in \mathscr{N}_\epsilon$, the analyses in Sections 3(b) and 3(c) do not apply to the critical points on $\partial S^{\rm f}$ that are close to the point of normal projection, $\boldsymbol{x}^\star$. Further, the latter becomes a critical point itself as $\boldsymbol{x}^{\rm o} \to \boldsymbol{x}^\star$ due to a lack of differentiability of the kernels in (E 3). In this case, one may resort to the tangent-plane approximation as in Section 3(d)ii such that, by adopting the change of variables (3.30) with $\varepsilon = 0$, J_3 in (E 3) can be approximated as

$$\begin{aligned} J_3^\star \;=\; & \frac{e^{\mathrm{i}k\boldsymbol{x}^\star\cdot\boldsymbol{d}}}{4\pi}\int_0^\infty \frac{\varrho}{(kr_0)^4}\Big[3\cos(kr_0) + (kr_0 - \frac{3}{kr_0})\sin(kr_0)\Big]k\ell \times \\ & \times \int_0^{2\pi} e^{\mathrm{i}k\varrho d_t\cos(\theta)}\big(\boldsymbol{d}\cdot\boldsymbol{n}\,k\ell \;-\; d_t\,k\varrho\,\cos(\theta)\big)\mathrm{d}\theta\,\mathrm{d}(k\varrho), \quad \boldsymbol{x}^{\rm o}\in\mathscr{N}_\epsilon, \end{aligned} \tag{E 7}$$

where $\boldsymbol{n} = \boldsymbol{n}(\boldsymbol{x}^\star)$, $r_0 = \sqrt{\ell^2 + \varrho^2}$, and $d_t = \sqrt{1 - |\boldsymbol{d}\cdot\boldsymbol{n}|^2}$. Note that the outer integral in (E 7) has been conveniently extended to infinity by the use of an implicit neutralizer function [e.g. T2, T3]. The inner integral with respect to θ, on the other hand, can be expressed explicitly in terms of the Bessel functions of the first kind, namely $\mathrm{J}_0(d_t k\varrho)$ and $\mathrm{J}_1(d_t k\varrho)$. Thanks to the identity $\ell^2 = r_0^2 - \varrho^2$, thus obtained integral over $k\varrho$ can be rewritten as

$$\begin{aligned} J_3^\star \;=\; & \frac{e^{\mathrm{i}k\boldsymbol{x}^\star\cdot\boldsymbol{d}}}{2}\int_0^\infty \frac{\varrho}{(kr_0)^4}\Big[3\cos(kr_0) + (kr_0 - \frac{3}{kr_0})\sin(kr_0)\Big] \times \\ & \times \Big\{\boldsymbol{d}\cdot\boldsymbol{n}(kr_0)^2\mathrm{J}_0(d_t k\varrho) - \boldsymbol{d}\cdot\boldsymbol{n}(k\varrho_0)^2\mathrm{J}_0(d_t k\varrho) - \mathrm{i}d_t\,k\varrho\,k\ell\,\mathrm{J}_1(d_t k\varrho)\Big\}\mathrm{d}(k\varrho), \quad \boldsymbol{x}^{\rm o}\in\mathscr{N}_\epsilon. \end{aligned} \tag{E 8}$$

On integrating (E 8) by parts and making use of the integral identities in [T1], the leading-order contribution of $\boldsymbol{x}^\star$ to J_3 is found to read

$$J_3^\star \;=\; \frac{e^{\mathrm{i}k\boldsymbol{x}^\star\cdot\boldsymbol{d}}}{2k}\Big[\,\mathrm{i}\,d_t^2\,\sin(|\boldsymbol{d}\cdot\boldsymbol{n}|k\ell) \;-\; |\boldsymbol{d}\cdot\boldsymbol{n}|^2\Big(\cos(|\boldsymbol{d}\cdot\boldsymbol{n}|k\ell) - \frac{\sin(|\boldsymbol{d}\cdot\boldsymbol{n}|k\ell)}{|\boldsymbol{d}\cdot\boldsymbol{n}|k\ell}\Big)\Big], \quad \boldsymbol{x}^{\rm o}\in\mathscr{N}_\epsilon. \tag{E 9}$$

In a similar fashion, the leading-order contribution of $\boldsymbol{x}^\star$ to J_4 and J_5 can be obtained as

$$J_4^\star \;=\; \frac{|\boldsymbol{d}\cdot\boldsymbol{n}|}{2k^2\ell}\,e^{\mathrm{i}k\boldsymbol{x}^\star\cdot\boldsymbol{d}}\sin(|\boldsymbol{d}\cdot\boldsymbol{n}|k\ell), \qquad J_5^\star \;=\; -\frac{1}{2k}\,e^{\mathrm{i}k\boldsymbol{x}^\star\cdot\boldsymbol{d}}\sin(|\boldsymbol{d}\cdot\boldsymbol{n}|k\ell), \qquad \boldsymbol{x}^{\rm o}\in\mathscr{N}_\epsilon. \tag{E 10}$$

By substituting (E 9) and (E 10) into (E 2), one finds

$$\mathsf{T}^\star(\boldsymbol{x}^{\rm o}) \;\overset{1}{=}\; -\frac{k}{2}\,\sin(2k\ell|\boldsymbol{d}\cdot\boldsymbol{n}|)\Big\{\mathsf{A}\left(1 - 2(\boldsymbol{d}\cdot\boldsymbol{n})^2\right) + \mathsf{B}\Big\}, \qquad \boldsymbol{x}^{\rm o}\in\mathscr{N}_\epsilon \tag{E 11}$$

to be the leading asymptotic contribution of $\boldsymbol{x}^\star$ to T in the case of scattering by a Neumann obstacle.

On the basis of the above results, the "Neumann" contributions $\mathsf{T}^{\rm{II}^{\pm}}$, T^c and $\mathsf{T}^\star$ to the TS are found to behave as in (4.2), and are incorporated into (4.1) for further analysis.

Contribution of the boundary of the integration domain, $\partial S^{\rm f}$. In contrast to the case of a Dirichlet obstacle, the kernels of J_3 and J_5 in (E 3) entering the "Neumann" TS formula (E 2) do not vanish as $\boldsymbol{\zeta} \to \partial S^{\rm f}$, which warrants further consideration (recall that $J_2 \to 0$ in this case thanks to the fact that $\boldsymbol{d}\cdot\boldsymbol{n} = 0$ on $S^{\rm f}$). Note, however, that if $\boldsymbol{\zeta}^* \in \partial S^{\rm f}$ is a stationary point of $\boldsymbol{\zeta}\cdot\boldsymbol{d} \pm r$, the kernels of J_m $(m{=}3,5)$ both vanish there thanks to (3.11); thus, the contribution of such critical points can be ignored. On the basis of the high-frequency analysis of oscillatory integrals in [T2]

(Sec. 9.2.1 (a)), the contribution of $\partial S^{\rm f}$ to (E 3) can accordingly be computed as

$$J_m^{\partial S^{\rm f}} = k^{-1} \sum_{\pm} \int_{\partial \tilde{S}^{\rm f}} \frac{\rm i}{\phi^{\pm}_{,s}(t,0)}\, g_m^{\pm}(\boldsymbol{\zeta};\boldsymbol{d})\, e^{{\rm i}k\phi^{\pm}}\,{\rm d}t, \qquad \phi^{\pm}(t,s) = \boldsymbol{\zeta}\cdot\boldsymbol{d} \pm r, \qquad \boldsymbol{\zeta} = \boldsymbol{\zeta}(t,s), \tag{E 12}$$

where $m = 3,5$; $\partial\tilde{S}^{\rm f} \subset \partial S^{\rm f}$ excludes all $\boldsymbol{\zeta}^*$; t is the arclength parameter along $\partial S^{\rm f}$; and $s \geqslant 0$ is a curvilinear surface coordinate on $S^{\rm f}$, positive inward, that is orthogonal to t ($s{=}0$ on $S^{\rm f}$). The oscillatory line integrals in (E 12) can be evaluated via techniques introduced earlier, assuming structurally-stable caustics – if any – of codimension less than three (recall that cod($\phi^{\pm}$) cannot exceed two for 1D integrals). As a result the high-frequency asymptotic behavior of (E 2), i.e. the "Neumann" counterpart of (4.1), is found to include an *additional boundary contribution*

$$\mathsf{T}^{\partial S^{\rm f}} = O(k^{1/2+\beta}), \qquad 0 \leqslant \beta \leqslant \tfrac{3}{10}, \tag{E 13}$$

where the limits on β are established according to Table 2.

(b) Full source aperture

On recalling that the TS integral representations (3.3) and (E 2) share the *common* phase function pair $\boldsymbol{\zeta}\cdot\boldsymbol{d} \pm r$, one finds that the "Dirichlet" analysis in Sections 4(b)i and 4(b)ii applies equally to the reconstruction of a sound-hard obstacle. As a result, one has

$$\breve{\mathsf{T}}(\boldsymbol{x}^{\rm o}) \overset{k^{\nu}}{=} 1_{\breve{\mathscr{N}}_{\epsilon}}(\boldsymbol{x}^{\rm o}) \int_{\Omega} \mathsf{T}^{\star}\, d\Omega_{\boldsymbol{d}} \,+\, \int_{\tilde{B}_{\phi}} \mathsf{T}^{c}\, d\Omega_{\boldsymbol{d}} \,+\, \int_{S^{\pm}} \frac{|\boldsymbol{d}^{*}\!\cdot\boldsymbol{n}|}{r^2}\, \mathsf{T}^{I\!I^{\pm}} dS_{\boldsymbol{\zeta}} \,+\, \int_{\Omega} \mathsf{T}^{\partial S^{\rm f}}\, d\Omega_{\boldsymbol{d}}, \tag{E 14}$$

where $\nu \leqslant 1/2$ and

$$\int_{\tilde{B}_{\phi}} \mathsf{T}^{c}\, d\Omega_{\boldsymbol{d}} \;=\; O(k^{\alpha}), \quad \tfrac{1}{4} \leqslant \alpha \leqslant \tfrac{2}{3}, \qquad \int_{S^{\pm}} \frac{|\boldsymbol{d}^{*}\!\cdot\boldsymbol{n}|}{r^2}\, \mathsf{T}^{I\!I^{\pm}} dS_{\boldsymbol{\zeta}} \;=\; O(k^{\beta}), \quad 0 \leqslant \beta \leqslant \tfrac{1}{3}. \tag{E 15}$$

To compute the contribution of nearby critical points to (4.3) when $\boldsymbol{x}^{\rm o} \in \breve{\mathscr{N}}_{\epsilon}$, on the other hand, (E 11) can be integrated over $\Omega_{\boldsymbol{d}}$ as in Section 4(b)iii to obtain

$$\int_{\Omega} \mathsf{T}^{\star}\; {\rm d}\Omega_{\boldsymbol{d}} \;=\; \frac{-\pi\, k}{(k\ell)^3} \Big\{ \mathsf{A}\big(k\ell\cos(k\ell) - \sin(k\ell)\big)^2 + \mathsf{B}\,(k\ell)^2 \sin(k\ell)^2 \Big\}. \tag{E 16}$$

Remark 1. *In situations where a hidden Neumann obstacle D is reconstructed by sampling with a commensurate (i.e. sound-hard) vanishing scatterer, one should set* $(\mathsf{A},\mathsf{B}) = (3/2,-1)$ *according to Table* 1.

With (E 15) and (E 16) in place, the last step in the analysis is to evaluate the contribution of the boundary term $\mathsf{T}^{\partial S^{\rm f}}$ to the full-source-aperture TS variation (E 14). From the onset, it is seen that (E 13) itself may exceed the $O(k^{2/3})$ residual stated in Theorem 4.7 – which can possibly cause problems. By way of (E 3) and (2.3), however, it can be shown that $g_m^{\pm}$ in (E 12) carry the intrinsic properties

$$g_3^{\pm}(\cdot,\boldsymbol{d}) \;=\; -g_3^{\pm}(\cdot,-\boldsymbol{d}), \qquad g_5^{\pm}(\cdot,\boldsymbol{d}) \;=\; g_5^{\pm}(\cdot,-\boldsymbol{d}), \qquad g_m^{+} \;=\; \bar{g}_m^{-}, \quad m = 3,5 \tag{E 17}$$

where the overbar symbol denotes complex conjugation. Since the "bright" surfaces $S^{\rm f}(\boldsymbol{d})$ and $S^{\rm f}(-\boldsymbol{d})$ are complementary, one also finds that $s|_{\boldsymbol{d}} = -s|_{-\boldsymbol{d}}$ for all $\boldsymbol{\zeta} \in \tilde{S}^{\rm f}$, and thus

$$\phi^{\pm}(t,0)|_{\boldsymbol{d}} \;=\; -\phi^{\mp}(t,0)|_{-\boldsymbol{d}} \quad\Longrightarrow\quad \phi^{\pm}_{,s}(t,0)|_{\boldsymbol{d}} \;=\; \phi^{\mp}_{,s}(t,0)|_{-\boldsymbol{d}}. \tag{E 18}$$

From (E 12), (E 17) and (E 18), it follows that

$$J_3^{\partial S^{\rm f}}\big|_{\boldsymbol{d}} \;=\; \bar{J}_3^{\partial S^{\rm f}}\big|_{-\boldsymbol{d}}, \qquad J_5^{\partial S^{\rm f}}\big|_{\boldsymbol{d}} \;=\; -\bar{J}_5^{\partial S^{\rm f}}\big|_{-\boldsymbol{d}}.$$

On substituting the last result into (E 2) and (4.3), one immediately finds that

$$\mathsf{T}^{\partial S^{\rm f}}\big|_{\boldsymbol{d}} \,+\, \mathsf{T}^{\partial S^{\rm f}}\big|_{-\boldsymbol{d}} = 0 \quad\Longrightarrow\quad \int_{\Omega} \mathsf{T}^{\partial S^{\rm f}}\, d\Omega_{\boldsymbol{d}} = 0$$

which, in conjunction with (E 14)–(E 16), completes the proof of Theorem 4.7.

References

T1 A. Erdelyi. *Bateman Manuscript Project, Tables of Integral Transforms Volume II*. McGraw-Hill, New York, 1954.

T2 J. J. Stamnes. *Waves in Focal Regions*. Taylor & Francis, New York, 1986.

T3 V. A. Borovikov. *Uniform Stationary Phase Method*. Instit. Electrical Engineers, London, 1994.